

Synchronization of drift waves
and its effect on
fluctuation-induced transport

Dissertation
zur Erlangung des Doktorgrades
der Mathematisch-Naturwissenschaftlichen Fakultät
der Christian-Albrechts-Universität
zu Kiel

vorgelegt
von
Dietmar Block

Kiel
Dezember 2001

Referent: Prof. Dr. A. Piel
Koreferent: Prof. Dr. U. Stroth
Tag der mündlichen Prüfung: 1. Februar 2002
Zum Druck genehmigt: Kiel, den 1. Februar 2002

Der Dekan

Kurzfassung

Diese Arbeit behandelt den Einfluss von externen wellenartigen Potentialstrukturen auf die Dynamik von Driftwellen in Plasmen. Neben der detaillierten, experimentellen Untersuchung der Dynamik der getriebenen Driftwellen ist in diesem Zusammenhang von besonderem Interesse, ob der mit den Driftwellen verbundene anomale, fluktuationsinduzierte Teilchentransport durch eine geeignete Wahl des Treibersignals beeinflusst werden kann. Hierzu werden zunächst einige grundlegende, theoretische Betrachtungen der Driftwellendynamik angestellt und der van der Pol Oszillator als Paradigma eines nichtlinearen, getriebenen Systems vorgestellt. Es folgt eine kurze Zusammenfassung der statistischen Analysemethoden, die für die Auswertung der Messungen der Plasmaparameter mittels elektrostatischer Sonden benötigt werden. Die anschließende Beschreibung des Plasmaexperimentes und der verwendeten Diagnostiken umfasst eine detaillierte Analyse des Plasmagleichgewichtes und die Klassifizierung der beobachteten Fluktuationen als Driftwellen. Die hierbei erzielten Ergebnisse bilden die Grundlage für die eigentlichen Untersuchungen der Dynamik des getriebenen Zustandes. Durch den Vergleich zweier Plasmazustände unterschiedlicher Dynamik gelingt es, sowohl den Treibermechanismus zu charakterisieren, als auch Aussagen über die raumzeitliche Dynamik des getriebenen Systems zu machen und diese im Rahmen des getriebenen van der Pol Modells zu diskutieren. Eine Schlüsselrolle kommt hierbei der Vielsondendiagnostik zu. Als wesentliche Befunde sind zu nennen: die Charakterisierung der modenselektiven Wechselwirkung von Treiber und Driftwelle, die Beobachtung der zeitlichen und räumlicher Signaturen der vollständigen und unvollständigen Synchronisation und die Identifizierung des Einflusses des azimuthalen elektrischen Feldes des Exciters auf die Driftwellendynamik. Diese Ergebnisse ermöglichen es, aus den abschliessenden Transportuntersuchungen den Mechanismus der beobachteten Transporterhöhungen und -reduzierungen zu ermitteln. Es zeigt sich, dass die radiale Modenstruktur der getriebenen Driftwellen über Transporterhöhung oder -reduzierung entscheidet.

Abstract

In this work the influence of external wave-like potential structures on the dynamics of drift waves in plasmas is investigated. In the center of interest is, besides a detailed, experimental investigation of the dynamics of the driven drift waves, the question, whether the anomalous fluctuation-induced transport related to drift waves can be influenced by a proper choice of the driver signal. Hence, some fundamental theoretical considerations concerning drift wave dynamics are presented at first. Additionally, the van der Pol oscillator is introduced as a paradigm for a nonlinear, driven system. This is followed by a short overview of the statistical analysis methods, which are used to process the plasma parameters obtained from electrostatic probe measurements. The subsequent description of the plasma experiment and the applied diagnostics contains a detailed analysis of the plasma equilibrium and a classification of the observed fluctuations as drift waves. The obtained results form the basis for the intended investigations of the externally driven system. The comparison of two plasma states with different dynamics allows to characterize the driver mechanism and to investigate the spatio-temporal dynamics of the driven system. The results are discussed in the framework of the driven van der Pol model. Here, the multi-probe diagnostic plays a key role. The main results are: the characterization of the mode-selective interaction of drift wave and driver, the observation of temporal and spatial signatures of complete and incomplete synchronization and the identification of the influence of the azimuthal electric field of the exciter on the drift wave dynamics. These results permit an identification of the mechanism behind the observed transport enhancements and reductions. It turns out, that the radial mode structure of the driven drift modes determines the observed change of transport.

Contents

1	Introduction	1
2	Physics of Drift Waves	5
2.1	Basic equations	5
2.2	Linear models	6
2.2.1	Drift velocities	7
2.2.2	Full numerical model	8
2.2.3	Gauss numeric model	9
2.2.4	Local approximation	9
2.2.5	Drift wave mechanism	10
2.3	Nonlinear models	13
2.3.1	The Hasegawa-Wakatani model	13
2.3.2	The driven Hasegawa-Wakatani model	14
2.4	Fluctuation-induced $E \times B$ transport	15
2.5	Concluding remarks	16
3	The van der Pol oscillator	19
3.1	The roots of the van der Pol oscillator	19
3.2	Synchronized states of the van der Pol oscillator	20
3.2.1	Complete synchronization	21
3.2.2	Incomplete synchronization	22
3.3	Concluding remarks	25
4	Methods of data analysis	27
4.1	PDF and central moments	27
4.2	Correlation analysis	28
4.3	Spectral data analysis	28
4.4	Spectrally resolved transport	29
4.5	Phase sensitive data averaging	30
5	Experiment and diagnostics	33
5.1	Technical description	33
5.2	Diagnostics	35

5.2.1	Electrostatic probes	35
5.2.2	Special probes	37
5.2.3	Probe arrays	39
5.2.4	3D probe positioning system	39
5.2.5	Exciter	39
5.2.6	Positions of diagnostics	41
5.2.7	Data acquisition	42
5.3	Characterization of the plasma	42
5.3.1	Plasma equilibrium	43
5.3.2	Plasma fluctuations	46
5.4	Concluding remarks	50
6	Synchronization of drift waves	51
6.1	Single-mode state	51
6.1.1	Dynamics without exciter signal	52
6.1.2	Dynamics with exciter signal	52
6.1.3	Synchronization	55
6.1.4	Periodic pulling	57
6.2	Multi-mode state	70
6.2.1	Dynamics without exciter	70
6.2.2	Dynamics with co-rotating exciter signal	71
6.2.3	Dynamics with counter-rotating exciter signal	75
6.3	Synopsis	78
7	Effects of synchronization on transport	81
7.1	Single-mode state	81
7.1.1	Transport without driver signal	83
7.1.2	Influence of synchronization on transport	84
7.1.3	Transport and Periodic Pulling	90
7.2	Multi-mode state	92
7.2.1	Transport without driver signal	92
7.2.2	Transport with driver signal	94
7.2.3	Spectrally resolved transport measurements	100
7.3	Synopsis	103
8	Summary and outlook	105
	Bibliography	109

Chapter 1

Introduction

During the last 50 years, considerable effort has been spent on the investigation of anomalous transport in magnetically confined plasmas, on its origin and on possibilities to reduce it. The observed transport is usually not satisfactorily described by classical or neoclassical transport theory. Therefore, additional transport processes driven by universal instabilities are made responsible for the observed anomalous transport [1, 2, 3]. Most of these research activities are related to the quest to build a fusion reactor because, especially for the production and confinement of hot and dense fusion plasmas, the transport caused by the instabilities turned out to be a severe problem. These instabilities are driven by gradients in plasma pressure, which are common to bounded plasmas. Among the most prominent instabilities are drift waves, which propagate mostly azimuthally (in cylindrical plasmas) and have a radial fluctuation maximum close to the position of maximum density gradient. Hence, research on drift waves has been linked with the research on anomalous transport from the very beginning [4].

The first experimental observations of drift waves were made by D'ANGELO et al. [5, 6, 7] and the theoretical basis was founded independently by MOISEEV and SAGDEEV [8] and JUKES [9]. Soon after this LASHINSKY [10] and CHEN [11, 12, 13, 14] identified the universal character of the instability and linked the observations with microscopic physical processes. They proposed a local and linear drift wave model, which gave an acceptable description of the observations. To improve the description non-local models with a Gaussian density profile have been developed [15, 16]. ELLIS and co-workers showed that a non-local description with arbitrary density profiles is generally needed for a quantitative comparison with experimental data [17, 18]. The role of the radial electric field and the resulting $E \times B$ rotation of the plasma was first described by MARDEN-MARSHALL et al. [19].

Although these linear models were able to describe the drift wave mechanism and the destabilization of drift waves, non-linear models were needed to describe the saturation process, mode coupling and drift wave turbulence. Quite simple but nevertheless powerful non-linear models are the HASEGAWA-MIMA [20] and HASEGAWA-WAKATANI equations [21], which are named after their authors. These models already

allowed to study a number of general non-linear processes numerically, but they did not explain the observed anomalous transport in fusion experiments. With increasing computational power of today's computers more and more sophisticated non-linear models were developed [22, 23, 24]. The modeling of drift wave turbulence is still subject of intense research. Many mechanisms are discussed to cause or at least be related to the observed transport, e.g. streamers and zonal flows [25, 26] and coherent structures [27, 28], but the experimental verification of these concepts turns out to be difficult. One reason for this is the need for measurements with high spatio-temporal resolution. Especially for hot and dense fusion plasmas huge technical effort is necessary [29]. Therefore, many experimental observations of non-linear drift wave dynamics are made in low β plasmas, e.g. formation of coherent structures [30, 31, 32, 33] and transition to turbulence [34]. For low β plasmas the diagnostic is less complicated, but spatio-temporal measurements are still a sophisticated task [35, 36]. For transport measurements statistical techniques are used [37]. Spatio-temporal transport measurements are still rare, e.g. [38].

Parallel to the investigation of drift wave dynamics and the related transport, there have been attempts to control transport. Already at the beginning of the 70's first investigations with feedback techniques were started [39, 40]. Typically, in these experiments the density fluctuations were recorded with probes. Afterwards the signal was phase-shifted and amplified before it was fed back into the plasma via an electrode at a different spatial position. These experiments showed that the confinement was improved due to reduction of fluctuations, but for each drift mode to be suppressed a separate feedback circuit was needed. A suppression of broadband fluctuations has therefore not been achieved. Till today this technique has been refined and tested in fusion experiments [41, 42], but the observed reduction of fluctuations is localized and the efficiency is not satisfying.

More promising results are obtained with biasing experiments. The biasing experiments aim to generate such sheared flows by radial currents between electrodes inserted into the plasma and the vessel wall [43]. The basic idea behind these experiments rests on transport suppression by sheared flow [44]. The establishment of sheared flow is assumed to produce transport barriers, which are responsible for the L-H transition in fusion devices [45, 46, 47]. Although the understanding of sheared flows has improved substantially in the last years open questions concerning the details of transport suppression still remain.

A completely different approach to reduce plasma fluctuations is triggered by the improved understanding of nonlinear dynamics. It was shown that many chaotic systems can be stabilized with chaos control techniques [48, 49]. A successful application of these concept on weak drift wave turbulence has been demonstrated recently [50]. In contrast to the other methods, not all fluctuations are suppressed. Instead, a single mode is stabilized to suppress the other modes. The influence of this method on transport still needs to be investigated and will be part of the present thesis.

The idea to drive a single drift mode in order to reduce the fluctuation amplitude of other modes has found only little attention in the past [51, 52]. On the other hand, it

is well known, that the dynamics of nonlinear, oscillatory unstable dynamical systems with a periodic driving force exhibits peculiar features, e.g., quasi-periodicity [53] and period-doubling bifurcations towards chaos [54, 55]. Furthermore, complete and incomplete synchronization have been observed in various oscillatory unstable and periodically driven plasma experiments [56, 57, 58, 59, 60] and in computer simulations [61, 62]. The general concept of synchronization [53] turned out to be useful for many technical applications [63, 64]. In this context, synchronization means frequency entrainment, i.e., the oscillation frequency is shifted towards the frequency of the external driver. During incomplete synchronization the oscillation frequency is only locked to the driver frequency for a short time and entrainment is periodically lost. This happens when the coupling is too weak or the frequency mismatch is too large to establish complete synchronization. This effect is also known as periodic pulling [51] and is of great importance for the correct understanding of the dynamical behavior of various devices, such as unijunction transistor oscillator [65], microwave oscillator [63], neon bulb relaxation oscillator [66], and fluctuations in the Earth's magnetosphere [67]. In laboratory plasmas periodic pulling has been subject of several investigations in recent years, e.g., beam-plasma systems [68, 69, 70], ion sound waves [71, 72, 73], potential relaxation oscillations [74, 75, 76], and grid sheath oscillations [56]. Hitherto, most investigations have focused on the temporal aspect of synchronization, but now the interest is shifting towards spatio-temporal behavior, including wave phenomena. At present, the understanding is most advanced for metastable-guided ionization waves in neon gas discharges [77]. KOEPKE et al. showed that spatial and temporal signatures of periodic pulling are a fundamental feature of the transition between competing eigenmodes [78]. Recent studies attacked the problem by application of a controlled spatio-temporal driving force [79].

First experiments in Kiel and Nancy showed that drift wave dynamics can be influenced with spatio-temporal driver signals [80]. With a modified setup SCHRÖDER et al. [81] demonstrated that this control method is capable to synchronize selected drift modes in a weakly turbulent plasma state. Nevertheless, the driving mechanism and the nonlinear dynamics of such a driven system have not been investigated yet. Furthermore, the influence of the driver signal on transport is unknown.

The present work aims to link the research fields of nonlinear dynamics and anomalous transport studies. Related with each of them is a main objective of this work. On the one hand, it is of general interest to give a detailed spatio-temporal description of the driven drift wave system. Especially with respect to the investigations on ionization waves [78, 79], it is desirable to check whether the dynamics of this driven, spatio-temporal system comprise a spatial component, i.e. to generally validate the conjecture that spatial dynamics are typical for driven wave-like phenomena. On the other hand, any change of drift wave dynamics can cause severe changes of the related anomalous transport. Therefore, the investigation of the influence of spatio-temporal signals on anomalous transport is a main objective of this work as well. The combination of the results will allow to link possible changes of the fluctuation-induced transport with the observed dynamics of the driven system. Hence, the aim is to overcome the usual

empirical description of transport phenomena and to identify the mechanism related to the transport changes.

To investigate the drift wave dynamics with and without driver signals, temporal and spatio-temporal measurement techniques with high resolution are essential. For this purpose new probe positioning systems and an improved probe array are developed for the KIWI¹ (chapter 5). They are used to characterize and relate the plasma equilibrium and the observed plasma fluctuations. The theoretical basis forms a nonlocal, linear drift wave model (chapter 2). The nonlinear dynamics of the driven system are described in chapter 6. Especially, similarities with the dynamics of a driven van der Pol oscillator (chapter 3) are in the center of interest. The detailed investigation of the spatio-temporal dynamics is a main objective of this work. The question how the driver influences transport is discussed in chapter 7. Spatial and temporal transport properties are compared for different plasma states to relate the spatial mode structure of the drift modes with the observed transport. The statistical data analysis methods are briefly described in chapter 4.

¹Kiel Instrument for Wave Investigations

Chapter 2

Physics of Drift Waves

A common feature of all laboratory plasmas is the presence of boundaries, which produce gradients in plasma density, plasma temperature and plasma potential. On the one hand these gradients give rise to diffusion, which tend to flatten these gradients, on the other hand they provide a source of energy to drive instabilities. One type of these so called universal instabilities are drift waves [82, 83]. They are low frequency, electrostatic waves, which are driven by the pressure gradient. Their propagation direction is mainly perpendicular to the magnetic field. This chapter gives an introduction to the basic equations to describe the drift waves, their propagation, and dynamical characteristics. Starting with the fluid equations, linear drift wave models are deduced to discuss the basic characteristics of drift waves. The aim is to provide the background for a comparison with experimental observations in chapter 5. As an example for non-linear models the Hasegawa-Wakatani [21] model is briefly described. An extension of this model [81] is then used to raise questions, how an external driver signal influences drift wave dynamics.

2.1 Basic equations

Electrostatic waves in magnetized plasmas are typically described by three-dimensional fluid equations, in particular the equations for particle, momentum and energy conservation

$$0 = \frac{\partial n}{\partial t} + \nabla \cdot (n\mathbf{v}_\alpha), \quad (2.1)$$

$$nm_\alpha \left(\frac{\partial}{\partial t} + \mathbf{v}_\alpha \cdot \nabla \right) \mathbf{v}_\alpha = nq_\alpha (\mathbf{E} + \mathbf{v}_\alpha \times \mathbf{B}) - \nabla p_\alpha - \nabla \cdot \Pi_\alpha - nm_\alpha \nu_\alpha \mathbf{v}_\alpha, \quad (2.2)$$

$$0 = \frac{3}{2}n \left(\frac{\partial}{\partial t} T_\alpha + \mathbf{v}_\alpha \cdot \nabla T_\alpha \right). \quad (2.3)$$

Here, $\alpha = i, e$ is the particle index for ions or electrons, n the plasma density, m_α the particle mass, q_α the particle charge, ν_α the particle-neutral collision frequency,

Π_α the stress tensor and \mathbf{v}_α the particle velocity. Bold face variables are vectors. Due to the fluid description kinetic effects are already neglected, but besides this a number of additional assumptions are underlying these equations [84]:

- All particles are singly charged.
- The plasma is weakly ionized, i.e. only collisions with neutrals are taken into account.
- All fluctuations are electrostatic ($\mathbf{E} = -\nabla\phi$). Due to $m_e/m_i \ll 1$, this assumption yields in combination with Eq. 2.2 to the condition that the electron pressure has to be small compared to the magnetic pressure, i.e. $\beta \ll 1$.
- Any perturbation of density n and electric potential ϕ is assumed to be of low frequency, $\omega_\alpha \ll \Omega_\alpha = q_\alpha B/m_\alpha$, and its typical scale length is large compared to the Debye length λ_d . This assures quasi-neutrality, i.e. $n_e \approx n_i$, and implies $\nabla \cdot \mathbf{J} = 0$, with the current density $\mathbf{J} = \sum n q_\alpha \mathbf{v}_\alpha$. Furthermore, it founds the basis to solve the fluid equations in the framework of the drift approximation, i.e. all gyro motions are neglected and the particle velocities are approximated by drift velocities.
- The ratio of scale of motion Δ_\perp and pressure gradient $L_\perp = |\nabla_\perp \log p|$ and of the wave numbers k_\parallel and k_\perp (with respect to \mathbf{B}) should be small compared to 1, i.e. $\Delta_\perp/L_\perp \sim k_\parallel/k_\perp \ll 1$.

Although, all these assumption simplify the equations without changing drift wave dynamics, they are still far to complicated to allow for an analytical solution. Nevertheless, by neglecting different sets of terms simpler models can be derived, which indeed allow for some analytical treatment.

2.2 Linear models

Waves in bounded plasmas are characterized by their mode structure and the propagation speed of the individual modes. As a first step, it is desirable to deduce a dispersion relation for drift waves. For plasma conditions as in KIWI the following additional assumptions can be made to simplify equations 2.1-2.3:

- The plasma is isothermal, i.e. $p_\alpha = k_B n T_\alpha$. Hence, Eq. 2.3 becomes identical with Eq. 2.1 and can therefore be skipped.
- The ions are cold, i.e. $T_i = 0$ and $p_i = 0$.
- The magnetic field \mathbf{B} is homogeneous and directed along the z -axis.
- Electron inertia is neglected.

By inserting $p_\alpha = k_B n T_\alpha$ into the electron momentum equation, a modified set of equations is obtained

$$0 = \frac{\partial n}{\partial t} + \nabla \cdot (n \mathbf{v}_\alpha) \quad (2.4)$$

$$nm_i \left(\frac{\partial}{\partial t} + \mathbf{v}_i \cdot \nabla \right) \mathbf{v}_i = nq_i (\mathbf{E} + \mathbf{v}_i \times \mathbf{B}) - m_i \nabla_i \mathbf{v}_i \quad (2.5)$$

$$0 = nq_e (\mathbf{E} + \mathbf{v}_e \times \mathbf{B}) - k_B T_e \nabla n - m_e \nabla_e \mathbf{v}_e \quad (2.6)$$

2.2.1 Drift velocities

By crossing the momentum equations with \mathbf{B} important particle drifts perpendicular to \mathbf{B} are obtained [85]:

electron diamagnetic drift velocity

$$\mathbf{v}_* = \frac{\omega^*}{k_\perp} \mathbf{e}_{\parallel \mathbf{E}} = \frac{L_\perp}{eB} \mathbf{e}_{\parallel \mathbf{E}}, \quad (2.7)$$

$E \times B$ drift velocity

$$\mathbf{v}_E = \frac{\omega_E}{k_\perp} \mathbf{e}_{\perp \mathbf{E}} = \frac{\mathbf{E} \times \mathbf{B}}{B^2}, \quad (2.8)$$

ion polarization drift velocity

$$\mathbf{v}_p = \frac{\omega_p}{k_\perp} \mathbf{e}_{\parallel \mathbf{E}} = \frac{1}{\Omega_i B} \frac{d\mathbf{E}}{dt} = -\frac{m_i}{eB^2} \mathbf{B} \times \left(\frac{\partial}{\partial t} - \mathbf{v}_E \cdot \nabla \right) \mathbf{v}_E. \quad (2.9)$$

ω^* , ω_E and ω_p denote the related frequencies. Although, the latter is small compared to the other it is important due its finite divergence. It counteracts charge separation, caused by electron dynamics, and thus ensures the quasi-neutrality of the plasma [86].

The z-component of the electron momentum equation can be used to calculate the electron drift along the magnetic field.

$$\mathbf{v}_{\parallel} = \frac{\omega_{\parallel}}{k_{\parallel}} = \frac{eE_{\parallel}}{m_e \nu_e} \quad (2.10)$$

The parallel dynamics of the ions is neglected due to their larger mass. With these drifts the electron and ion velocities can be written as

$$\begin{aligned} \mathbf{v}_{e\perp} &= \mathbf{v}_E + \mathbf{v}_* \\ \mathbf{v}_{e\parallel} &= \mathbf{v}_{\parallel} \end{aligned} \quad (2.11)$$

$$\begin{aligned} \mathbf{v}_{i\perp} &= \mathbf{v}_E + \mathbf{v}_p \\ \mathbf{v}_{i\parallel} &= 0. \end{aligned} \quad (2.12)$$

Obviously, the obtained drifts allow for a separate treatment of the dynamics parallel and perpendicular to \mathbf{B} .

2.2.2 Full numerical model

Up to now no assumptions are made upon the coordinate system. Due to the symmetry of the KIWI device cylindrical coordinates are chosen to solve Eq. 2.4-2.6. A treatment in local slab geometry would lead to the same qualitative results, but it would not reproduce the experimental observations quantitatively [18, 87].

A linearization of the fluid equations with the assumption of harmonic perturbations with the azimuthal mode number $m = rk_{\perp}$

$$n = n_0 + \tilde{n} = n_0 + \tilde{n}(r) \exp(i(m\Theta + k_{\parallel}z - \omega t)) \quad (2.13)$$

$$\mathbf{v} = \mathbf{v}_0 + \tilde{\mathbf{v}} = \mathbf{v}_0 + \tilde{\mathbf{v}}(r) \exp(i(m\Theta + k_{\parallel}z - \omega t)) \quad (2.14)$$

$$\phi = \phi_0 + \tilde{\phi} = \phi_0 + \tilde{\phi}(r) \exp(i(m\Theta + k_{\parallel}z - \omega t)) \quad (2.15)$$

allows to derive a differential form of the dispersion relation

$$0 = \left[\nabla_{\perp}^2 + \frac{1}{n_0} \frac{dn_0}{dr} \frac{d}{dr} + \left(1 + \frac{2\omega_E}{m\Omega_i} - \frac{\omega_E^2}{m\Omega_i(\omega - \omega_E + i\nu_i)} \right) Q(\omega - \omega_E) - \frac{(\omega^* + i\nu_{\parallel})(2\omega\omega_E - \omega_E^2)}{\rho^2 m\Omega_i(\omega - \omega_E + i\nu_i)(\omega - \omega_E - \omega_{\parallel} + i\nu_{\parallel})} \right] \Psi \quad (2.16)$$

where

$$\nabla_{\perp}^2 = \frac{d^2}{dr^2} + \frac{1}{r} \frac{d}{dr} - \frac{m^2}{r^2} \quad (2.17)$$

$$Q(\omega - \omega_E) = \frac{i\nu_{\parallel}(\omega^* - \omega + \omega_E) - \omega^* \omega_{\parallel}}{\rho^2(\omega - \omega_E + i\nu_i)(\omega - \omega_E - \omega_{\parallel} + i\nu_{\parallel})} \quad (2.18)$$

$$\rho^2 = \frac{k_B T_e}{eB\Omega_i} \quad (2.19)$$

$$\nu_{\parallel} = \frac{k_{\parallel}^2 k_B T}{m_e \nu_e} \quad (2.20)$$

$$\Psi = \frac{e\tilde{\phi}}{k_B T_e} \quad (2.21)$$

ρ is the ion gyro radius at electron temperature and is normally used as a characteristic length scale. Ψ is the normalized plasma potential fluctuation. Eq. 2.16 is known as *full numerical model* [17] and can be solved numerically with boundary conditions $\Psi(0) = \Psi(a) = 0$, i.e. vanishing fluctuation amplitudes at the center of the plasma column and its radial boundary. As result the radial eigenmode $\Psi(r) \sim \tilde{n}(r)$ and the complex eigenfrequencies $\omega = \omega_R + i\omega_I$ are obtained.

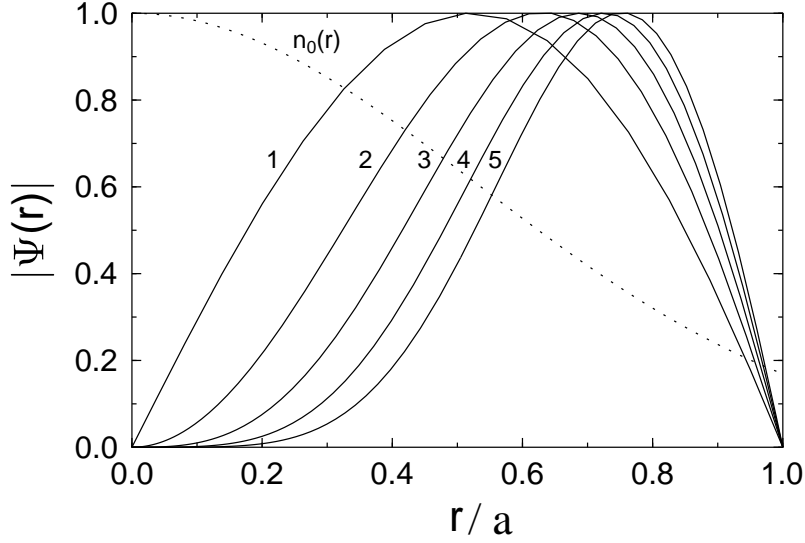


Figure 2.1: Radial fluctuation profile $\Psi(r)$ for a Gaussian density profile $n_0(r)$ for azimuthal mode numbers $m=1 \dots 5$.

2.2.3 Gauss numeric model

The dispersion relation (Eq. 2.16) simplifies significantly if a Gaussian density profile $n_0(r) \sim \exp(-r^2/a^2)$ is assumed and if collisions and $E \times B$ rotation are neglected. The resulting model is named 'Gauss Numeric Model' (GNM) [17] and is by far easier to handle, because the diamagnetic frequency ω^* is no longer depending on r . The differential dispersion equation simplifies to

$$\frac{d^2}{dr^2} \Psi + \left(\frac{1}{r} - \frac{r^2}{a^2} \right) \frac{d}{dr} \Psi + \left(Q - \frac{m^2}{r^2} \right) \Psi = 0. \quad (2.22)$$

Because Q is no longer depending on r , $\Psi(r)$ becomes real. The solution for $\Psi(r) \sim \tilde{n}(r)$ for different azimuthal mode numbers is shown in Fig. 2.1. The fluctuation maximum is located close to the maximum density gradient. Additionally, the position of maximum density fluctuation depends on the azimuthal mode number. With increasing mode number its position shifts radially outwards and the radial extent of the eigenmode decreases.

2.2.4 Local approximation

For a local approximation the derivatives of Ψ can be neglected. The obtained local dispersion relation

$$Q(\omega - \omega_E) = 0 \quad (2.23)$$

can then be solved analytically for different cases [88]. The main results from these approximations are:

1. The real part ω_R is mainly affected by the $E \times B$ -rotation of the plasma column and the diamagnetic drift. A good approximation is given by

$$\omega_R = \omega_E + \frac{\omega^*}{1 + Q\rho^2}, \quad (2.24)$$

i.e. the $E \times B$ -rotation of the plasma column causes a Doppler shift in the observed frequency. The factor $(1 + Q\rho^2)^{-1}$ is related to ion inertia. Typically, $Q\rho^2$ is of the order of 1. A similar calculation in local slab geometry reveals an expression, where Q is replaced by k_\perp^2 , i.e. Q can be regarded as square of a perpendicular wave vector. This interpretation of Q shows, that ion inertia introduces dispersion to the drift waves.

2. The imaginary part ω_I describes the stability conditions for the wave. Destabilizing effects are $E \times B$ -rotation, radial shear of $E \times B$ -rotation, and axial currents in combination with electron collisions. On the other hand, ion collisions are stabilizing.
3. $Q \sim m$, i.e. the dispersion depends on the azimuthal mode number.
4. The growth rate of the drift waves is proportional to the radial density gradient.

2.2.5 Drift wave mechanism

The parallel electron dynamics play a key role for the whole drift wave mechanism. Especially the stability of the drift waves is determined by the parallel electron response [89]. The detailed mechanism is described by a physical picture given by Chen [13].

The parallel electrons dynamics is described by the parallel component of the electron momentum equation (Eq. 2.6). A simple integration of Eq. 2.6 and neglect of collisions yields the Boltzmann relation

$$n = n_0 \exp\left(\frac{e\phi}{k_B T_e}\right). \quad (2.25)$$

This relation forms a connection between density and potential and results from Maxwellian velocity distribution of the electrons. Basically, Eq. 2.25 states that any density perturbation is in-phase with a potential perturbation, i.e. positive density perturbations have positive potential and negative density perturbations have negative potential. The resulting implications are illustrated in Fig. 2.2 a. The solid lines give equi-density (potential) contours. The density gradient is perpendicular to the unperturbed equi-density contour (dashed line). Due to Eq. 2.25 density and potential perturbations are in-phase and positive (negative) density perturbation have positive (negative) potential. The resulting electric field is indicated by arrows. The field strength is indicated by the length of the arrows. The electric field is zero at the maxima and minima of the density

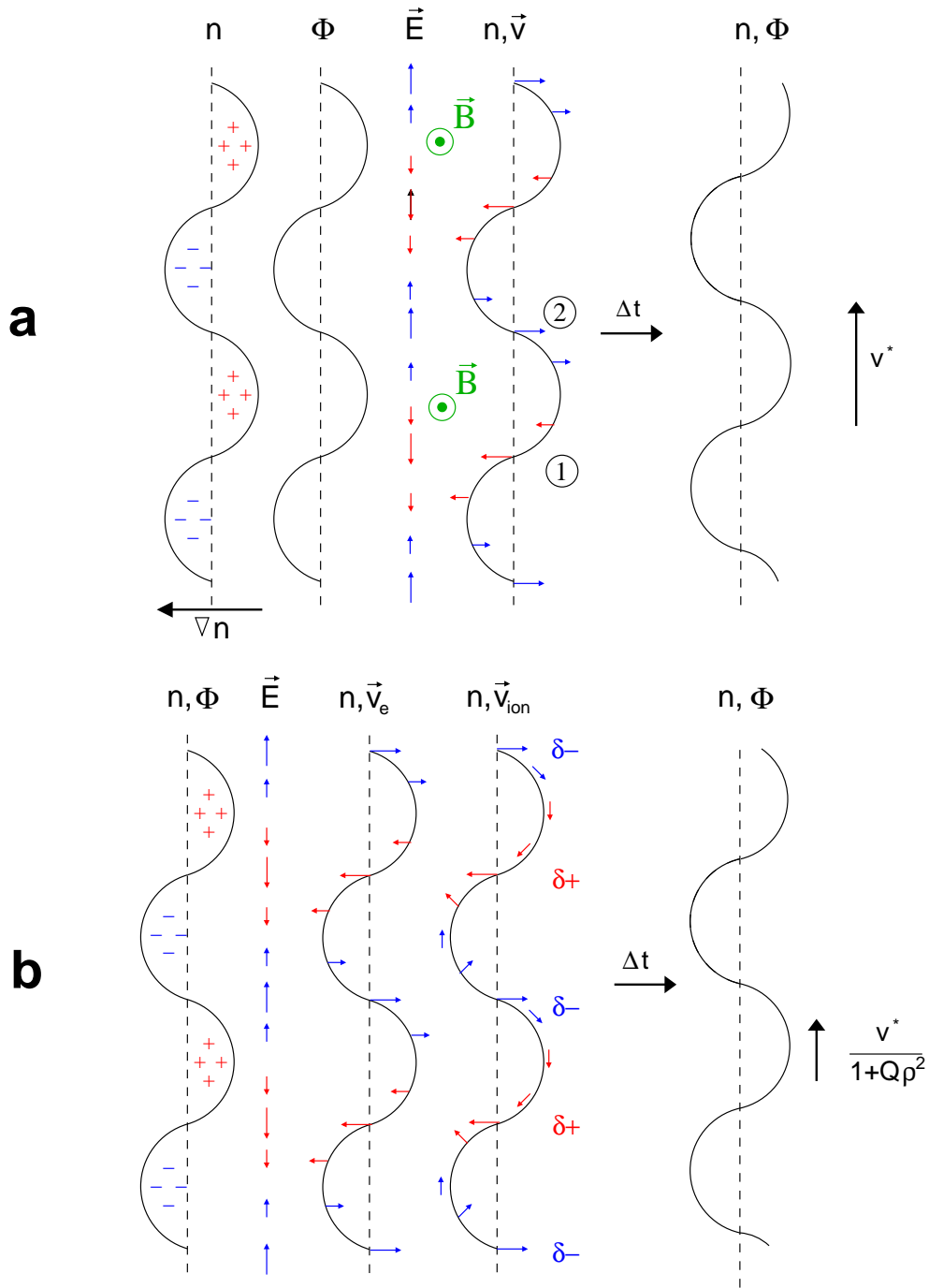


Figure 2.2: (a) Basic elements of drift wave propagation. Surplus and reduced charge densities are indicated by '+' and '-'. The arrows sketch amplitude and direction of the electric field E and the $E \times B$ -velocity. The magnetic field is oriented out of the paper. (b) drift wave mechanism including ion inertia. The drift velocities for electrons are plotted separately. The charge separation caused by the different drifts for ions and electrons is indicated by $\delta\pm$. After Chen [13]

perturbations and maximum at the positions of zero density perturbation. The combination of magnetic field and local electric fields yields to $E \times B$ -drifts parallel to ∇n . Their influence on the density contour is depicted in the ' n, \mathbf{v} ' plot. The local $E \times B$ velocities are indicated by arrows. Their length corresponds to the absolute value of the local drift velocity. According to the local electric fields, the drift velocity is maximum at the positions of zero density perturbations. At position 1, the drift velocity is in direction of the density gradient, i.e. plasma with lower density is drifting towards regions of higher density and form a negative density perturbation. At position 2, it is vice versa. The $E \times B$ drift shifts plasma with higher density into regions of lower density. The combination of all local drifts results in a propagation of the drift wave with electron diamagnetic drift velocity in direction of $\nabla n \times B$. The important fact is that the density gradient is the driving force of the wave. The steeper the density gradient is, the stronger are density perturbations caused by small drifts along the gradient. Via the Boltzmann distribution of the electrons the local potential and therefore the local electric fields are directly linked with the density perturbations. This means the whole process is self-consistent and only the density gradient as driving force determines the propagation velocity of the wave, although Fig. 2.2 a might give the impression that the electric fields are responsible for the wave propagation. For externally generated electric fields this argument will not hold any longer. In this case, the propagation of the wave can depend explicitly on these external fields.

However, this simple drift wave mechanism changes slightly if ion inertia is taken into account. Due to the wave propagation, the electric field at a fixed position changes. According to Eq. 2.9 these electric field fluctuations cause polarization drifts, which are directed parallel to the propagation of the wave. Using Eq. 2.9 and 2.12 the ion velocities are obtained as shown in Fig. 2.2 b. Obviously, the electron and ion drifts are no longer identical. Therefore, the polarization drift leads to an additional charge build up indicated by δ_{\pm} . This charge build-up gives rise to electric fields which slow down the drift wave propagation.

This simple picture describes the propagation of an establish drift wave, but it does not contain any instability mechanism, because the $E \times B$ velocity is zero for minimum and maximum density perturbation. This situation will change as soon as density and potential are not in-phase. Any phase shift will lead to non-vanishing electric fields at positions of maximum and minimum density perturbation. The consequence is an increase or damping of wave amplitude depending on sign of the phase shift. To achieve such phase shifts, the parallel electron dynamics has to be included, because otherwise the electrons would immediately cancel this phase shift in order to satisfy the Boltzmann relation. Only if the electron flow along B is impeded, the Boltzmann relation can be violated. The resulting phase shift between density and potential is then responsible for a growth of the perturbation. Some of the destabilizing mechanisms have already been mentioned. Despite of these there are others like electron-ion collisions in dense plasmas, Landau damping in collisionless plasmas, and inductance in high β plasmas.

2.3 Nonlinear models

Although linear models give insight into the basic drift wave dynamics, they do not explain, how linear unstable drift modes saturate. This saturation process is obviously a nonlinear effect. Further, observations of nonlinear processes like mode interaction, mode competition and turbulence raise the need for nonlinear drift wave models. Since an analytical treatment of these processes is very limited, a number of different approaches have been followed in the past. Mainly two directions can be distinguished: In last few years the increasing computational power of today's computers allowed to spend more and more effort on obtaining as realistic models as possible by including i.e. complex magnetic topology [90] or electro-magnetic effects [24]. On the other hand, rather simple models are popular to investigate new dynamical concepts and phenomena like self-organized criticality [91, 92, 93] and zonal flows and streamers [25, 26]. These models are sometimes referred to as 'toy models', because their simplifications guarantee low numerical efforts while conserving fundamental features of nonlinear dynamics.

2.3.1 The Hasegawa-Wakatani model

One of the most famous models is the Hasegawa-Wakatani model. It can be directly deduced from the fluid equations [21, 94]. The main assumptions are:

1. The electron response along \mathbf{B} is non-adiabatic due to resistivity.
2. The polarization drift is retained to lowest order for the ions and ion viscosity is taken into account.
3. Only the dominant terms from the nonlinearity are kept.

Evaluating the continuity equations for ions and electrons with these assumptions and introducing dimensionless variables lead to

$$\frac{\partial}{\partial t} \nabla_{\perp}^2 \tilde{\phi} + \mathbf{v}_{\mathbf{E}} \cdot \nabla \nabla_{\perp}^2 \tilde{\phi} = \nabla_{\parallel} J_{\parallel} + \mu_w \nabla_{\perp}^4 \tilde{\phi} \quad (2.26)$$

$$\frac{\partial}{\partial t} \tilde{n} + \mathbf{v}_{\mathbf{E}} \cdot \nabla (n_0 + \tilde{n}) = \nabla_{\parallel} J_{\parallel} + \mu_n \nabla_{\perp}^2 \tilde{n} \quad (2.27)$$

with $J_{\parallel} = -\sigma \nabla_{\parallel} (\tilde{\phi} - \tilde{n})$. The viscous terms $\mu_n \nabla_{\perp}^2 \tilde{n}$ and $\mu_w \nabla_{\perp}^4 \tilde{\phi}$ have been entered artificially to the equations to assure regularity of density and potential. In many cases the spatially three-dimensional model is reduced to two spatial dimensions by introduction of an effective wave length $\nabla_{\parallel}^2 \rightarrow -k_{\parallel}^2$. This approximation is motivated by experimental observations of long correlation length along the magnetic field [2] and reduces drastically the computational efforts. A Fourier transform and linearization of Eq.2.26 and 2.27 yield to a dispersion relation similar to those obtained for the presented linear models.

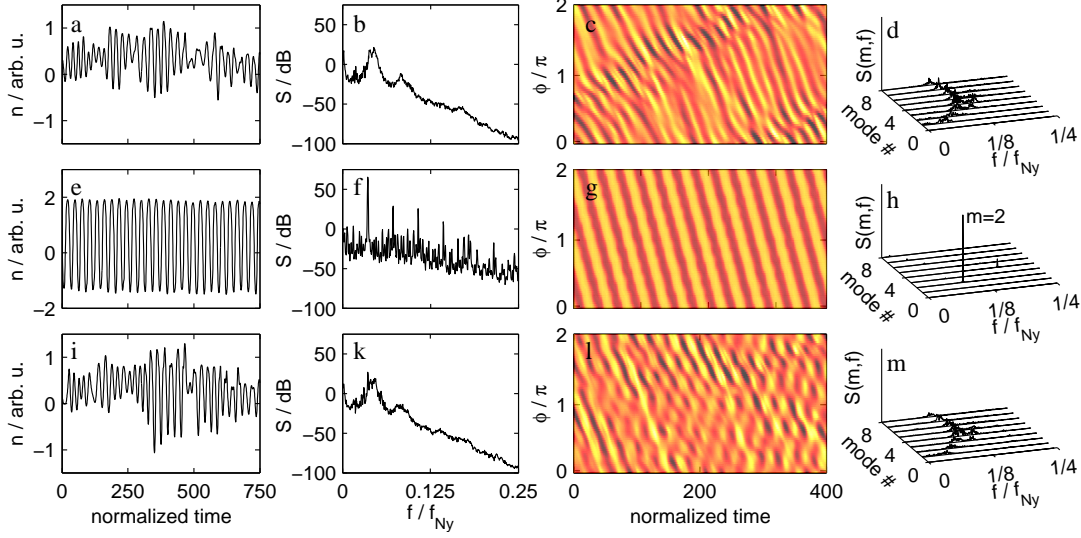


Figure 2.3: *simulation results, (a-d) show the dynamics with out driver signal, (e-h) are obtained for co-rotating $m = 2$ driver signal, and (i-m) are for counter-rotating $m = 2$ driver signal. The plots (a,e,i) are typical time series of density. The related power spectrum is depicted in (b,f,k). The contour plots (c,g,l) are time series from an artificial 64 probe array. The probe are arranged to cover the full circumference of the plasma column. The frequency mode number spectrum of these contour plots are shown in (d,h,m).*

2.3.2 The driven Hasegawa-Wakatani model

The equations for the driven system differ by an additional driver term from the un-driven system. This driver term is motivated by previous experiments, where an external spatio-temporal driver signal has been used to influence drift wave turbulence [38, 81]. The assumption is that this driver signal can be described by an oscillatory parallel current profile of the functional form

$$S = \nabla_{\parallel} J_{ext} = A \sin(\pi r/a) \sin(2\pi m \Theta - \omega_{ext} t). \quad (2.28)$$

The modified model equations are

$$\frac{\partial}{\partial t} \nabla_{\perp}^2 \tilde{\phi} + \mathbf{v}_E \cdot \nabla \nabla_{\perp}^2 \tilde{\phi} = \nabla_{\parallel} (J_{\parallel} - J_{ext}) + \mu_w \nabla_{\perp}^4 \tilde{\phi} \quad (2.29)$$

$$\frac{\partial}{\partial t} \tilde{n} + \mathbf{v}_E \cdot \nabla (n_0 + \tilde{n}) = \nabla_{\parallel} (J_{\parallel} - J_{ext}) + \mu_n \nabla_{\perp}^2 \tilde{n}. \quad (2.30)$$

The numerical solution of these equations is performed in poloidal coordinates with a prescribed background density of the form $n_0 = 2.5 \cos(r/a)$. More details including a comparison with experimental data can be found in [81]. At this point only

the simulation results are briefly discussed, because a description of the experimental techniques and obtained data will be given in the following chapters.

Fig. 2.3 gives an overview of the drift wave dynamics for different driver signals. From top to bottom, the dynamics are analyzed for the undriven system, the driven system with a co-rotating driver signal (driver signal propagates in the same direction as the drift waves) and the driven system with counter-rotating driver signal. The time series (Fig. 2.3 a, e and i) as well as the spectra (Fig. 2.3 b, f and k) show clearly that only for the co-rotating case a harmonic signal is obtained. Further, it is notable that the time series and spectra for the undriven and counter-rotating case indicate almost identical dynamics. The color plots visualize the spatio-temporal density fluctuations along one poloidal circumference and show that only for the co-rotating driver signal a regular wave pattern is observable. The frequency-mode-number-power spectra (Fig. 2.3 d, h, and m) underline this optical impression. To conclude, the simulations show that a spatio-temporal driver signal has strong influence on the drift wave dynamics, if the spatial and temporal evolution of driver signal and drift mode match.

Because of the fixed background density gradient, this model does not allow to investigate the influence of the driver signal on fluctuation-induced transport. Investigations of transport processes require a 3D model, which establishes background density and potential profiles self-consistently from sources and sinks.

2.4 Fluctuation-induced $E \times B$ transport

A common feature of all attempts to influence drift waves dynamics is the hope to influence fluctuation-induced transport and if possible to reduce it. For further discussion of this aspect, it is important to drop a few words on why fluctuations do cause transport.

Fig. 2.4 shows two different arrangements of potential and density perturbations. For zero phase shift between potential and density the average $E \times B$ transport cancels (Fig. 2.4 a), because on opposite sides of the structure as many particles are convected to the left as to the right. This changes, if a phase shift between density and potential fluctuation is introduced (Fig. 2.4 b). At positions with same potential, i.e. same $E \times B$ velocity, the density is different. The result is that less particles are convected at the position of lower density. Consequently, Γ_1 is much smaller than Γ_2 . The resulting net-transport $\Gamma = \Gamma_2 - \Gamma_1$ is directed to the right.

The same can be obtained by a simple analysis. Assuming that density \tilde{n} and electric field $\tilde{E} = -\nabla\tilde{\phi}$ are fluctuating sinusoidally with frequency ω and phase shift α_{nE} , the fluctuation induced transport $\tilde{\Gamma}_{E \times B}$ is given by

$$\Gamma_{E \times B} = \tilde{n} \tilde{v}_{E \times B} \sim \sin(\omega t) \sin(\omega t + \alpha_{nE}) = \frac{1}{2} (\cos(\alpha_{nE}) - \cos(2\omega t + \alpha_{nE})) \quad (2.31)$$

This means, that the fluctuation-induced transport fluctuates with twice the frequency

and the average transport

$$\langle \Gamma_{E \times B} \rangle = \frac{1}{2} \cos \alpha_{nE} \quad (2.32)$$

is only zero if the phase shift $\alpha_{nE} = \pm\pi/2$, i.e. if density and potential fluctuations have no phase shift.

The implications for drift waves are, that any phase shift between density and potential will lead to radial net-transport. Fig. 2.5 depicts the qualitative situation for a $m = 2$ mode in a cylindrical plasma column. The colored circles mark the density perturbations. The phase shifted potential perturbations are indicated by the black circles. The electric field is maximum right between the centers of maximum and minimum potential. At these positions the $E \times B$ transport is pointing outwards. Only for small regions close to the potential minima and maxima the transport is pointing inwards. However, at these positions the transport is weak, because of the weak electric field close to the potential extrema. This can not compensate the outward oriented transport. Obviously, the $m = 2$ mode structure in n and ϕ generates a $m = 4$ mode structure in Γ . The azimuthal propagation of this structure with doubled spatial periodicity explains the frequency doubling for Γ (Eq. 2.31). This shows that the temporal fluctuations of Γ are directly linked with its spatial structure.

2.5 Concluding remarks

It can be stated that linear drift wave physics is well understood and allows for a comparison of models and experiments. For nonlinear drift wave dynamics the understanding is less advanced. For the driven Hasegawa-Wakatani model promising parallels with experimental findings are observed. Nevertheless, a number of questions remain open:

- How does synchronization of drift waves work in detail?
- Is synchronization observed for any driver frequency or only for special frequency regimes?
- Is there a way to quantify the influence of the driver on the system?
- Does synchronization affect fluctuation induced transport?

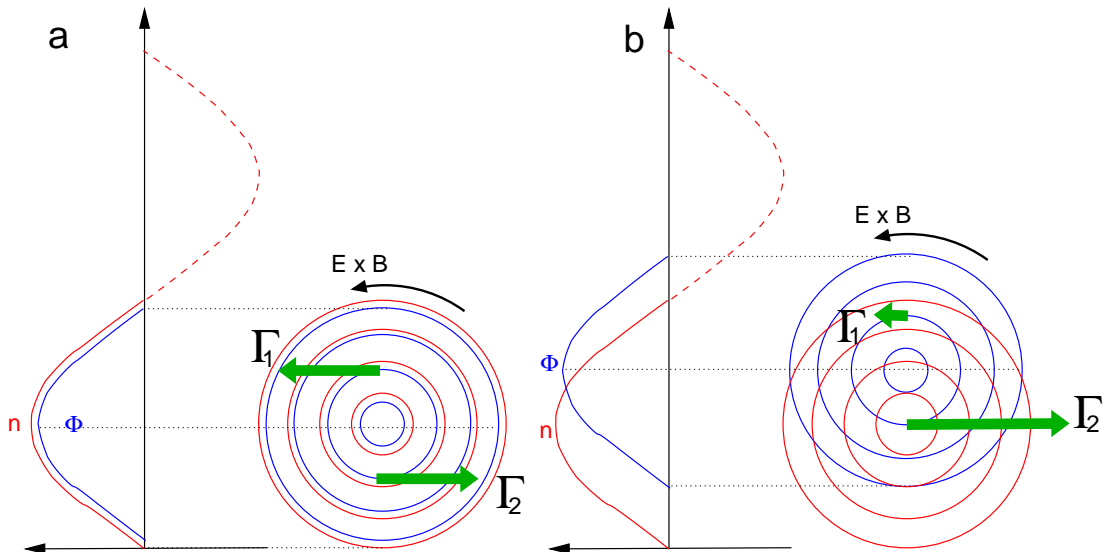


Figure 2.4: Fluctuation-induced $E \times B$ transport for different phase shift of density n and potential Φ , (a) zero phase shift, (b) phase shift of $\pi/4$. The resulting $E \times B$ transport is indicated by arrows. For (b) the particle transport is not balanced.

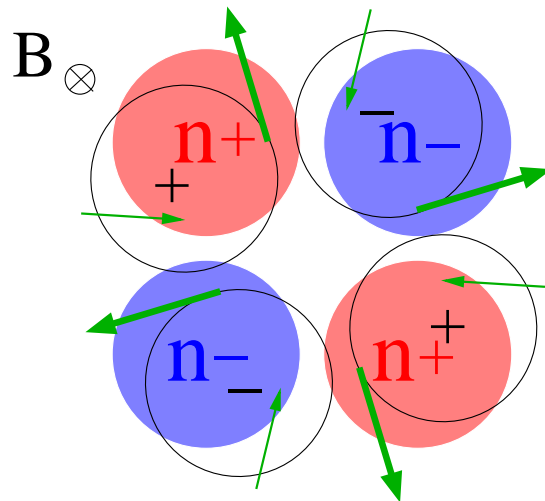


Figure 2.5: Fluctuation-induced $E \times B$ transport for a $m = 2$ mode with a phase shift between density and potential. The colored circles mark the regions of positive and negative density perturbations. The black circles indicate the positions of positive and negative potential perturbations. The green arrows are the resulting $E \times B$ transport. Their size reflects the transport strength.

Chapter 3

The van der Pol oscillator

It has been mentioned in the introduction that the phenomenon of complete and incomplete synchronization is observed in a number of oscillatory unstable and periodically driven plasma experiments [56, 68, 72, 74]. Typically, these are systems with high-dimensional dynamics expressed by systems of multi-dimensional, coupled, partial differential equations. Most of these systems do not allow for an analytic study of the dynamics. Despite of these complex systems there are rather simple systems, which show similar dynamics. Their description in terms of ordinary differential equations permits far reaching analytic studies. One of these systems is the van der Pol oscillator. By means of this model this chapter introduces into the dynamics of synchronization and the related characteristics.

3.1 The roots of the van der Pol oscillator

The most famous oscillatory system is for certain the mathematical pendulum. It is described by the nonlinear differential equation

$$\frac{d^2\theta}{dt^2} + \omega_0^2 \sin \theta = 0 \quad (3.1)$$

with elongation θ and oscillation frequency ω_0 . To expand the description to dissipative systems a new term is added to the force balance. Usually the velocity dependent Stokes friction is chosen. To balance the energy dissipation by friction an energy source can be included into the equation as well. Then the linearized differential equation is

$$\frac{d^2\theta}{dt^2} + \underbrace{\gamma \frac{d\theta}{dt}}_{friction} + \omega_0^2 \theta = \underbrace{E_0 \cos(\omega_i t)}_{source} \quad (3.2)$$

Another way to balance the friction even without external driver is to insert a more complicated friction term $f(\theta_0, \theta, \dot{\theta})$, where θ_0 is the amplitude threshold marking the

change from energy dissipation to energy influx. The according equation has been derived by VAN DER POL [95].

$$\frac{d^2\theta}{dt^2} - \gamma_0 f(\theta_0, \theta, \dot{\theta}) \frac{d\theta}{dt} + \omega_0^2 \theta = E_0 \cos(\omega_i t) \quad (3.3)$$

The simplest realization for the nonlinear function $f(\theta_0, \theta, \dot{\theta})$ is an amplitude dependent friction, e.g.

$$f(\theta_0, \theta, \dot{\theta}) = 1 - \frac{\theta^2}{\theta_0^2}. \quad (3.4)$$

The main ingredients, which make the dynamics of this system interesting, are the energy source, the limiter and the driver. The energy source drives the system and compensates the friction. The nonlinearity of the friction limits the oscillation amplitude and establishes a stationary oscillation, while the nonlinear interaction of driver and oscillatory system enriches the dynamics.

3.2 Synchronized states of the van der Pol oscillator

The dynamics of the driven van der Pol oscillator comprise, despite of the quite simple differential equation, a number of dynamics, which are observed in much more complicated systems. A common dynamical situation observed in these systems is synchronization, which is also entitled as mode or phase-locking. The latter already describes the dynamics well, because for a synchronized state the driver and the oscillating system have a fixed phase relation. Their phases are locked and the system shows regular periodic oscillation. Basically, three types of synchronization can be distinguished:

1. sub-harmonic synchronization ($\omega_i < \omega_0$),
2. harmonic synchronization ($\omega_i \approx \omega_0$),
3. higher harmonic synchronization ($\omega_i > \omega_0$),

with the driver frequency ω_i and the the natural oscillation frequency ω_0 . In any case, the ratio ω_i/ω_0 has to be rational or close to a rational value to achieve synchronization. Mathematically, the phase-locking is treated by adding a phase shift to the driver term and assuming

$$\theta(t) = a \cos(\omega_i t) + b \cos(n\omega_i t). \quad (3.5)$$

For $b = 0$, harmonic synchronization is obtained. For sub-harmonic and higher harmonic synchronization, b has to be non-zero. In this case, n determines whether sub- or higher harmonic synchronization is obtained ($n = 2, 3, 4, \dots$ for sub-harmonic synchronization, $n = 1/2, 1/3, \dots$ higher harmonic synchronization). A detailed analysis and discussion of the results of this approach is given in [53]. Here, only some aspects directly related to this work will be summarized.

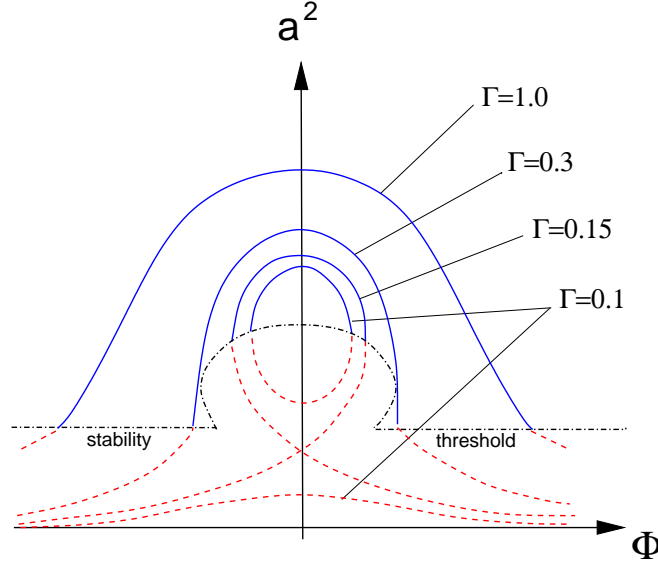


Figure 3.1: Resonance curve $\Gamma(a^2, \Phi)$ of the driven van der Pol oscillator. The solid blue lines mark stable solutions. The dashed red lines are unstable solutions.

3.2.1 Complete synchronization

First, the relation between driver amplitude E and oscillation amplitude a can be obtained. For the harmonic case it is

$$\frac{E^2}{4\gamma_0^2\omega_i^2} = \frac{a^2}{4} \left[\left(\frac{\omega_0^2 \omega_i^2}{\gamma_0 \omega_i} \right) + \left(\frac{a^2}{4} - 1 \right) \right] \quad (3.6)$$

For simplification the parameters Γ and Φ are usually introduced.

$$\Gamma = \frac{E^2}{4\gamma_0^2\omega_i^2} \quad (3.7)$$

$$\Phi = \left(\frac{\omega_0^2 \omega_i^2}{\gamma_0 \omega_i} \right) \quad (3.8)$$

Φ is just a dimensionless variable describing the frequency mismatch of driver and undriven system and Γ a rescaling of the driver amplitude. Discussing the stability of the different solutions of Eq. 3.6, one obtains the resonance curve of the driven van der Pol oscillator (Fig. 3.1). It shows that with increasing driver amplitude the observed oscillation amplitude increases as well as the frequency mismatch, which will still allow for successful synchronization. This dependence of the synchronization area and the driver amplitude is usually shown in plots like Fig. 3.2. Due to the shape such plots are called Arnol'd tongues.

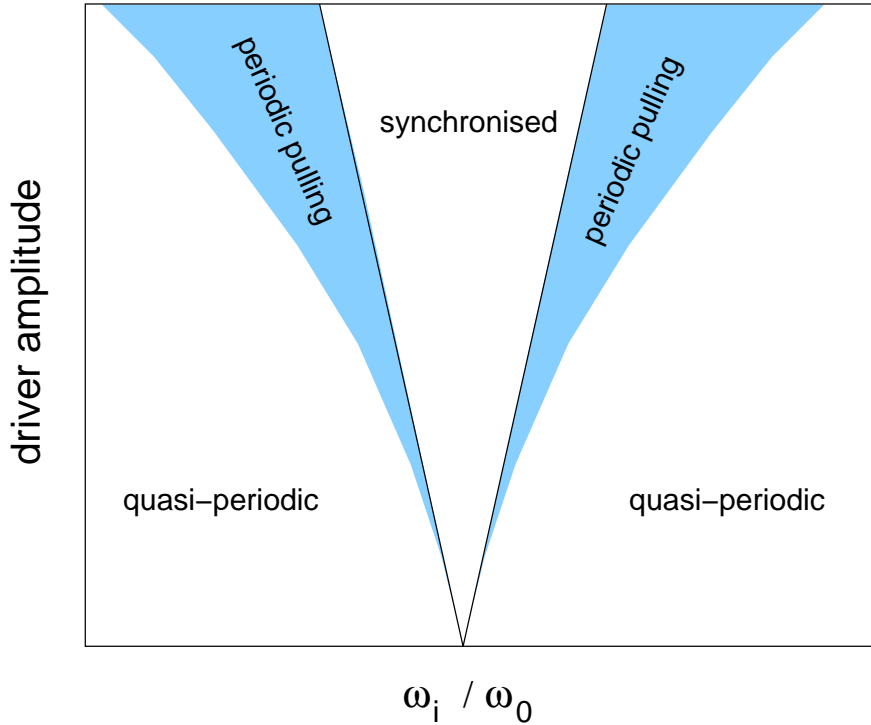


Figure 3.2: Schematic drawing of an Arnol'd tongue.

3.2.2 Incomplete synchronization

An important variation of the above described synchronization is the incomplete synchronization, which is usually referred to as periodic pulling. This phenomenon is observed close to the regime of synchronization, i.e. at the borders of the Arnol'd tongue (Fig. 3.2). Here, the oscillation frequency of the driven system is periodically pulled towards the external driver frequency, but the coupling of driver and system is too weak or the frequency mismatch too large to establish complete synchronization. Again, the simplicity of the van der Pol model allows for an analytic description of this dynamical phenomenon. Obviously, the pulling process does not only comprise an amplitude modulation, but a frequency modulation as well. Consequently, the ansatz to solve the van der Pol equation (Eq. 3.3 and 3.4) should have the form

$$\theta(t) = a(t) \sin(\omega_i t - \phi(t)). \quad (3.9)$$

With the approximations, that $a(t)$ and $\phi(t)$ vary slowly compared to ω_i , that the system shows only weak nonlinearity, and that driver frequency ω_i and system frequency ω_0 differ only slightly, one obtains differential equations for the temporal evolution of amplitude and phase.

$$\frac{da}{dt} = \frac{\gamma_0 a}{2} \left[1 - \left(\frac{a}{a_0} \right)^2 \right] + \frac{E \omega_0}{2} \cos \phi \quad (3.10)$$

$$\frac{d\phi}{dt} = (\omega_i - \omega_0) - \frac{E\omega_0}{2a} \sin\phi \quad (3.11)$$

In the limit $E \rightarrow 0$ and $\omega_i \rightarrow \omega_0$, the differential equations for the undriven van der Pol oscillator are obtained. However, Eq. 3.11 is identical to Adlers equations [96]

$$\frac{d\phi}{dt} = \Omega_0 (1 - \alpha \sin\phi) \quad (3.12)$$

with

$$\alpha = \frac{E\omega_0}{2a\Omega_0} \quad \text{and} \quad \Omega_0 = \omega_i - \omega_0 \quad (3.13)$$

Note, that Ω_0 is the usual modulation frequency of linearly superimposed oscillations and the amplitude a_0 corresponds to the oscillation amplitude of the undriven system.

For a time-independent phase relation $d\phi/dt = 0$ the system is synchronized. According to Eq. 3.12, this is only possible for $|\alpha| \geq 1$ or

$$\left| \frac{\Omega_0}{\omega_0} \right| \leq \frac{E}{2a}. \quad (3.14)$$

This means, synchronization is limited to an interval proportional to the driver amplitude. To describe periodic pulling Eq. 3.12 has to be integrated. The result is [97]

$$\tan\left(\frac{\phi(t)}{2}\right) = \frac{\Omega}{\Omega_0} \tan\left(\frac{\Omega t}{2}\right) + \alpha. \quad (3.15)$$

Ω defines the periodicity of $\phi(t)$ and is given by $\Omega = \Omega_0 \sqrt{1 - \alpha^2}$. With help of Eq. 3.13 the expression for Ω is usually written as

$$\Omega = \Omega_0 \sqrt{1 - \frac{\Omega_c^2}{\Omega_0^2}} \quad (3.16)$$

with $\Omega_c = E\omega_0/2a$ being the critical frequency, above which synchronization is observed. For $\alpha \rightarrow 1$, Ω approaches zero, e.g. the pulling process slows down until the system is synchronized for $\alpha = 1$. Further, the phase evolution is nonlinear (Fig. 3.3), i.e. the phase evolution has two different time-scales. For $\alpha \rightarrow 1$, the regime of slow phase evolution expands and the phase evolution slows down more and more, while the regime of fast phase evolution gets smaller and the evolution faster. Finally, $d\phi/dt = 0$ for $\alpha = 1$; the system is synchronized. For $\alpha \rightarrow 0$, the phase evolution approaches linearity and Ω reduces to Ω_0 .

Modulation processes generally produces characteristic side band structures in the power spectrum. To obtain the spectral characteristics for amplitude and phase modulation, Adlers Equation 3.12 can be solved [98]. The result is depicted in Fig. 3.4. For $\alpha \rightarrow 1$ the side bands get more and more pronounced and their distance Ω decreases. Further, the analysis shows that the power spectrum, associated with periodic pulling, has a characteristic triangular shape. This feature is very helpful to detect amplitude and phase modulation.

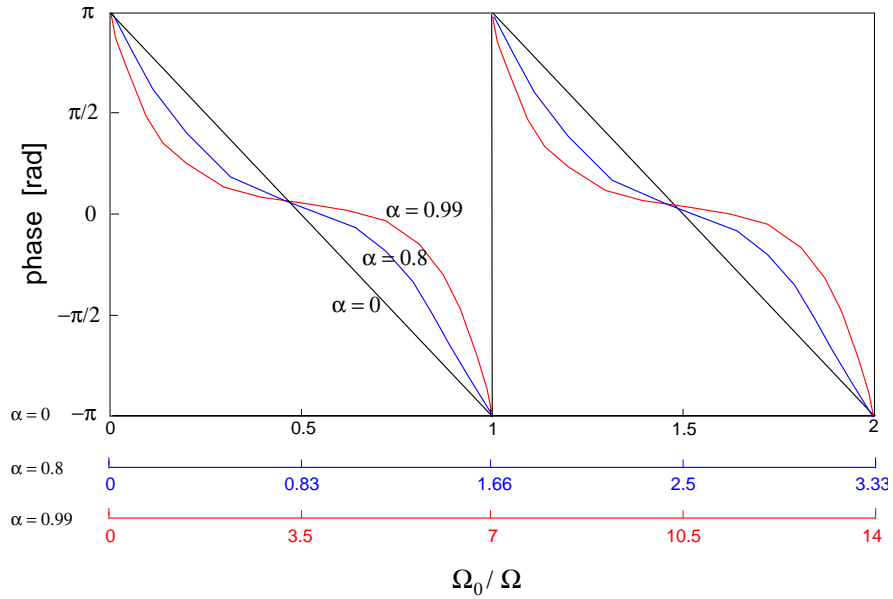


Figure 3.3: Temporal phase evolution between driver and system. Note the different Ω_0/Ω scales for the different α values.

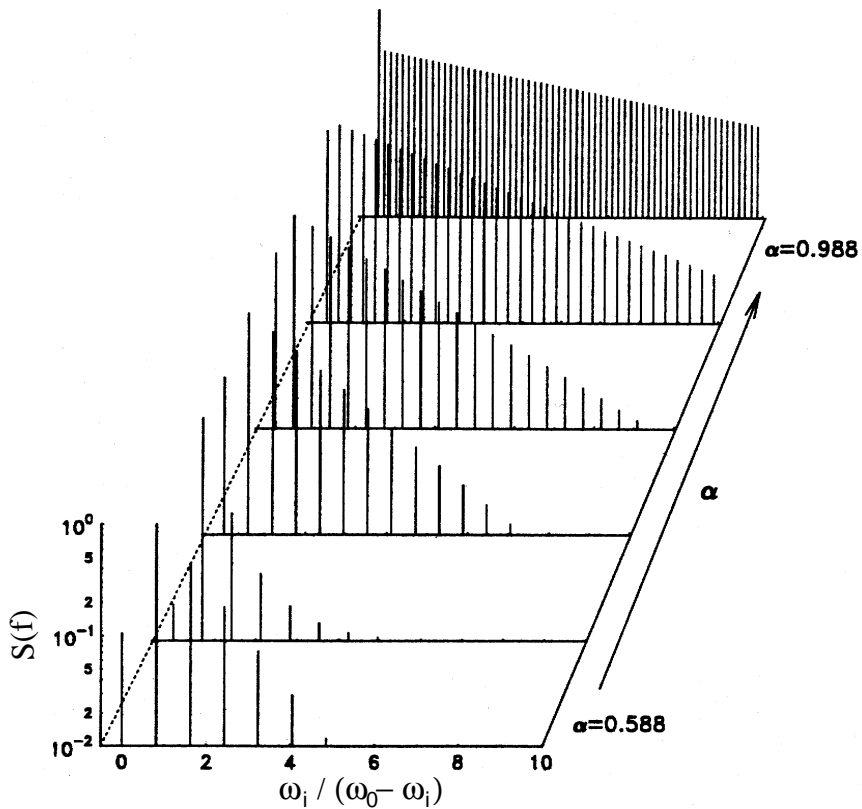


Figure 3.4: Calculated spectrum for periodic pulling and its dependence on α (from [97]).

3.3 Concluding remarks

An important point is that the van der Pol oscillator is described by a nonlinear, ordinary differential equation in one spatial dimension. This equation significantly differs from those of more complex systems like meta-stable guided ionization waves [99] or drift waves (chapter 2). They are described by a set of nonlinear, partial differential equations in two or more spatial dimensions. Nevertheless, these driven systems show qualitatively the same dynamical behavior. In the past, some attempts have been made to deduce van der Pol-like equations from fluid equations [52, 72]. For this purpose a new source term is added to the continuity equation. Unfortunately, the physical interpretation of this term is still open.

Chapter 4

Methods of data analysis

This chapter briefly introduces into the data analysis methods used in the following chapters, to avoid misunderstanding due to different definitions and normalizations used in literature. A detailed introduction into the statistical and spectral data analysis can found in [100]. The technique of phase sensitive data averaging is discussed in more detail, because it is a non-standard method.

4.1 PDF and central moments

One way to gain information on a fluctuating quantity $x(t)$ is to look at its Probability Density Function (PDF). The PDF $P(x)$ is defined as the probability to find x in the interval $[x, x + dx]$. Consequently,

$$\int P(x) dx = 1. \quad (4.1)$$

For discrete experimental data (x_n, P_n) the integration turns into a sum and the equation above changes to

$$\sum_n P_n = 1. \quad (4.2)$$

To describe the shape of a PDF commonly its central moments are used, which are defined by [101]

$$m_i = \langle (x - \langle x \rangle)^i \rangle \quad (4.3)$$

with $i \in [1, 2, 3, \dots]$ and $\langle x \rangle = \sum P_n x_n$ (mean value). A special interpretation has the second central moment, called variance,

$$m_2 = \langle x^2 \rangle - \langle x \rangle^2 = \sigma^2. \quad (4.4)$$

σ is called standard deviation and describes the mean deviation of $P_n(x)$ from the mean value $\langle x \rangle$. The third and fourth order moments are typically normalized with the standard deviation. While the skewness $s = m_3/\sigma^3$ gives information about the symmetry, the kurtosis $k = m_4/\sigma^4$ provides information about the shape of the tails of the PDF.

Throughout this work skewness and kurtosis are used to compare the PDF with the PDF of a Gaussian. Therefore, the kurtosis is redefined as $k = m_4/\sigma^4 - 3$, e.g. a PDF with $k < 0$ ($k > 0$) is less (more) peaked than a Gaussian PDF.

4.2 Correlation analysis

Quite often it is desirable to measure the correlation between two signals. The cross-correlation of two fluctuating quantities $a(x, t)$ and $b(x, t)$ is defined as the ensemble average of statistical independent realizations while shifting one quantity in space and time, e.g.

$$C_{a,b}(\Delta x, \Delta t) = \langle a(x, t)b(x + \Delta x, t + \Delta t) \rangle. \quad (4.5)$$

For $a = b$ the auto-correlation is obtained.

To compare different cross correlations a normalization is needed. Usually for this purpose the geometric average of the auto-correlation functions for $\Delta x = 0$ and $\Delta t = 0$ is used. Therefore,

$$R_{a,b}(\Delta x, \Delta t) = \frac{C_{a,b}(\Delta x, \Delta t)}{\sqrt{C_{a,a}(0, 0)C_{b,b}(0, 0)}}, \quad (4.6)$$

with $0 \leq R \leq 1$.

4.3 Spectral data analysis

Another standard tool are Fourier methods to gain spectral informations on time series. The spectral power density of a fluctuating quantity $a(x, t)$ is defined as

$$S(k, \omega) = \langle |\hat{a}(k, \omega)|^2 \rangle, \quad (4.7)$$

with $\hat{a}(k, \omega)$ being the complex Fourier transform of $a(x, t)$. For two fluctuating quantities this can be generalized to give the cross power density spectrum

$$S_{a,b}(k, \omega) = \langle \hat{a}^*(k, \omega)\hat{b}(k, \omega) \rangle. \quad (4.8)$$

Because $S_{a,b}(k, \omega)$ is complex, $|S_{a,b}(k, \omega)|$ quantifies the coupling of amplitudes, while the information on the average phase shift between $a(x, t)$ and $b(x, t)$ is given by

$$\alpha_{a,b} = \arg S_{a,b}(k, \omega). \quad (4.9)$$

Introducing a normalization with the geometric average, the cross coherence spectrum

$$\gamma_{a,b} = \frac{|S_{a,b}(k, \omega)|}{\sqrt{S_{a,a}(k, \omega)S_{b,b}(k, \omega)}} \quad (4.10)$$

is obtained.

Using two simultaneous recordings of the same quantity at positions separated by Δx , the local wave number spectrum $S_l(k, \omega)$ can be approximated. The local wave number k is approximated by the signal phase shift α by $k = \alpha/\Delta x$. Now, $S_l(k, \omega)$ is computed by

$$S_l(k, \omega) = \frac{1}{N} \sum_i I_{[0, \Delta k]}(k - k_i(\omega)) S_i(\omega). \quad (4.11)$$

with the indicator function $I_{[0, \Delta k]}(x)$ being 1 for $x \in [-\Delta k/2, \Delta k/2]$ and $S_i(\omega)$ denoting the mean value of the power density of both recordings of the i -th of N ensembles. Due to the localized measurement this method reaches its limits for turbulent signals. In this case, much better results are obtained using probe arrays and calculation of the frequency wave number spectrum by direct Fourier transform [35].

4.4 Spectrally resolved transport

For the investigation of fluctuation-induced transport it is important to obtain the transport with spectral resolution to identify the importance of different frequency regimes. Usually only the average transport is of interest. It is defined as

$$\langle \Gamma \rangle = \langle \tilde{n} \tilde{v} \rangle = \frac{1}{B} \langle \tilde{n} \tilde{E} \rangle = \frac{1}{B} R_{\tilde{n}, \tilde{E}}(0). \quad (4.12)$$

Applying the Wiener-Khintchine-Theorem [102], the cross-correlation function can be replaced by the inverse Fourier transform of the spectral cross-power density $S_{\tilde{n}, \tilde{E}}(\omega)$, i.e. the transport can be expressed by

$$\langle \Gamma \rangle = \frac{2}{B} \Re \int_0^\infty S_{\tilde{n}, \tilde{E}}(\omega) d\omega. \quad (4.13)$$

Splitting the spectral cross-power density into co- and quad-spectrum, i.e.

$$S_{\tilde{n}, \tilde{E}}(\omega) = C_{\tilde{n}, \tilde{E}}(\omega) + iQ_{\tilde{n}, \tilde{E}}(\omega) \quad (4.14)$$

the spectral transport can be defined by

$$\Gamma(\omega) = \frac{2}{B} C_{\tilde{n}, \tilde{E}}(\omega), \quad (4.15)$$

consequently

$$\langle \Gamma \rangle = \int_0^\infty \Gamma(\omega) d\omega. \quad (4.16)$$

Therefore localized measurements of \tilde{n} and \tilde{E} allow for a spectrally resolved transport estimation [37].

4.5 Phase sensitive data averaging

In general, a fluctuating quantity $a(x, t)$ can be split into three parts, a stationary part a_{stat} , coherent fluctuations a_{coh} , and stochastic fluctuations a_{stoch} .

$$a(x, t) = a_{stat}(x) + a_{coh}(x, t) + a_{stoch}(x, t) \quad (4.17)$$

a_{stat} is easily computed by time averaging. To split the remaining fluctuations into coherent and stochastic parts, a phase sensitive method is needed. Recently the technique of conditional averaging [103] has gained interest in plasma turbulence research [30, 104, 105]. This method uses the *a priori* assumption ($a_{cond} \in [a_{coh}(x, t)]$) to select a sub-ensemble from the ensemble, i.e.

$$\langle a(x, t) \rangle_{cond} = \langle a(x, t) | a(x', t') = a_{cond} \rangle. \quad (4.18)$$

Averaging over such a sub-ensemble will cancel out all stochastic contributions for a sufficiently large ensemble. The coherent part will remain, if the assumption on a_{cond} is valid. In practice problems arise due to the selection of proper conditions. A common procedure to detect coherent structures are threshold values. Unfortunately, in most turbulent systems the fraction of coherent fluctuations detectable with this method is much smaller than the contribution of the remaining fluctuations. Consequently, very long time-series are needed. This drastically changes if the technique is applied to a synchronized system. Here, the coherent fraction is dominant and the driver signal is phase-locked with this fraction. Therefore, the driver signal can be used as phase reference.

A more illustrative explanation can be given with help of Fig. 4.1 a-d. In this example, the plasma is assumed to contain a $m = 2$ density perturbation propagating azimuthally in a cylindrical plasma column. This perturbation is synchronized by an external, sinusoidal driver signal. Due to the synchronization their phases are locked. Time-series of density fluctuations are recorded with a radially movable probe at different radial positions (a). Simultaneously, the driver signal is recorded. The phase shift between different radial positions is random due to the sequential data recording. This destroys the spatial information although the temporal periodicity can be clearly seen, but the known phase shift between system and driver signal can be used to reconstruct this information and to remove the stochastic fluctuations. For this purpose two periods of the driver signal are assumed to be equivalent to a azimuthal period. Either this assumption can be verified by calculation of a local frequency wave number power spectrum or it can be directly obtained from the spatial component of the driver signal. With the known periodicity the time-series at each radial position can be split into an ensemble of time-series, each comprising the density fluctuations of one azimuthal circumference (b). The stochastic fluctuations can now be removed by averaging over the ensemble. The remaining coherent signal fraction is shown in (c). Repeating this procedure for all radial positions allows to reconstruct the coherent fluctuations spatially (d).

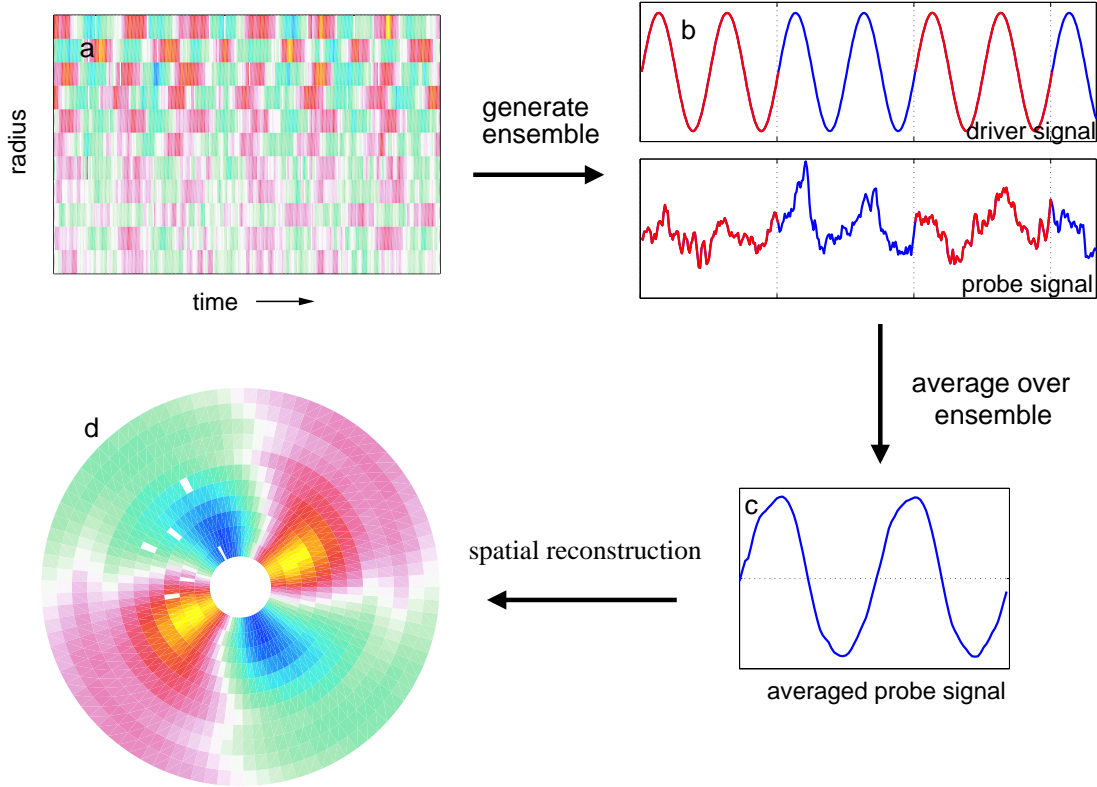


Figure 4.1: (a) density fluctuations as function of time and radius. The phase between two radial positions is random. (b) time-series of driver signal and density. The sub time-series are separated by the dashed lines. (c) time-series of the driver signal and the ensemble averaged probe signal. (d) spatial reconstruction using the averaged data at different radial positions.

The benefit of this method is that each data point is used for data evaluation. This increases the size of the ensemble and improves the averaging process. To reconstruct the coherent density perturbation shown in (d) two time-series each consisting of 256k samples have been used for each radial position. Despite of the high sampling rate of 1 Msamples - leading to a high azimuthal resolution - the ensemble size is still of the order of 2000. Further, 2D spatial information is obtained by a 1D measurement.

The limitations of this method are related to the averaging process. Although the filter characteristic of this method is narrow-band the averaging process does not only extract the coherent fluctuations at the chosen frequency, but also at its harmonics. Further, this method is not capable to distinguish between two waves of the same frequency, but with opposite propagation direction.

Chapter 5

Experiment and diagnostics

This chapter concentrates on the description and characterization of the KIWI experiment. In the center of interest is, besides the technical details, a description of the plasma equilibrium, the plasma fluctuations and the relation of both with the aim to demonstrate that this plasma system is well understood. The observed fluctuations will be analyzed and compared with theory given in chapter 2. Furthermore, this chapter will introduce into the basic diagnostics which are used to obtain the results presented in the following chapters.

5.1 Technical description

The KIWI is a linear magnetized device consisting of three parts (Fig. 5.1). The two source chambers at the ends are connected via a magnetized midsection. The plasma is produced inside the source chambers by a thermionic hot-cathode discharge in Argon. Typical discharge parameters are listed in Table 5.1. By using additional field coils, operated in cusp geometry, the magnetic field of the midsection can be almost compensated to reduce magnetic mapping [106] (Fig. 5.2). Further, a multi-dipole magnetic field configuration in line cusp geometry is used to increase the ionization efficiency of the primary electrons [107]. Besides this, the enhanced residence time

Parameter	Minimum	Typical	Maximum
base pressure	$5 \cdot 10^{-5} \text{Pa}$		$2 \cdot 10^{-4} \text{Pa}$
neutral gas pressure	$5 \cdot 10^{-2} \text{Pa}$	$1 \cdot 10^{-1} \text{Pa}$	$5 \cdot 10^{-1} \text{Pa}$
discharge voltage	40 V	65 V	65 V
discharge current	5 A	8 A	12 A
grid voltage	0 V	6 V, 12 V	16 V
magnetic field (midsection)		0.07 T	0.15 T

Table 5.1: *Important parameters of operation of the KIWI.*

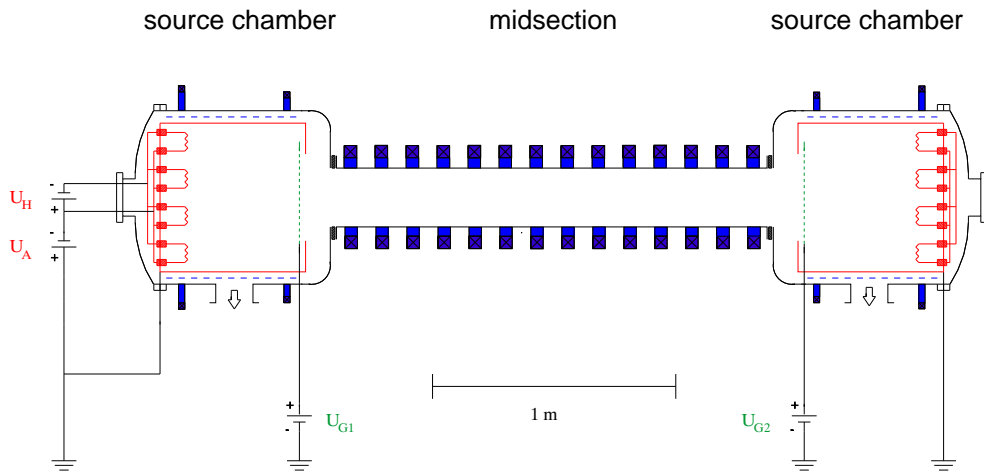


Figure 5.1: Schematic drawing of the KIWI device. The components for the magnetic field generation are printed in blue. The red parts belong to the discharge. The biased grid is marked green.

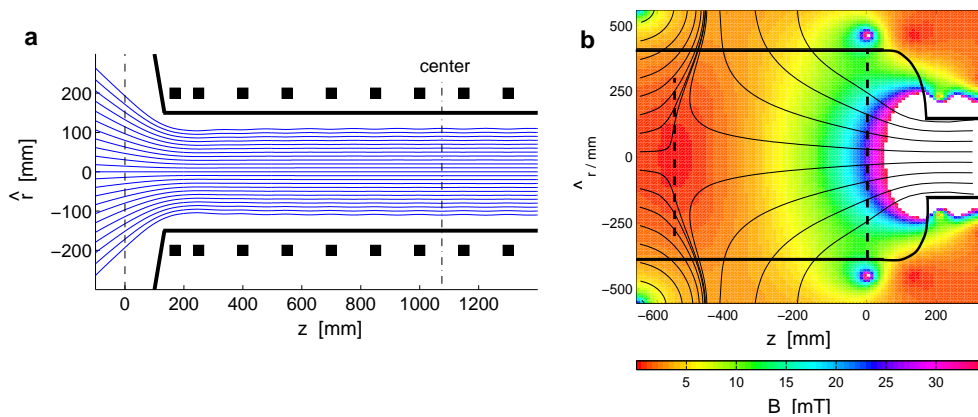


Figure 5.2: Magnetic field line calculations for (a) the midsection and (b) the source chamber. The field line density in (b) does not reflect the strength of the magnetic field.

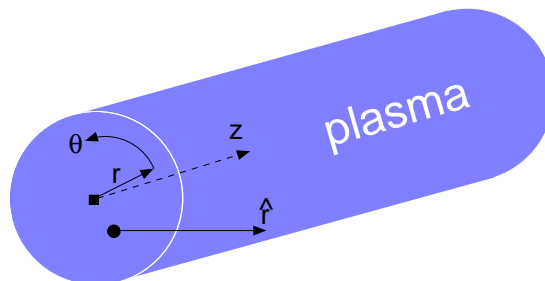


Figure 5.3: Schematic drawing of coordinate definition. The solid square marks the center of the plasma column while the solid circle denotes the geometric center of the KIWI device.

of the charged particles in the source chamber leads to a better thermalization of the plasma. Therefore, the velocity distribution function is almost Maxwellian [108]. The source chambers and the midsection are separated by biased stainless steel mesh grids with a transparency of 68%. The magnetic field in the midsection is homogeneous with a magnetic field ripple of less than 5%, except for the ends. Here, the limited number of field coils leads to diverging field lines (Fig. 5.2).

An important feature of the KIWI is its steady state operation with stable plasma conditions for several hours. This founds the basis for measurements with high spatial and temporal resolution. Additionally, long time series assure reasonable statistics. Further details about the KIWI can be found in [109].

For the investigations described in this work only one chamber is operated. The separation grid at the active source chamber is positively biased with respect to ground while the other grid is connected to ground as well as all parts of the inactive chamber.

Due to the symmetry of the device cylindrical coordinates are used subsequently. In most cases the radial coordinate r is chosen to be zero at the center of the plasma column. Exceptions from this will be marked by \hat{r} . Here, zero will mark the geometric center of the device. In all cases the axial coordinate will be labeled z and its origin marks the position of the active grid while θ denotes the azimuthal coordinate (Fig. 5.3).

5.2 Diagnostics

5.2.1 Electrostatic probes

The main diagnostic tool used for this work are electrostatic or Langmuir probes [110]. These are small electrodes (diameter: 100 μm , length: 4-5 mm) immersed into the plasma. Due to the possibility to mount them on small carriers, the disturbance of the plasma is very localized and can therefore be neglected. Additionally, they allow for an excellent spatial and temporal resolution compared to wave diagnostics. To measure the plasma parameters with such a probe, usually a current voltage characteristic is recorded. A typical characteristic is shown in Figure 5.4. It consists of three parts: The **ion saturation regime** is entered if the probe is biased strongly negative with respect to the plasma potential. Due to the fairly high negative bias, all electrons are repelled from the probe and only positively charged ions¹ reach the probe. The ion saturation current is given by [111, 112]

$$I_{i,sat} = 0.61neA\sqrt{\frac{k_B T_e}{m_i}} \quad (5.1)$$

with A being the effective probe surface. The region above the plasma potential is called **electron saturation regime**. Here, the all electrons are attracted by the probe

¹In the KIWI device only single charged positive ions are observed.

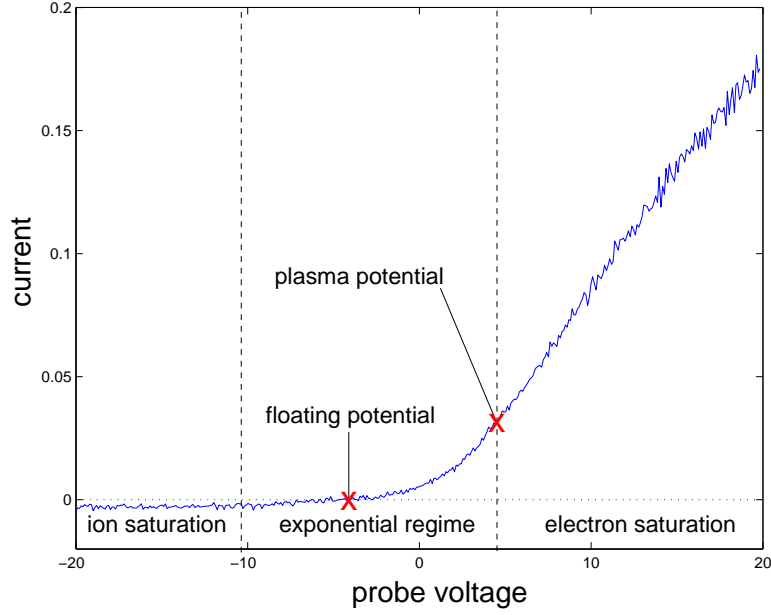


Figure 5.4: Typical current voltage characteristic of a Langmuir probe. The three characteristic regimes are marked as well as the plasma potential ϕ_p and the floating potential ϕ_{fl} .

and the ions are repelled. In contrast to the ion saturation regime, the electron saturation current depends on the probe shape. For planar probes a real saturation is observed while for cylindrical and spherical probes the current increases monotonically. This is mainly caused by an increase of the attraction area with probe voltage. Consequently, the electron saturation current is only well defined at the plasma potential. The electron saturation current at the plasma potential is given by

$$I_{e,sat} = -neA\sqrt{\frac{k_B T_e}{2\pi m_e}}. \quad (5.2)$$

In between both regimes only a part of the electrons is attracted, namely those with sufficient kinetic energy to overcome the potential barrier. This part is called **exponential regime**. Assuming a Maxwellian velocity distribution the pure electron current $I_e = I - I_{i,sat}$ depends exponentially on the applied voltage U

$$I_e(U) = I_{e,sat} \exp\left(\frac{e(U - \phi_p)}{k_B T_e}\right). \quad (5.3)$$

Another important point of the probe characteristic is the floating potential ϕ_{fl} . At this point the probe is current free, i.e. the electron and ion currents compensate each other. For a plane probe immersed in an Argon plasma the floating potential and the plasma potential are related by

$$\phi_{fl} = \phi_p - 4.7 \frac{k_B T_e}{e}, \quad (5.4)$$

assuming that $T_i \ll T_e$.

From the probe characteristic the crucial parameters T_e and n_e are obtained with help of Eq. 5.2 and Eq. 5.3. A more detailed discussion on probe diagnostics is given in [111, 112]. Especially [113] discusses the analysis algorithms used at this experiment in detail and pays special attention to the complications related to magnetized plasma.

Dealing with fluctuating plasma parameters of the form

$$n = n_0 + \tilde{n}, \quad \phi = \phi_0 + \tilde{\phi} \quad \text{and} \quad T_e = T_{e0} + \tilde{T}_e \quad (5.5)$$

the time needed for a complete characteristic acquisition has to be shorter than the time scale of the fluctuations. Technically this is extremely difficult. A different method can be used if the temperature fluctuations are negligible. With this assumption, Eq. 5.1 and 5.4 give

$$\tilde{n} \approx \frac{\tilde{I}_{i,sat}}{\sqrt{T_{e0}}}. \quad (5.6)$$

$$\tilde{\phi}_p \approx \tilde{\phi}_{fl}. \quad (5.7)$$

These equations show that time series recordings of floating potential and ion saturation current give sufficient estimates for fluctuations of density and plasma potential. The condition of $\tilde{T}_e \ll T_{e0}$ is realistic for the low and quite homogeneous electron temperatures observed in KIWI (Fig. 5.12).

5.2.2 Special probes

A modification to Langmuir probes are emissive probes. They are used to obtain the plasma potential from a simple floating potential measurement. For this purpose emissive probes use a heated tungsten wire to emit electrons. Regulating the heating current through the probe, the electron emission can be adapted to produce a nearly symmetric current voltage characteristic. The result is, that the floating potential becomes nearly identical with the plasma potential [112]. Compared to Langmuir probes, emissive probes allow for a fast and more accurate determination of the plasma potential and its fluctuations by floating potential measurements. Nevertheless, due to the electron emission its influence on the plasma is less localized and it might disturb other probes nearby. For this reason it is only used to determine the equilibrium plasma potential.

To measure the fluctuation induced transport with high resolution, two special probe constructions are used, double and triple probes (Fig. 5.5). The two Langmuir probes of the double probe are both operated to measure the floating potential. Due to their radial alignment the radial electric field fluctuations can be deduced. The triple probe consist of three Langmuir probes. Their spatial arrangement is shown in Fig. 5.5. The angle between the probes guarantees for an almost radial orientation of the probes. The distance between two neighboring probes is about 4 mm. The two outer probes are used to record floating potential fluctuations while the central probe is negatively biased to record ion saturation current fluctuations. Therefore, this probe is used to obtain the local fluctuation-induced transport in radial direction.

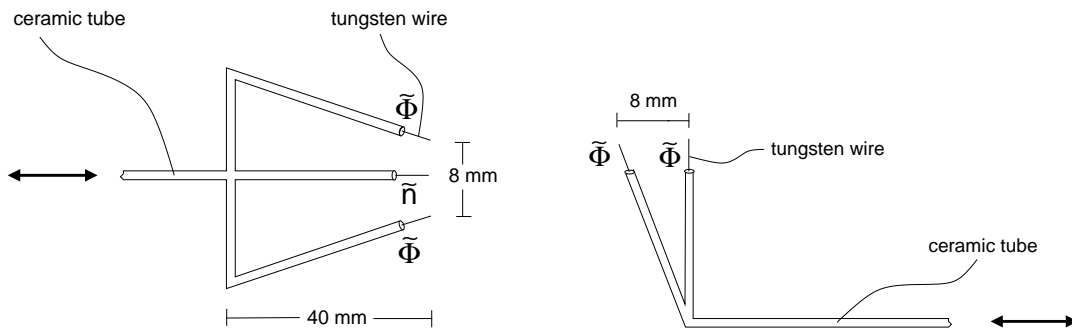


Figure 5.5: Construction sketch of triple probe and double probe tips. The electric connectors and the mounting points are not depicted. The typical direction for movements is indicated by arrows.

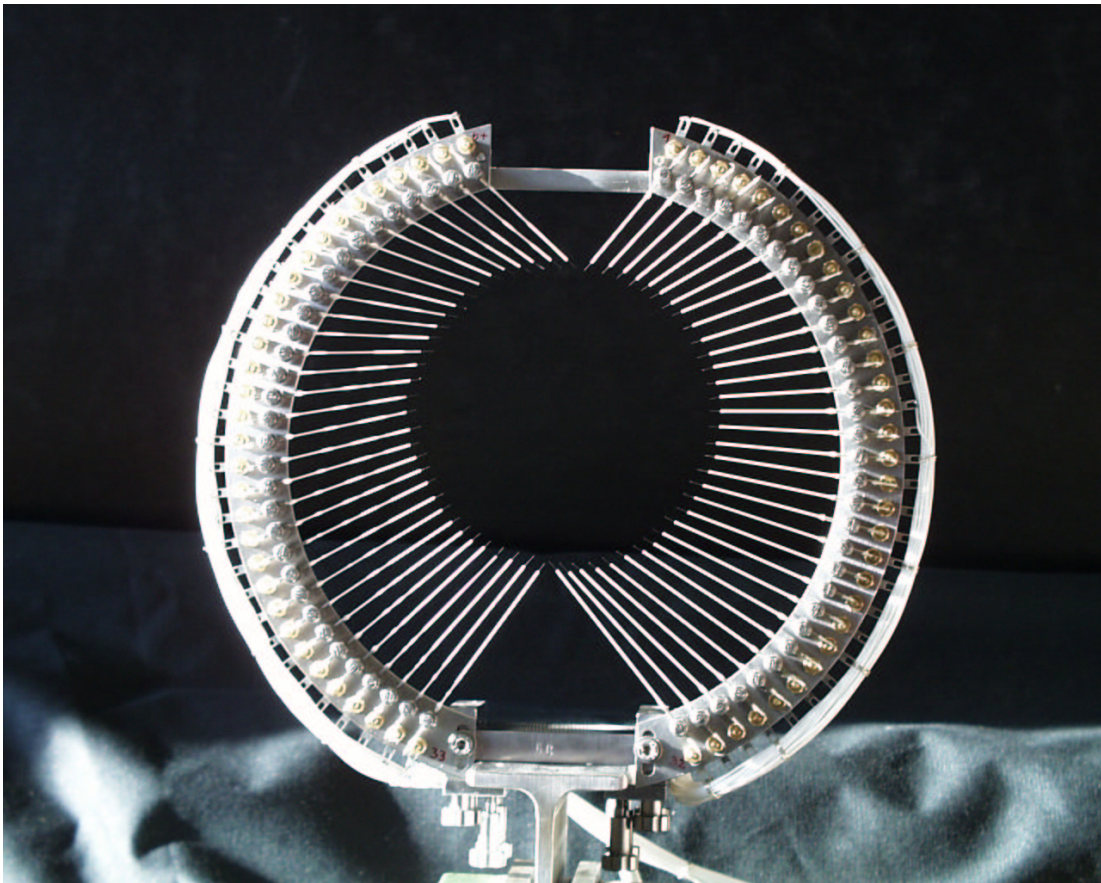


Figure 5.6: Picture of the re-designed 64 probe array. The 64 Langmuir probes are adjusted to follow an equi-potential contour with 9 cm diameter. The inner diameter of the stainless steel ring is 18 cm.

5.2.3 Probe arrays

To gain detailed spatio-temporal information about the plasma fluctuations a circular probe array consisting of 64 regular spaced probes is used. The benefits of such a probe array have been shown in previous investigations [80, 35, 114]. The instantaneous observation at many azimuthal positions turned out to be a useful tool to investigate the complex, turbulent drift wave dynamics. To use this diagnostic in conjunction with the new probe positioning system, the probe array has been re-designed and optimized (Fig. 5.6). A new feature is the possibility to tilt each probe. This allows for an equidistant probe arrangement on arbitrary contours. The probes are negatively biased to record ion saturation current fluctuations.

5.2.4 3D probe positioning system

To have full access to all plasma positions a new probe positioning system is developed. An important feature of this positioning system is its coordinate system. The positioning system consists of two rings which are connected via two bars (Figs. 5.7 and 5.8). This construction is immersed into the midsection of the KIWI. A carriage is mounted on one of these bars. It carries one or more probes and can move along the z-axis. An additional drive provides the possibility of radial probe movements. Due to the possibility to rotate the whole construction the probe can move azimuthally as well. These cylindrical coordinates reflect the geometry of the KIWI and of the plasma column (see Sect. 5.3). Therefore, probes can easily move without changing probe orientation with respect to the plasma column and the magnetic field. This is a major advantage compared to former probe positioning systems, because the fixed probe orientation allows for purely radial or azimuthal field measurements. Further, it is easily calibrated to give absolute positions with respect to the vacuum vessel and therefore allows for an improved adjustment of probes, array and exciter to certain positions in the plasma column. Especially, the centering of the exciter with respect to the plasma column is very important to achieve an optimized performance. The positioning system is mainly used to obtain the equilibrium plasma parameters and fluctuation profiles from Langmuir probe measurements.

5.2.5 Exciter

To influence the plasma dynamics an octupole arrangement of electrodes (exciter) is used. Each electrode is 20 cm long and 2.5 cm wide. The eight electrodes are arranged on a circumference with variable diameter to adjust them with respect to the width of the plasma column. The radial position of the electrodes can be varied between 2.6 cm and 5.2 cm, even under vacuum conditions. The driver signals are generated with a 8 channel analog output card. Each analog output is connected via a power amplifier to its corresponding electrode. Peak to peak driver amplitudes of 50 V can be achieved, but for typical operation amplitudes below 10 V are used. Frequencies up to 30 kHz

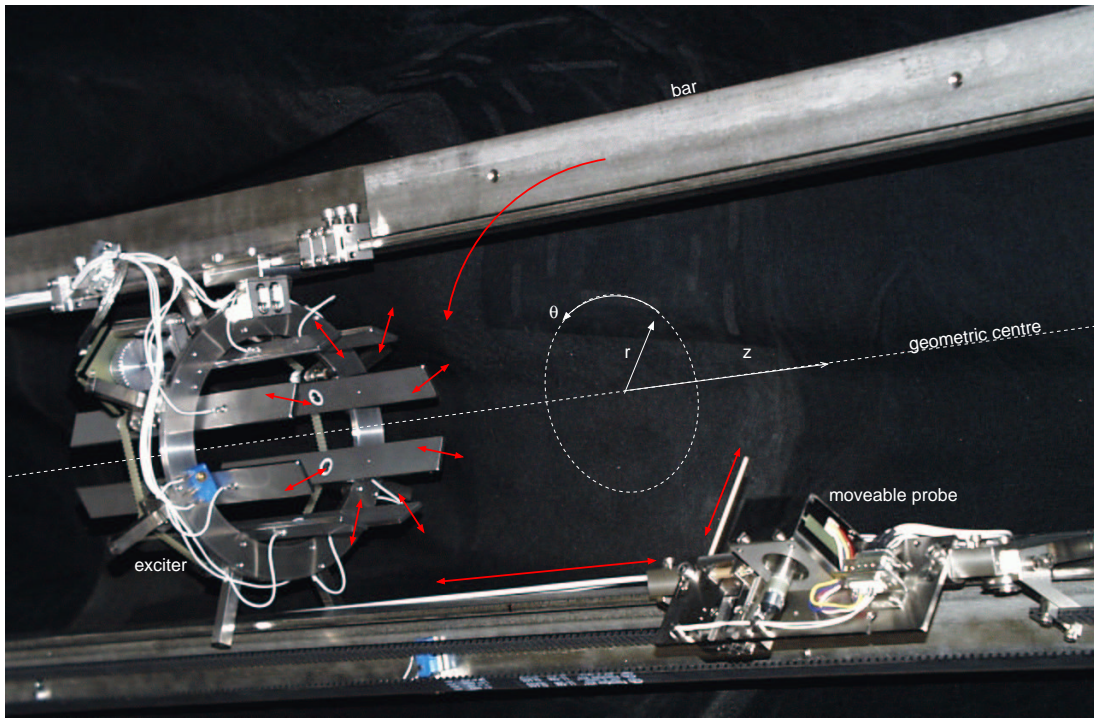


Figure 5.7: Pictures of the 3D probe positioning system and the exciter. The red arrows mark the direction of possible movements. The geometric center (dashed line) and a sketch of the coordinate system are added for orientation.

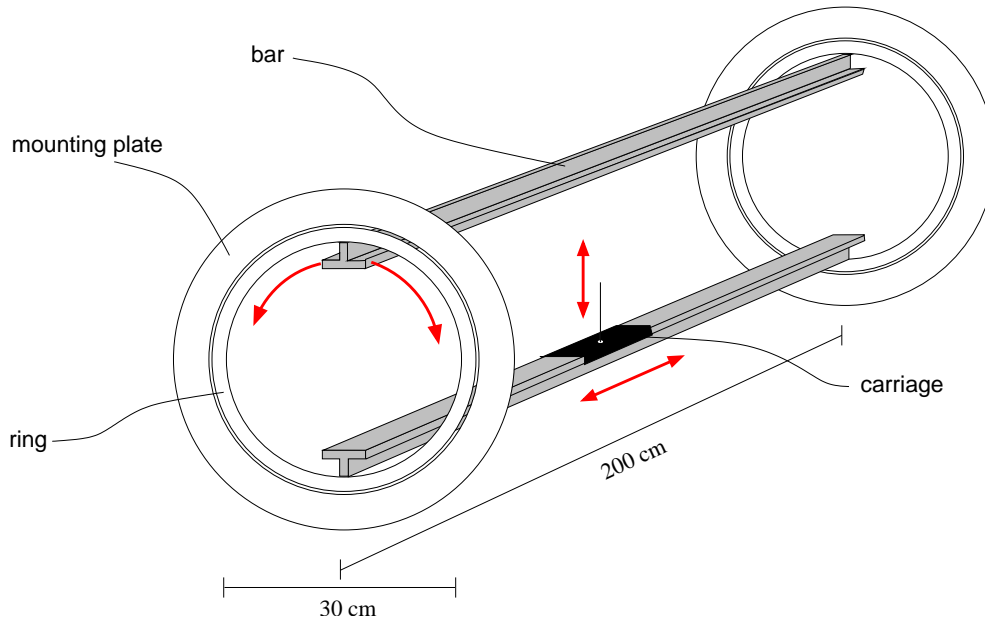


Figure 5.8: Sketch of the 3D probe positioning system. The arrows mark the direction of possible movements.

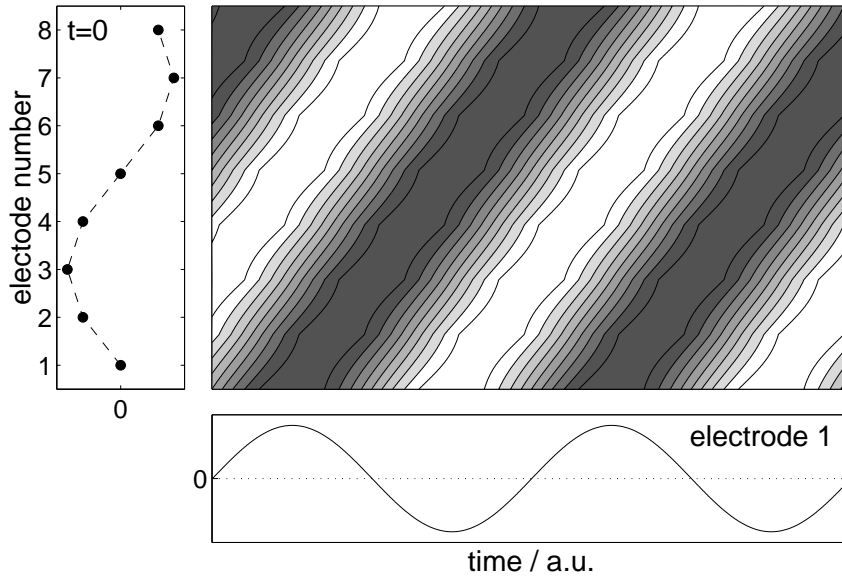


Figure 5.9: *Contour plot of the spatio-temporal structure of the octupole exciter signal. To each electrode a sinusoidal signal is applied (e.g. time series of signal applied to electrode 1). Due to the constant phase shift between each electrode, a sinusoidal shape is also apparent in azimuthal direction (e.g. at $t = 0$). In total, the azimuthal structure propagates upwards due to the time evolution of each channel.*

can be generated with a fixed phase relation between each channel. The phase relation is software controlled and can be chosen independently for each channel. Throughout this work, the phase shift between neighboring channels is constant. Fig. 5.9 shows a contour plot of a typical set of signals applied to the exciter as a function of time. As a consequence of the fixed phase shift, the sinusoidal variation in each channel leads to an azimuthally propagating wave pattern. The sign of the phase shift decides about the propagation direction while the frequency determines the propagation velocity. The wave length is controlled by the size of the phase shift. To really obtain a propagating wave, the wave length has to be chosen with respect to the periodical boundary conditions. Due to the number of electrodes, the Nyquist frequency limits the generation of modes to mode numbers $m_E=0$ to 3. Despite of an improved design allowing for more flexibility and electrode positioning, a main difference to earlier investigations [80] is that this electrical setup allows to draw a current to each electrode.

5.2.6 Positions of diagnostics

The axial position of the exciter is fixed at $z = 400$ mm. This assures that the exciter plates are aligned along the magnetic field lines and that they are not influenced by the magnetic inhomogeneity close to the grid. The double and triple probe are mounted at $z = 650$ mm. They are well separated from the exciter to assure that the observed dynamics are not limited to the exciter position.

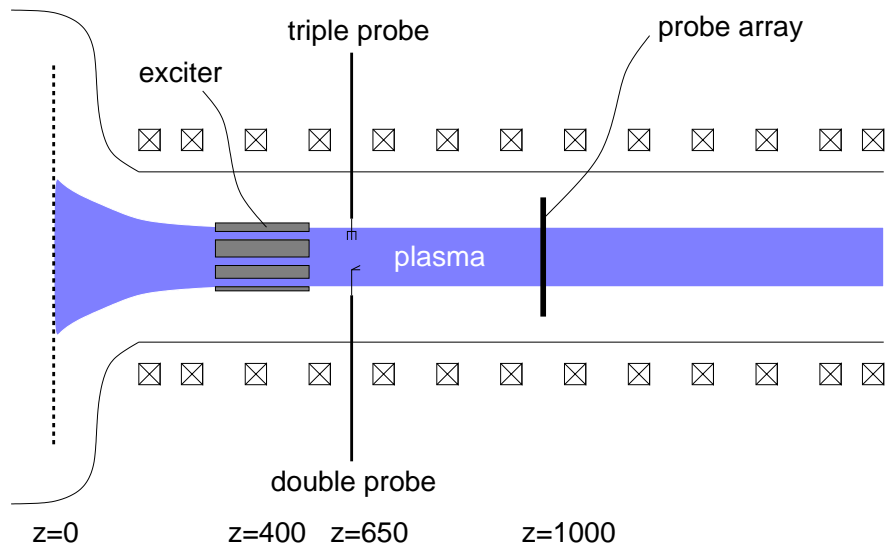


Figure 5.10: Positions of different diagnostics

5.2.7 Data acquisition

To control the data acquisition a modular structured program is written using LabWindows CVI. This program basically concentrates on the control of the different positioning systems, the data storage and the triggering and synchronization of data acquisition events. The data acquisition itself is done by spectrum analyzers, software controlled MIO-PC cards, and transient recorders.

5.3 Characterization of the plasma

Although there have already been several investigations of the plasma equilibrium and the different types of observable fluctuation in the past [115, 116], it was found to be necessary to re-investigate this. First, after almost ten years of use a major maintenance of the whole device was unavoidable. Therefore, it has to be shown that the experimental conditions stayed unchanged. Second, triggered by the capabilities of the new probe positioning system it is possible to obtain 3D information about the plasma conditions along almost the entire column. Especially, the 2D sections perpendicular to the magnetic field are required to center the exciter with respect to the plasma column and to choose a proper exciter radius. Furthermore, the spatially resolved measurements might give new insight into the dynamics of the fluctuations and could be used to consolidate their previous identification as drift waves [80]. However, by choosing comparable discharge conditions the following measurements allow for a better reliability of deduced quantities (Tab. 5.2).

parameter	typical value
electron temperature	1.5 eV
ion temperature	0.03 eV
plasma density	$1.0 \cdot 10^{16} \text{m}^{-3}$
electron plasma frequency	$1.6 \cdot 10^9 \text{ Hz}$
electron cyclotron frequency	$2.0 \cdot 10^9 \text{ Hz}$
electron thermal velocity	$7.0 \cdot 10^5 \text{ ms}^{-1}$
diamagnetic electron drift velocity	$1.2 \cdot 10^3 \text{ ms}^{-1}$
electron gyro radius	$4.0 \cdot 10^{-5} \text{ m}$
ion plasma frequency	$5.8 \cdot 10^6 \text{ Hz}$
ion cyclotron frequency	$2.7 \cdot 10^4 \text{ Hz}$
ion thermal velocity	$3.8 \cdot 10^2 \text{ ms}^{-1}$
ion sound velocity	$1.9 \cdot 10^3 \text{ ms}^{-1}$
ion gyro radius	$2.2 \cdot 10^{-3} \text{ m}$
plasma β	$1.0 \cdot 10^{-6}$
Debye length	$5.1 \cdot 10^{-5} \text{ m}$
effective gyro radius	$1.6 \cdot 10^{-2} \text{ m}$
density gradient length	$2.0 \cdot 10^{-2} \text{ m}$
mean free path for electron-neutral collisions	1 m
mean free path for ion-neutral collisions	0.3 m

Table 5.2: *Typical plasma parameters and deduced quantities observed in the KIWI. Plasma parameters with radial dependency were taken at plasma center to calculate deduced quantities. The plasma is assumed to be quasi neutral.*

5.3.1 Plasma equilibrium

To characterize the plasma equilibrium, basically two plasma parameters play an essential role, plasma density and plasma potential. As their equilibrium profiles have strong influence on plasma stability it is essential to investigate them in detail. It has to be stressed, that throughout this work equilibrium does not mean a thermodynamic equilibrium in the classical sense. Rather it is used to describe the dynamic balance of sources, sinks and transport processes on time average. This includes that the plasma parameters do not have to be constant in time, only their average values are constant. The qualitative findings presented below are almost independent of the discharge parameters. Therefore, all equilibrium profiles are obtained at a grid bias of $U_g = 6 \text{ V}$.

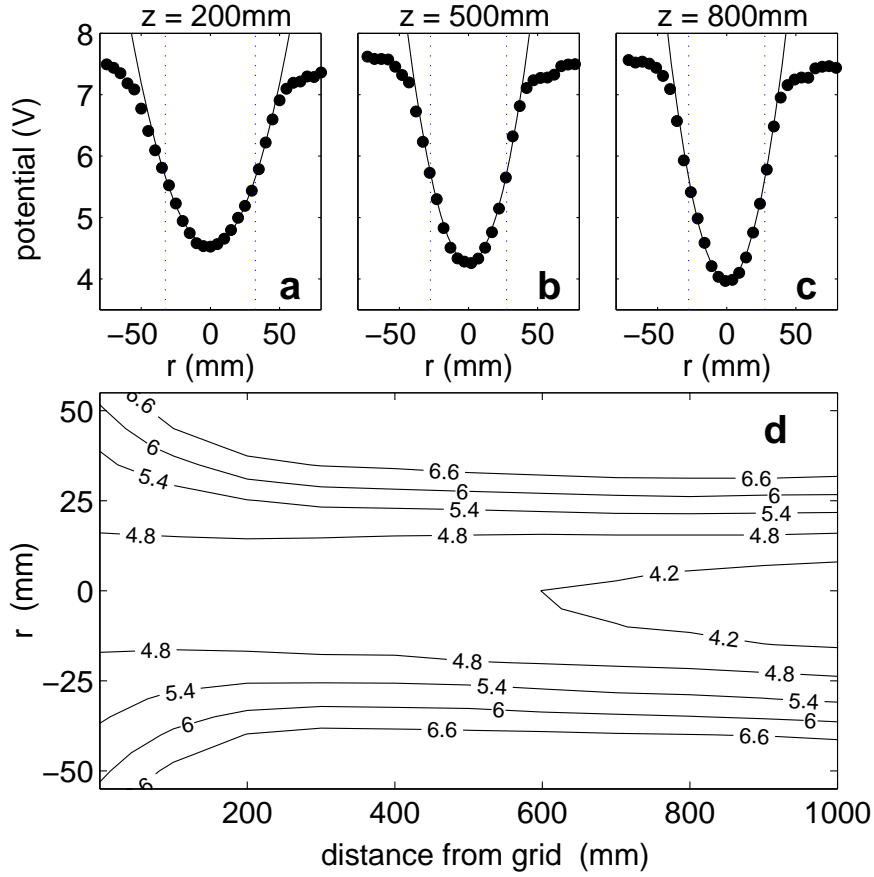


Figure 5.11: (a)-(c) show radial plasma potential profiles at different axial positions. The solid lines are least square fits of parabolas to the measurements. The positions of maximum density gradient are marked with dotted lines. The plasma potential contour (d) shows a cross section in the rz -plane through the center of the plasma column.

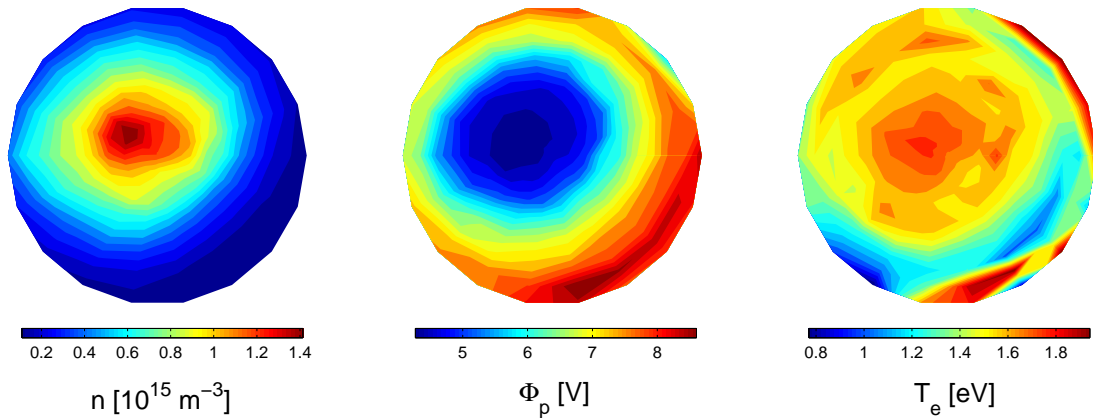


Figure 5.12: Electron density, potential, and temperature profiles perpendicular to B . The crosssection diameter is 10 cm.

Plasma potential

A typical potential profile for the KIWI device is shown in Figs. 5.11 and 5.12. While the first shows a section along r and z , the second represents a cross section perpendicular to z . From this cross section it is evident, that the choice of cylindrical coordinates is meaningful. Due to the rotational symmetry it is sufficient to restrict the following discussion to the contour plot Fig. 5.11d. Obviously the potential profile can be divided into two regions with different structural elements. While the region $z > 200$ mm is fairly uniform, a fringing of the equi-potential surfaces is observed for $z \leq 200$ mm. A comparison with the magnetic field (Fig. 5.2) reveals that in this region the equi-potential surfaces follow the fringing magnetic field lines. This is not surprising for a low- β plasma (see Tab. 5.2), where the charged particles can only move freely parallel to \mathbf{B} .

Because of the linear geometry of the KIWI, the magnetic field lines in the midsection end on both sides on grids. As these grids are differently biased, there is a voltage drop between them. For the presented experiments the active grid ($z = 0$ mm) is positively biased while the other grid ($z = 1800$ mm) is grounded, i.e. there is a voltage drop of 6 V between the grids. Having a look at Fig. 5.11d, a voltage drop is indeed observed, but it is much smaller than 6 V. The reason for this is that the grids act as a boundary. Consequently they are shielded by the plasma. This Debye shielding will lead to a significant potential drop within a few Debye length. As the Debye length is even at the radial boundary of the plasma column in the millimeter range this potential drop can not be resolved by probe measurements. Nevertheless, the remaining axial electric field can be explained by the plasma resistivity [117] and is in good agreement with previous measurements [116].

It is worth to have a close look at the radial component, because non-vanishing radial potential gradients cause azimuthal $\mathbf{E} \times \mathbf{B}$ -drifts, which are known to be a destabilizing mechanism for drift waves [19] (see chapter 2 for details). To simplify the following discussion Figs. 5.11a-c show the radial potential profile at three different axial positions. The discussion is restricted to the central part ($r \leq 40$ mm) of the plasma column, because the profiles are determined by sheath effects close to the radial boundaries. The radial position of the maximum density gradient is indicated by dotted lines in Fig. 5.11a-c. The potential profile in the central plasma region is fitted by a parabola. This can be justified by a simple MHD calculation which shows that a Gaussian density profile is self-consistent with a parabolic potential profile [117]. And indeed, in the restricted region, $r \leq 40$ mm, a parabola fits the profile quite well (solid line). Using the parabolic potential profile, $\Phi_p = ar^2 + c$, the $\mathbf{E} \times \mathbf{B}$ -velocity can be written as

$$\mathbf{v}_{E \times B} = -\frac{\nabla\phi \times \mathbf{B}}{B^2} = \frac{2ar}{B}\mathbf{e}_\theta. \quad (5.8)$$

with \mathbf{e}_θ being the azimuthal unit vector. It is found that the drift velocity is proportional to r . Thus, the associated $\mathbf{E} \times \mathbf{B}$ frequency $\omega_{E \times B}$ is independent of r . Consequently the $\mathbf{E} \times \mathbf{B}$ rotation of the plasma column is radially unshaped, i.e. the plasma can be regarded as a rotating solid body. This is an important fact to be kept in mind.

Plasma density

Of similar importance is the plasma density profile. A typical density profile for the KIWI device is shown in the contour plots in Figs. 5.13 and 5.12. The orientation of the cross sections as well as the discharge parameters are similar to those of the potential profiles. For simplicity an arbitrary scale is used for the density plots, because in contrast to potential the density lacks a discharge parameter like the grid voltage U_g for comparison.

Like the potential profile, the radial density profile is influenced by the fringing magnetic field lines. The radial density profile is broadest near the grid and narrows within 200 mm distance from the grid. Integrating $n(r, \theta, z)$ over r and θ shows that the plasma is injected at the grid and that the total number of charged particles $N(z)$ in a plane perpendicular to z decreases along the z -direction (Fig. 5.14). The convergence of the magnetic field lines leads to a plasma density maximum at $z = 100 - 200$ mm although the total number of charged particles is lower than that close to the grid. The density gradient for $z \geq 200$ mm is the result of axial and radial particle transport.

The radial density profile at three different axial positions is plotted in Figs. 5.13a-c. A least square fit to the experimental data suggests that the radial density distribution is well approximated by a Gaussian $n(r) \propto \exp(-r^2/2r_p^2)$. The diamagnetic drift velocity is then given by

$$\mathbf{v}^* = \frac{\nabla p_e \times \mathbf{B}}{enB^2} = \frac{k_B T_e}{eB} \frac{r}{r_p^2} \mathbf{e}_\theta. \quad (5.9)$$

With the experimentally justified assumption of a radially constant electron temperature, we find that the electron diamagnetic drift velocity is proportional to r only. The related drift frequency ω^* is independent of r , i.e. the drift is radially unsheared.

Another important information is obtained from Fig. 5.12. These plots use the coordinate \hat{r} rather than r , i.e. they are centered to the vacuum vessel and not to the plasma column. Therefore, the absolute position of the plasma column can simply be read from these plots. These absolute coordinates are essential for an improved concentric positioning of the probe array and the exciter. Fig. 5.15 depicts the result.

5.3.2 Plasma fluctuations

A special feature of the KIWI is that fluctuations are not observed for all discharge parameters. The most important parameter to control the occurrence of fluctuations and their dynamics is the grid bias U_g [34]. Depending on U_g , there are three distinct regimes. For low grid voltage (approx. 4 V), single drift modes are observed. For intermediate grid voltage (5-6 V) drift modes establish nonlinear saturation. For higher grid bias multi-mode states and even weakly developed turbulence are observed. The transition from stability to turbulence follows the Ruelle-Takens-Newhouse scenario [34].

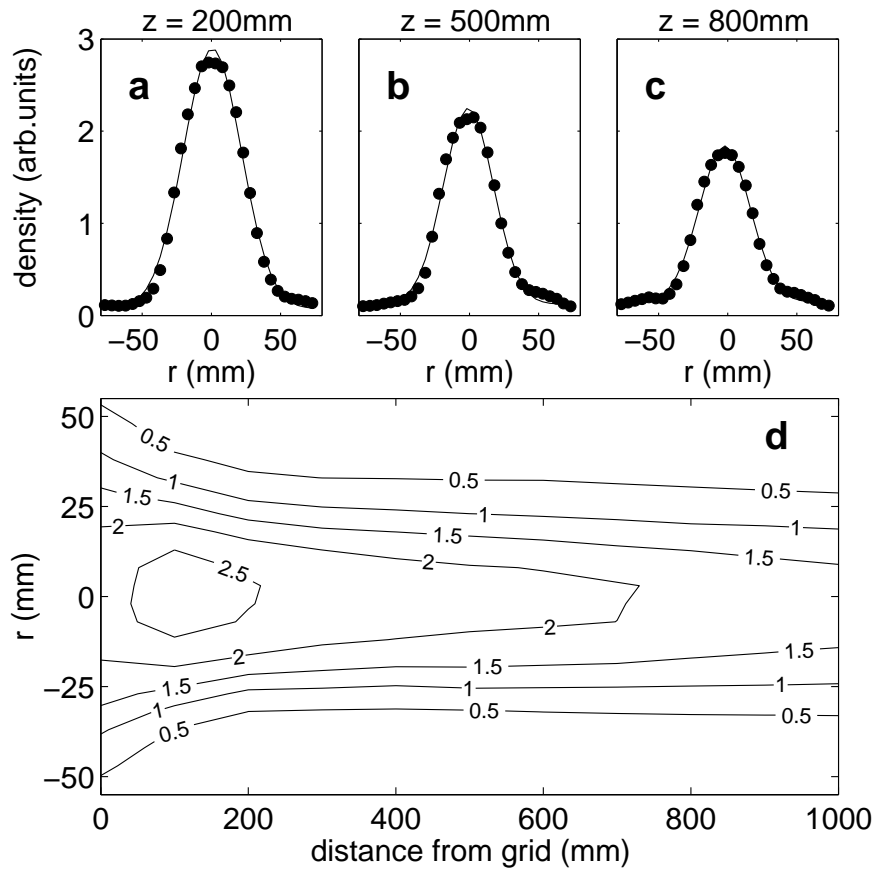


Figure 5.13: (a)-(c) show radial density profiles at different axial positions. The solid line is a least square fit of a Gaussian to the measurement. The density contour (d) shows a 2D section in the rz -plane through the center of the plasma column.

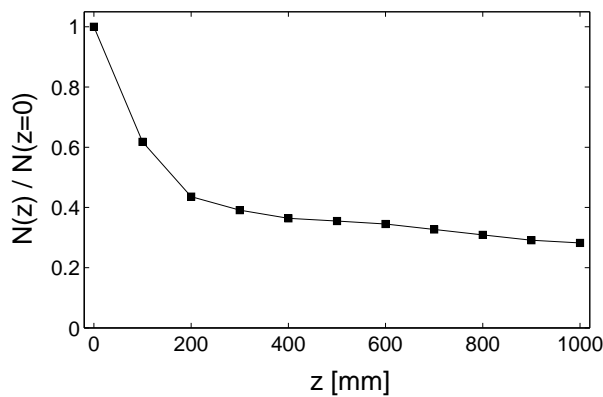


Figure 5.14: Integrated density perpendicular to B as a function of z .

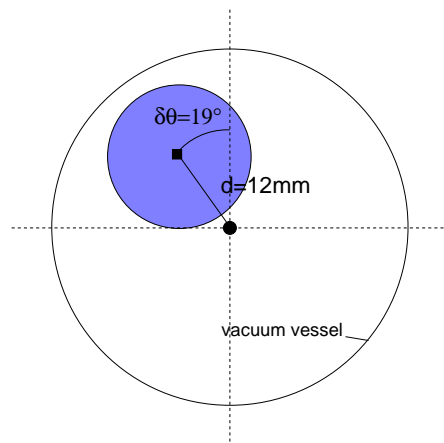


Figure 5.15: Absolute position of the plasma column with respect to the vacuum vessel.

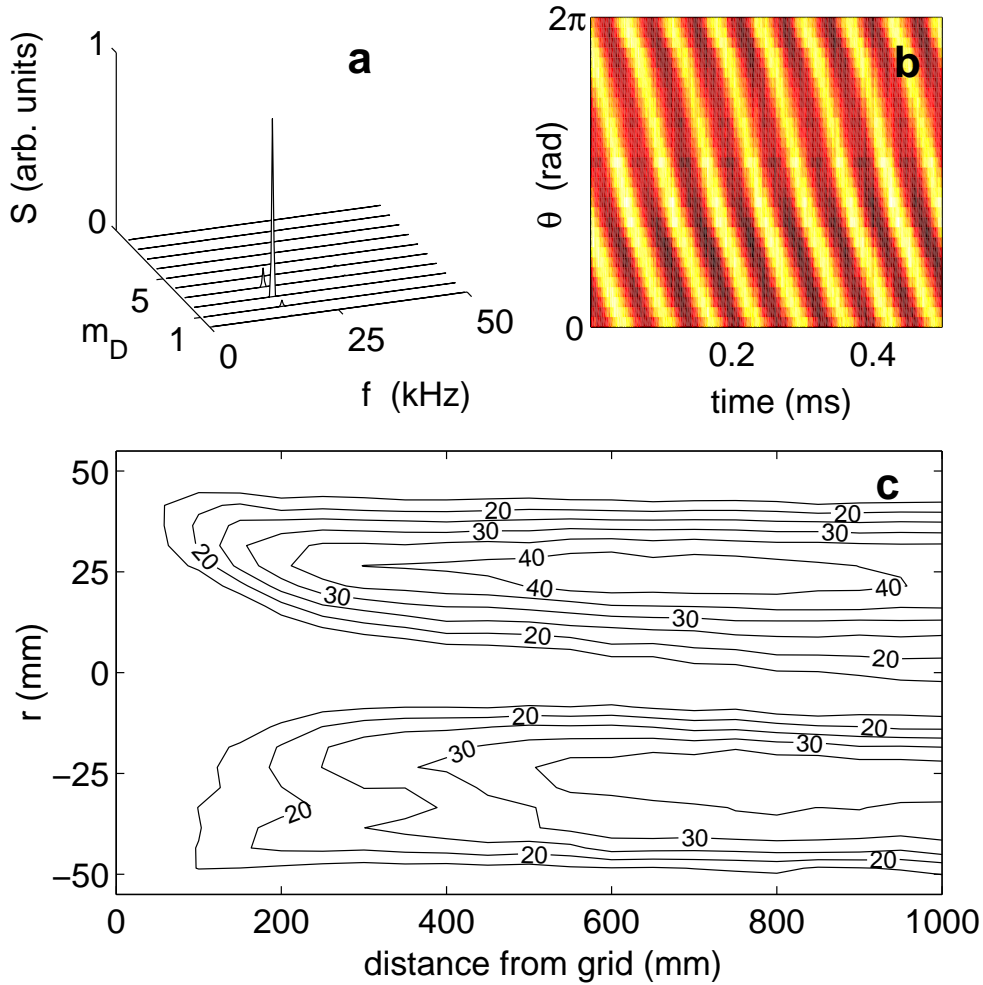


Figure 5.16: (a) frequency wave number spectrum of a $m = 2$ drift mode. It has been calculated from the density fluctuation data shown in the color plot (b). The density fluctuation profile (c) is normalized with the unperturbed density. The number attached to the contour lines are the density fluctuation amplitude in percent.

To identify the observed fluctuations as drift modes the following characteristics have to be met:

1. The fluctuation maximum has to be close to the position of maximum density gradient and the radial position of the fluctuation maximum should move outwards with increasing mode number (see Fig. 2.1).
2. The observed frequencies have to be in the range predicted by theory and the modes should be linearly unstable.
3. The main propagation direction of the wave has to be perpendicular to the magnetic field but the parallel wave number k_{\parallel} should not be zero.

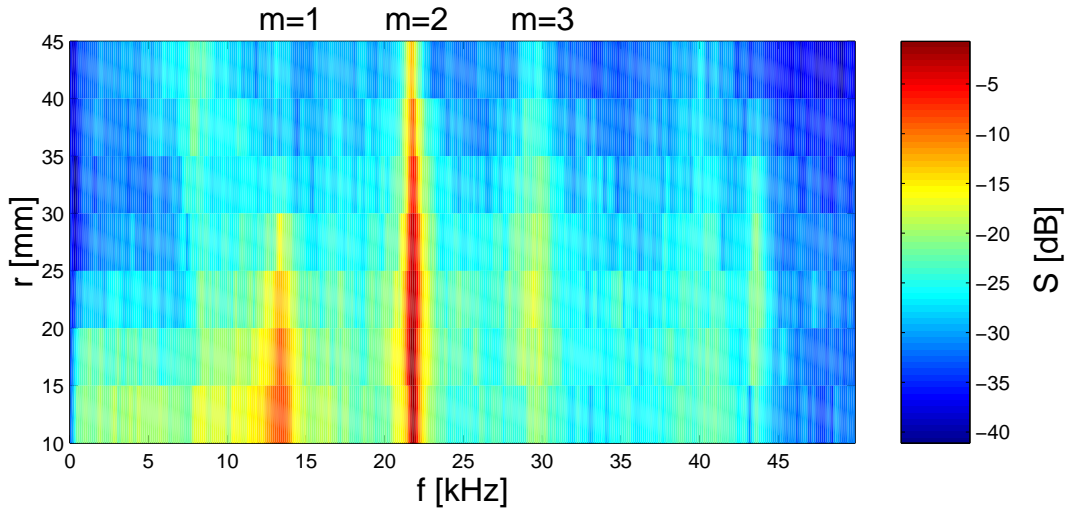


Figure 5.17: Color coded power spectra of density fluctuations as function of radial position.

Point 1: A close inspection of the density profiles already shows that the maximum density gradient is located at $r = 25$ mm. If this is compared with the position of maximum density fluctuation normalized to the background density (Fig. 5.16 c), a good agreement is found. To show the radial dependence on mode number Fig. 5.17 depicts color coded power spectra at different radial positions for a multi mode state. Clearly three distinct maxima are observed. The according mode numbers are printed above. The peaks are slightly shifting radially outwards with increasing frequency and mode number, i.e. the predicted radial dependency on mode number is clearly observed.

Point 2: In the framework of the GNM the density profiles can be used to calculate the observable frequencies for drift waves. A detailed comparison with the experimental data has been done by SCHRÖDER [117]. To summarize the obtained results: within the experimental accuracy the predicted and measured frequencies for $m_D = 2$ and $m_D = 3$ modes are in good agreement ($\Delta f/f < 5\%$). The observed drift wave propagation is determined by the $E \times B$ and diamagnetic drift velocity. An analysis of stability has been made earlier and has also been in good agreement with the experimental findings [115]. The measurements revealed that the axial drift and the $E \times B$ rotation are the main destabilizing effects.

Point 3: This is the most difficult part to show. The wave character perpendicular to B is easily verified by time series recorded with the 64 probe array (Fig. 5.16 b). The ion saturation current fluctuations show clearly a propagating $m = 2$ mode. This visual result is verified by a frequency mode number spectrum (Fig. 5.16 a), which is directly obtained from Fig. 5.16 b by a Fourier transform. To determine the parallel wave number turns out to be much more sophisticated. Analyzing the axial fluctuation profile suggests the picture of a standing wave between the grids. Because such a

wave involves approximately equal contributions of the forward and reflected wave, simple phase measurements can hardly determine the axial wave number. The large wave length obtained from earlier measurements [115] might be related to a slight difference in the absolute value of k_{\parallel} for forward and reflected wave. This difference can be introduced by axial inhomogeneities and sheaths [118].

5.4 Concluding remarks

To conclude, the measurements show that the observed fluctuations have to be classified as collisional, current-driven, rotation induced drift waves. For the presented experiments, their spatial and temporal structure is now quite well understood and has been related to the equilibrium profiles of the plasma. In particular, the $E \times B$ rotation of the plasma column and the diamagnetic electron drift are found to be unshered, i.e the azimuthal drift wave propagation is unshered. The observed fluctuations have been identified as drift waves and the observations are in good agreement with the linear, nonlocal GNM presented in chapter 2.

The presence of global monochromatic drift modes makes the KIWI ideally suitable for a systematic study of the influence of external driver signals on the drift wave dynamics. The possibility to perform similar experiments with a single and a multi mode state under similar conditions gives the unique opportunity to gain insight into the complex dynamics of the multi mode state.

Chapter 6

Synchronization of drift waves

By means of the van der Pol oscillator it has been shown in chapter 3 that oscillatory unstable systems exhibit new dynamics like complete and incomplete synchronization and quasi-periodicity if they are driven. Similar observations have been made for several oscillatory unstable and periodically driven plasma systems [56, 68, 72, 74]. For drift waves and drift wave turbulence only a few observations were made [51, 52, 81]. However, detailed investigations on the influence of spatio-temporal driver signals on drift waves have not yet been made. Due to the complex dynamics of the undriven turbulent system, the general problem arises how single mechanisms can be related to the observed changes, if such a system is driven externally. With respect to this the KIWI marks an exception. On the one hand, the dynamics of single, monochromatic drift modes is well understood. On the other hand, the possibility to establish different dynamical situations allows to investigate the interaction of drift wave and driver for a simple situation (*single-mode state*) first. In a second step, a more complicated situation, including several modes (*multi-mode state*), can be investigated.

6.1 Single-mode state

The simplest dynamic situation observed in KIWI is a single, monochromatic drift mode (*single-mode state*). This well understood system is used to attack the following questions:

- Does a spatio-temporal driver signal influence the drift wave dynamics and how can this be quantified?
- Are the observed phenomena related to the nonlinear dynamics of driven oscillatory systems, e.g. the van der Pol oscillator?
- Is the process purely temporal or does the spatial component of wave and driver play a significant role?

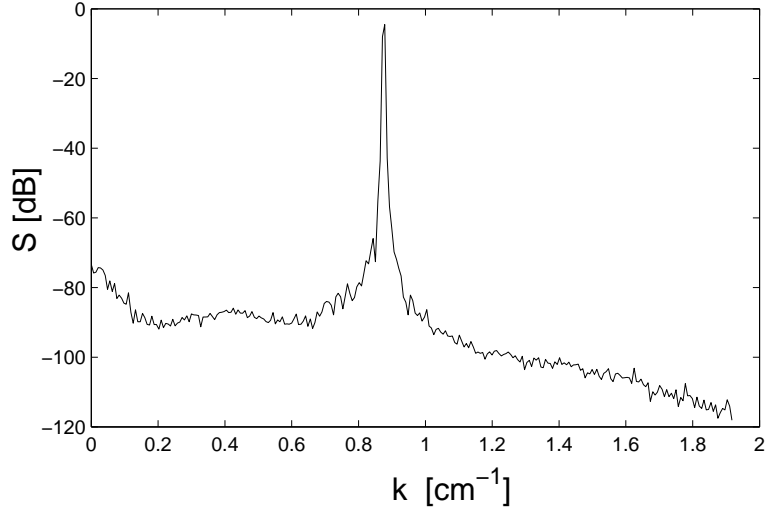


Figure 6.1: Local wave number spectrum $S(k)$ of a $m = 2$ drift mode at $r = 25$ mm.

6.1.1 Dynamics without exciter signal

Although the single-mode state has been already described in some detail in chapter 5, it is necessary to refine this description to obtain wave number values, which are needed for later reference. The plot in Fig. 6.1 shows the local wave number power spectrum recorded at $r \approx 23$ mm, i.e. close to the position of maximum density gradient. The only peak of the wave number spectrum is observed at $k_0 \approx 0.9 \text{ cm}^{-1}$. This corresponds well with a $m = 2$ drift mode. The related drift wave frequency is $f_0 \approx 18$ kHz.

6.1.2 Dynamics with exciter signal

Before investigating the influence of the exciter signal on the dynamics it is essential to drop a few notes on the exciter, its position and signals. A technical description including performance data has already been given in chapter 5, but the operation parameters have not yet been discussed. At first, it is essential to think about the radial position of the exciter plates. On the one hand, it is desired to couple the exciter signal efficiently into the plasma. This requires a good contact with the plasma. On the other hand, the exciter plates should not act as limiters and therefore artificially change the density gradient and the related fluctuations. As a compromise the exciter plates are positioned at $r = 45$ mm (Fig. 6.2). At this position the plates are well separated from the position of maximum density gradient and maximum fluctuation level. A significant influence on the density profile is not observed.

To simplify the interpretation of the dynamics of the driven system the exciter mode is chosen to be identical to the observed drift mode, i.e. $m_{ex} = 2$. The exciter frequency is varied around 18 kHz. Further, the propagation of the exciter signal is changed from non-rotating to co- and counter rotating. The exciter signal amplitude varies between

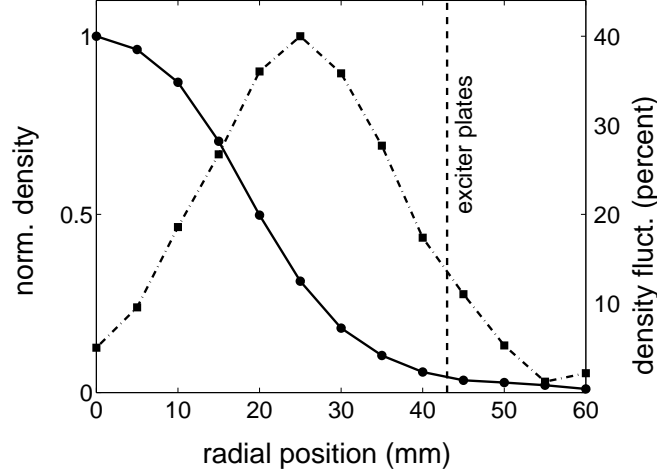


Figure 6.2: *Radial position of the exciter plates. For comparison the radial equilibrium density profile (solid line) and the relative density fluctuation profile (dashed-dotted line) are shown.*

3 and 8 V. The resulting power spectra $S(f)$ of the ion saturation current fluctuations of the driven system are shown in Fig. 6.3. The peaks of the $m = 2$ drift wave and the $m_{ex} = 2$ driver are marked in each sub-plot.

For **non-rotating** exciter signal only a weak peak for the driver occurs in the spectrum. This peak increases slightly (10 dB) when the exciter frequency approaches the drift wave frequency. For a region very close to the drift wave frequency only a single peak is observed for driver and drift wave. At this position the peak is slightly above the usual position of the drift wave peak. This indicates that the drift wave is synchronized by the driver. The only small frequency shift shows that the influence of the driver on the drift wave is not strong. For all other regions the position of the drift wave peak is not affected by the driver. Further, side band structures symmetric to the drift wave peak are observed. These side bands are related to the driver frequency by $f_{sb} = f_{dw} \pm n(f_{dw} - f_{ex})$ with n being an integer number. This is an indication for amplitude modulation, i.e. an interaction of drift wave and driver. The peak amplitude of these side bands as well as the number of side bands shows that this interaction is only weak.

For the case of **counter-rotating** exciter signal the observations are similar to those made for non-rotating exciter signal. The side band structures are little weaker but still symmetric. The extent of the regions, where synchronization is observed, are almost comparable.

A decisively different dynamical behavior is observed for **co-rotating** exciter signal. At first, a large region of synchronization symmetric to the drift wave frequency of the unperturbed system is observed. Further, strong side bands are seen for almost any exciter frequency outside the synchronization region. The amplitude of these side bands and of the driver peak itself increases the more driver and drift wave frequency

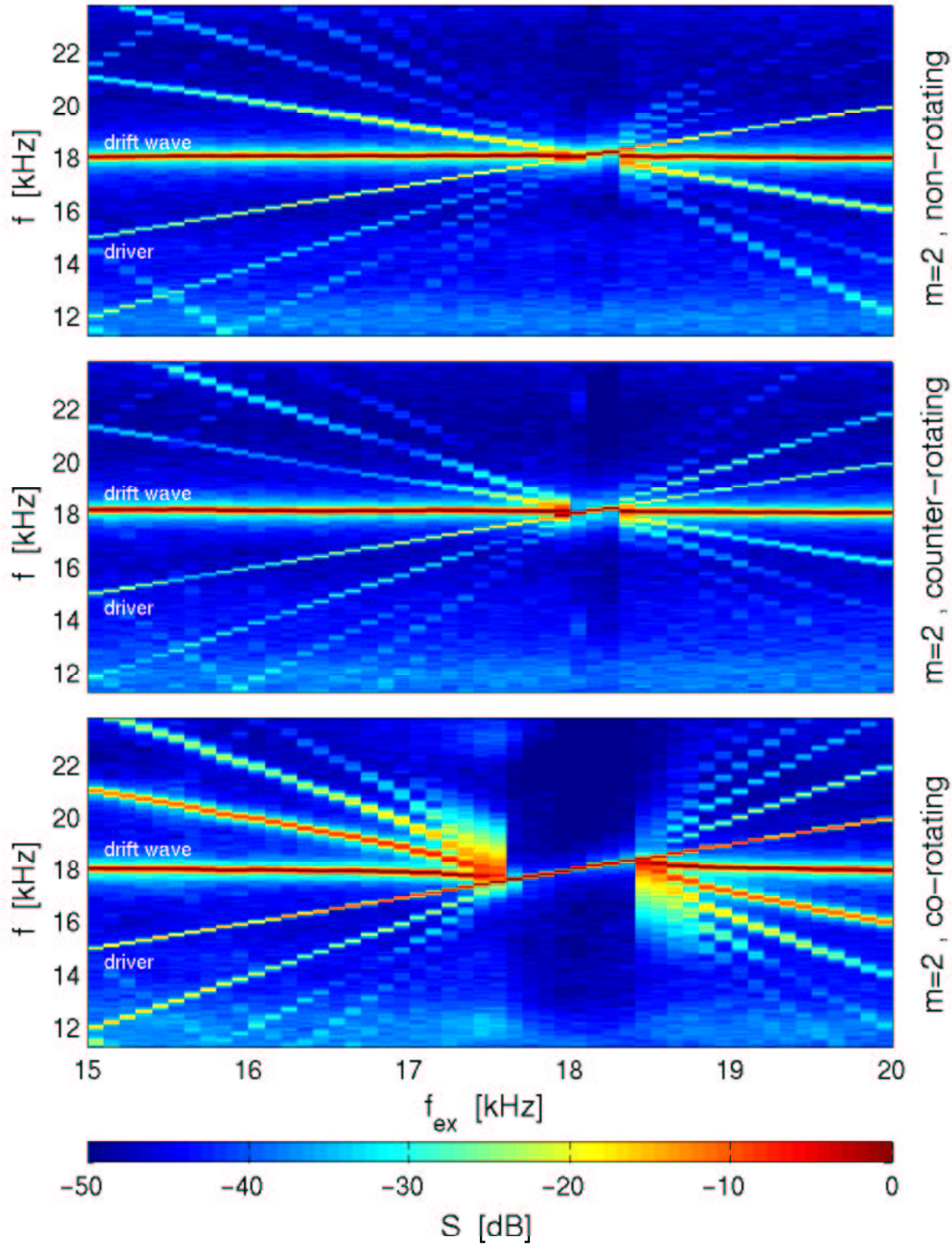


Figure 6.3: Spectral power density $S(f)$ of ion saturation current fluctuations as function of exciter frequency f_{ex} . The peaks from the $m = 2$ drift mode and the $m_{ex} = 2$ driver signal are marked. The exciter amplitude is 8 V.

approach each other. The amplitudes of drift wave and driver near the synchronization region are almost comparable. Additionally, the position of the drift wave peak is influenced by the driver even outside the synchronization region. Near synchronization the drift wave peak moves towards the driver peak. At the same time the side band structure becomes asymmetric. The asymmetry is less pronounced with increasing distance from the synchronization region.

To summarize the above listed results, it is found that the exciter has a significant influence on the dynamics of the system. The propagation direction determines how strong the interaction of driver and drift wave is. For matching propagation direction the interaction is strongest and the spectral characteristics of the density fluctuations differ substantially. The asymmetry of side bands and the nonlinear dependency of the beat frequency $f_{beat} = f_{dw} - f_{ex}$ are indications for incomplete synchronization, i.e. periodic pulling.

6.1.3 Synchronization

Common to all situations in Fig. 6.3 is a region of synchronization. Its width is obviously linked with the coupling strength of driver and drift wave. The proportionality between driver amplitude/strength and width of the synchronization interval has already been shown for the driven van der Pol oscillator (chapter 3). These findings motivate to use the width of the synchronization interval to investigate the importance of the spatial component of the driver signal for the synchronization process.

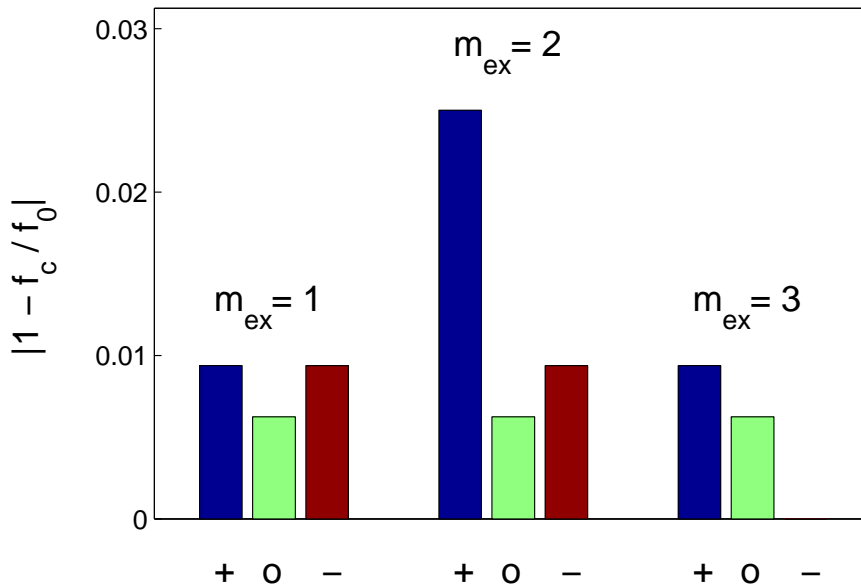


Figure 6.4: Dependence of the synchronization threshold f_c on spatial exciter signal structure and propagation direction. '+' denotes co-rotating, '-' counter-rotating and 'o' non-rotating exciter signals. The exciter amplitude is 8 V.

Dependence on driver signal structure

Fig. 6.4 summarizes the results of a number of measurements similar to those presented in Fig. 6.3. f_c denotes the lower exciter frequency threshold for synchronization. The same results are obtained for the upper exciter frequency threshold. The normalization to the undriven drift wave frequency corrects for slight plasma parameter drifts. Fig. 6.4 shows the synchronization width for all possible exciter signal structures. '+' denotes co-rotating, '-' counter-rotating and 'o' non-rotating exciter signals. Clearly the synchronization for a $m = 2$ drift mode is most efficient if the exciter signal has a matching mode number and propagation direction. This emphasizes the spatio-temporal character of this drift wave synchronization, i.e. the spatial component plays an essential role.

The origin of approximately the same synchronization width for non matching exciter signals can be explained by pure temporal synchronization effects, because similar behavior is observed for only one active exciter plate. The measurements prove that the known temporal synchronization [51, 52] is significantly enhanced by the spatial component. The dependency on the propagation direction stresses that the enhancement is not the result of the larger number of electrodes.

Dependence on exciter amplitude

Independent of the spatial structure of the driver signal, the driver amplitude will certainly have an influence on the synchronization width. For the driven van der Pol system the dependence of synchronization width on driver amplitude is described by Arnol'd tongues, i.e. the synchronization width increases with driver amplitude. Fig. 6.5 shows the synchronization region as function of the exciter amplitude. The exciter frequency is again normalized to the drift wave frequency of the undriven system f_0 . The solid line marks the threshold for synchronization. With increasing driver amplitude the synchronization width increases. The functional dependency for this system is well described by a parabola. Although the van der Pol model predicts a linear dependence of f_c on driver amplitude, this deviation is not surprising. The sheath between plasma and exciter plate will determine the coupling of the exciter signal into the plasma. The shielding of external potential by the plasma is likely to attenuate the exciter signal, i.e. exciter amplitude and driver amplitude are not the same.

Besides synchronization, periodic pulling is observed for the driven van der Pol system. A characteristic of this process is the nonlinear dependence of the beat frequency on the driver frequency (Eq. 3.16). For the driven drift wave such a nonlinear dependence is observed for a co-rotating driver signal with matching spatial mode structure as well (Fig. 6.3). This nonlinearity can be used for a further analysis of the influence of the driver signal amplitude on the dynamics of the driven system. The dashed line in Fig. 6.5 is determined by the criterion

$$f_{beat} - (f_{dw} - f_0) > 100 \text{ Hz.} \quad (6.1)$$

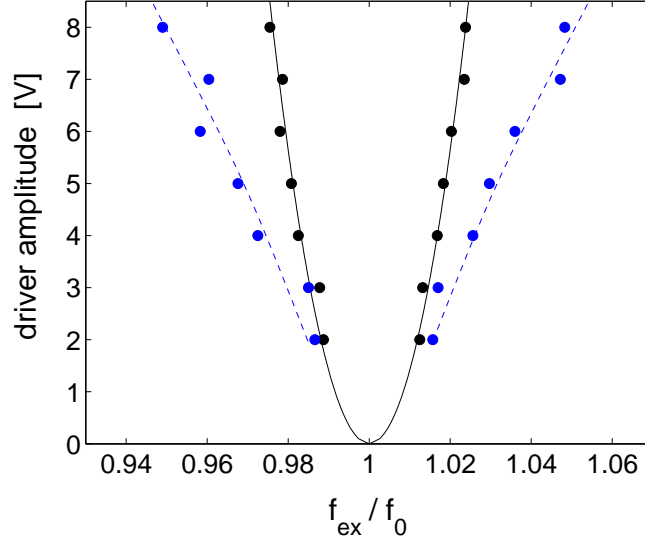


Figure 6.5: Synchronization region as function of the exciter amplitude. The exciter frequency is normalized to the drift wave frequency of the undriven system f_0 . The solid line marks the threshold for synchronization. The dashed line is determined by Eq. 3.16.

The left hand side describes the deviation of the observed beat frequency from the linear beat frequency, expected for modulation or simple signal superposition. In other words, Eq. 6.1 sets a threshold, above which periodic pulling is assumed to be significant. The similarity with the periodic pulling regime observed for the driven van der Pol system is evident. With increasing driver amplitude the region, where a significant nonlinearity is observed, increases. This is another strong indication, that the influence of the driver signal on drift wave dynamics increases with driver amplitude.

6.1.4 Periodic pulling

The observed nonlinearity of the beat frequency and the asymmetry of the side band structure close to the region of synchronization, already show that the driven drift wave experiences periodic pulling. To see to what extent this phenomenon is related to the periodic pulling of the van der Pol system, a quantitative comparison of both systems is necessary.

Temporal analysis

At first, it is meaningful to compare the temporal characteristics. Because of the definition of periodic pulling as amplitude and phase modulation, Fig. 6.6 a and b show amplitude of the ion saturation current fluctuations and its phase with respect to the driver as function of time for an exciter frequency close to the synchronization threshold. The phase modulation is clearly observed. The two characteristic time scales

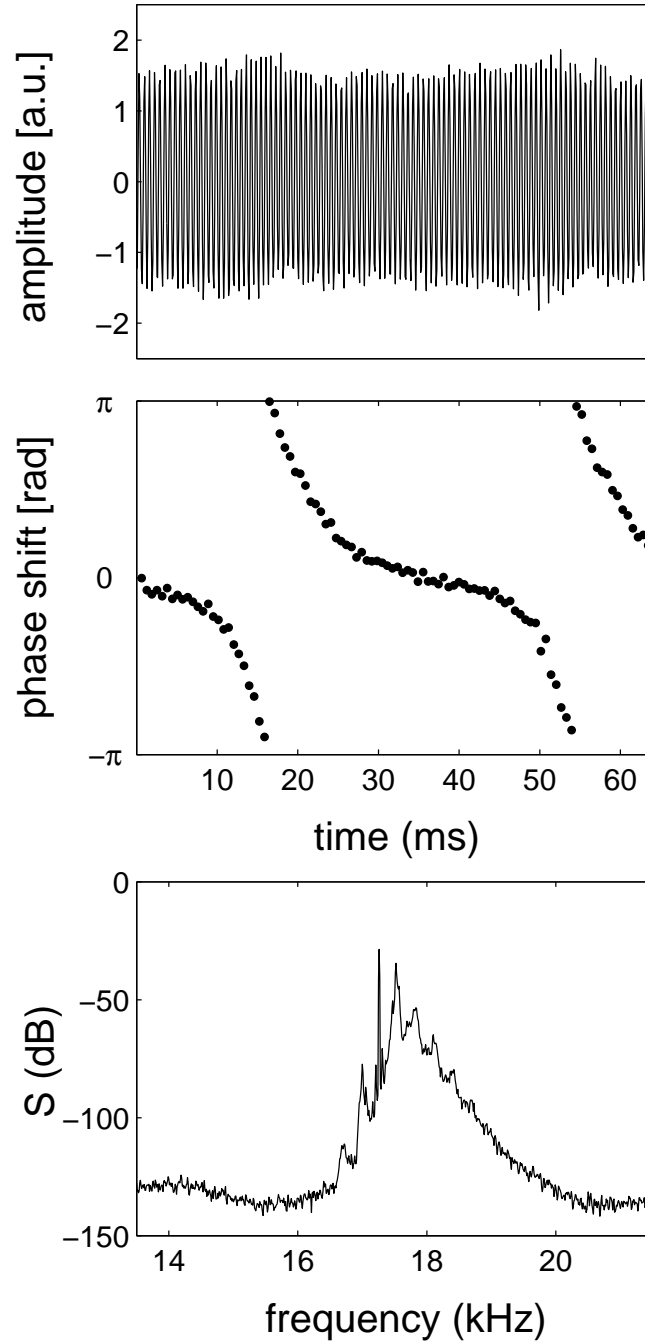


Figure 6.6: Time series of (a) ion saturation current fluctuation and (b) phase with respect to the exciter signal. Both, drift mode and exciter signal are $m = 2$ modes. The exciter signal is co-rotating and has an amplitude of 3 V. (c) shows the power spectrum calculated from (a).

of periodic pulling are well established. The slow phase evolution is related to no phase shift of exciter signal and drift wave. The amplitude modulation is weak. The slight enhancement in amplitude in Fig. 6.6 a corresponds to the fast phase evolution observed in Fig. 6.6 b. The combination of amplitude and phase modulation is evident from the power spectrum (Fig. 6.6 c), which is calculated from the time series depicted in Fig. 6.6 a. The spectrum has the typical triangular shape known for periodic pulling (chapter 3).

To test whether the driven drift wave system shows van der Pol like behavior, Eq. 3.16 can be used. Fig. 6.7 depicts the dependence of the beat frequency f_{beat} on f_{ex} . The different dynamics are indicated by typical power spectra. The dashed line marks the linear beat frequency. The solid line is a least square fit of

$$f_{beat} = (f_0 - f_{ex}) \sqrt{1 - \frac{f_c^2}{|f_0 - f_{ex}|^2}}. \quad (6.2)$$

to the data. This is equivalent to Eq. 3.16, only the notation has been adapted. The free parameter for the fit is f_c . The good approximation of the data by the fit shows that the system behaves van der Pol-like.

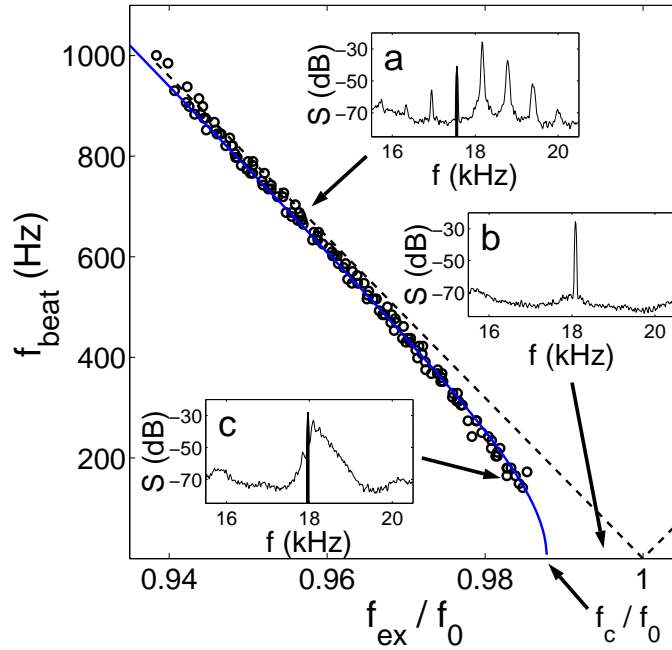


Figure 6.7: Frequency dependence for a co-rotating exciter signal. The dashed line denotes the linear beat frequency $|f_{ex} - f_0|$. f_c/f_0 marks the threshold above which synchronization takes place. (a) Modulation. Power spectrum for f_{ex} being smaller than f_c . (b) Complete synchronization. Power spectrum for f_{ex} larger than f_c . (c) Incomplete synchronization. Power spectrum for $f_{ex} \approx f_c$. The driver frequency peak is marked black.

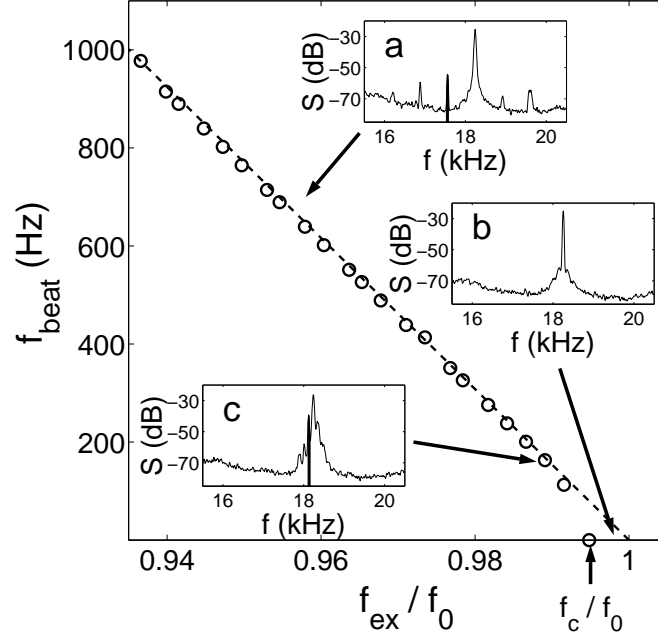


Figure 6.8: *Frequency dependence for counter-rotating exciter signal. The notations are similar to those in Fig. 6.7.(a) Modulation. Power spectrum for f_{ex} being smaller than f_c . (b) Complete synchronization. Power spectrum for f_{ex} larger than f_c . (c) Modulation. Power spectrum for $f_{ex} \approx f_c$. The driver frequency peak is marked black.*

For counter-rotating exciter signal a nonlinearity of f_{beat} is not observed (Fig. 6.8). Due to the limitations of the digital frequency synthesis of the exciter signal it is not possible to investigate the dynamics for exciter frequencies very close to f_c . Therefore, a very small region of periodic pulling can not be excluded, but compared to prior observations of periodic pulling of drift waves with purely temporal driver signals [51, 52] the counter-rotating signal seems to inhibit periodic pulling.

Spatio-temporal analysis

In the previous paragraphs was shown that the van der Pol model is capable to describe the temporal dynamics of the driven drift wave system. However, drift waves are a spatio-temporal phenomenon and the driving mechanism was found to depend strongly on the spatio-temporal character of exciter signal and drift wave. This rises the question how the periodic pulling process establishes spatially.

To investigate the spatio-temporal dynamics of periodic pulling, a subset of 15 probes from the 64 probe array is taken. These probes are equi-distantly distributed over half the circumference of the plasma column. This assures that the simultaneous recordings of the ion saturation current fluctuation cover a full wave length of a $m = 2$ mode. The 16th channel of the digitizer is used to record the exciter signal. Using the exciter signal as phase reference, the ion saturation current time series can be split into

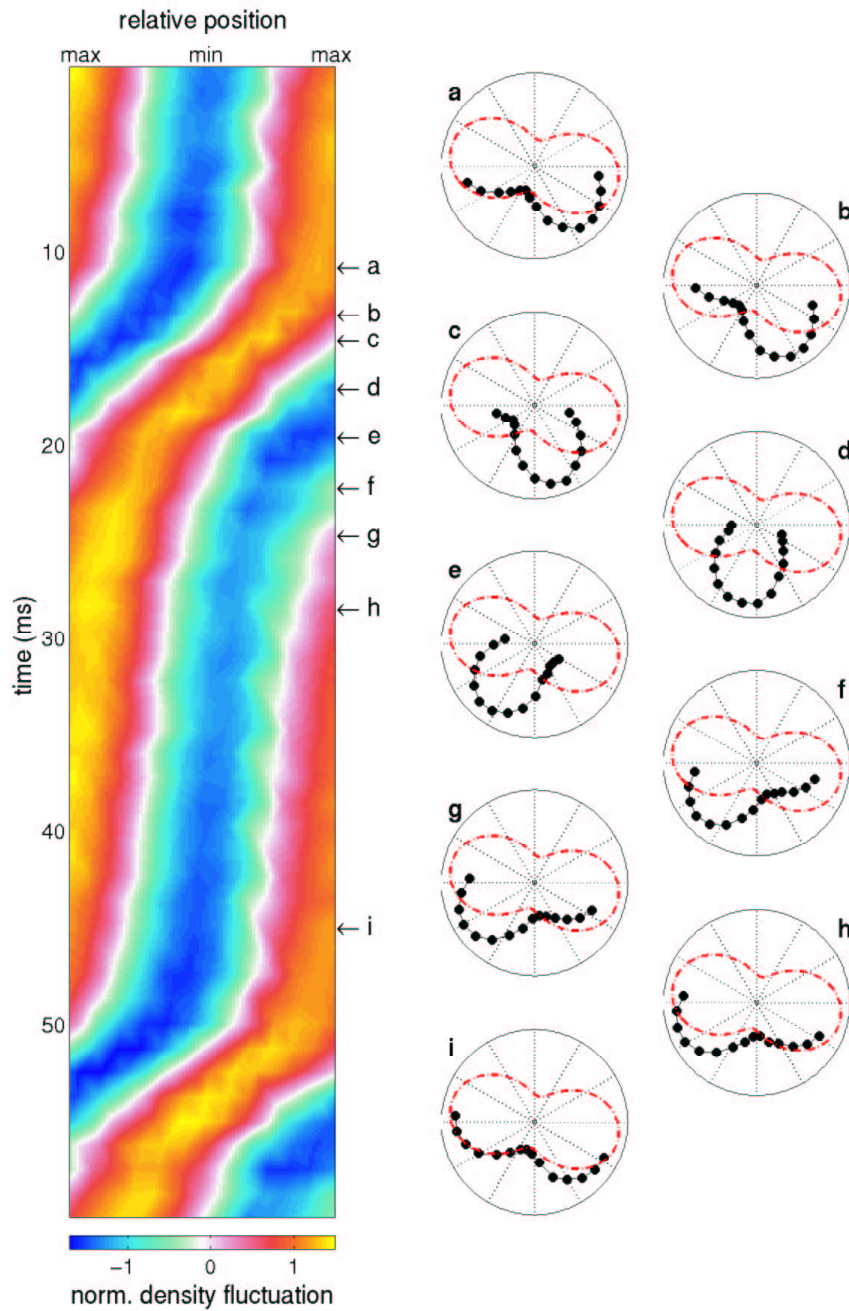


Figure 6.9: Visualization of spatio-temporal periodic pulling. The color plot shows the time evolution of the $m = 2$ drift mode phase with respect to the exciter signal. Typical for the process of periodic pulling are the two time scales. The polar plots (a) - (i) depict the relative motion of the drift mode (filled circles). The exciter signal is indicated by the dashed-dotted line. The maximum exciter signal belongs to positive exciter plate potential, while minimum exciter signal stands for negative potential. The drift mode maximum/maximum is related to positive/negative density fluctuations.

subsets of time series for certain phase angles of the exciter signal. Physically, this procedure describes a change of reference frame, in this case from the laboratory to a frame, which co-rotates with the exciter signal. The benefit is a separation of time scales. In the laboratory frame the slow periodic pulling is covered by the fast periodicity of the drift wave itself. A change to the co-rotating frame removes this fast time scale and the slower processes are observable. The resulting sub-time series are shown as color plot in Fig. 6.9. The labels 'min' and 'max' denote the related amplitude of the exciter signal. The poloidal plots (Fig. 6.9 a-i) help to determine the absolute phase shift of exciter signal (dashed-dotted) and drift wave (solid). Similar to the temporal analysis, the two time scales related to the pulling process are observed. The slow time scale (Fig. 6.9 g-i) is related to nearly zero phase shift of density fluctuation and exciter signal. The phase velocity of drift wave and exciter signal are almost identical. The drift wave propagates only little faster than the exciter signal, but for a certain mismatch of relative phase of drift wave and exciter the drift wave is accelerated. During a short period it propagates much faster than the exciter signal. The fast movement of the density fluctuation maximum corresponds to the region of exciter signal minimum, e.g. negative exciter signal. (Fig. 6.9 a-g). To summarize, the phase modulation observed in the temporal signal is produced by a temporal modulation of propagation velocity.

Up to now, only the temporal evolution in space has been studied, but what is about the spatial component of the wave itself? Is only the propagation velocity of the wave changed or does the shape of the wave change itself? To look for such behavior the propagation velocity variation has to be subtracted from the data, in other words, to change from the co-rotating exciter frame to the co-rotating drift wave frame. To achieve this, a trigger condition for the drift wave signal is needed to synchronize the azimuthal components. The most sensitive condition is the zero crossing of the signal. It allows for the least spatial detection error. Fig. 6.10 shows the drift wave in its co-rotating frame. The time scale is almost the same as in Fig. 6.9. It has been slightly prolonged to show the second pulling event completely. The azimuthal scale is now given in absolute values to allow for a wave length estimation. The color map is identical to those used in Fig. 6.9. Due to the probe arrangement the plotted region covers exactly half the azimuthal circumference, i.e. for a $m = 2$ drift mode one wave length. Two remarkable features are observed in Fig. 6.10:

First, the spatial extension of minimum and maximum is modulated in time. The modulation amplitude is about $\Delta\theta \approx 1$ cm. With a spatial separation of $\Delta x = 0.44$ cm of two neighboring probes, the observed modulation corresponds to a shift by two probes. This excludes the possibility of spatial under-sampling and demonstrates that the observed modulation is not artificial. The wave length¹ of the whole drift wave $\lambda \approx 7$ cm corresponds to a wave number $k \approx 0.9 \text{ cm}^{-1}$. This is identical with the wave

¹Please note, that for this problem the terms *phase* and *wave length/number* do not match the usual definitions. Rather they have to be regarded as local wave properties, e.g. they describe how a wave would look like if these local properties would be extended to at least one spatial or temporal period. Therefore k_{min} (k_{max}) denotes the approximate wave number of the minimum (maximum).

number observed for the undriven drift wave. For the phase-locked period the spatial extent of the drift wave maximum is significantly stretched. This local wave length enhancement corresponds to a local wave number reduction of $\Delta k_{min} \approx -0.1 \text{ cm}^{-1}$. At the same time the drift wave maximum is compressed by the same distance. Therefore, the local wave number is enhanced by $\Delta k_{max} \approx 0.15 \text{ cm}^{-1}$. Additionally, the position of maximum/minimum amplitude changes with respect to the positions of zero density fluctuations, i.e. the drift wave is not only stretched/compressed but bend as well.

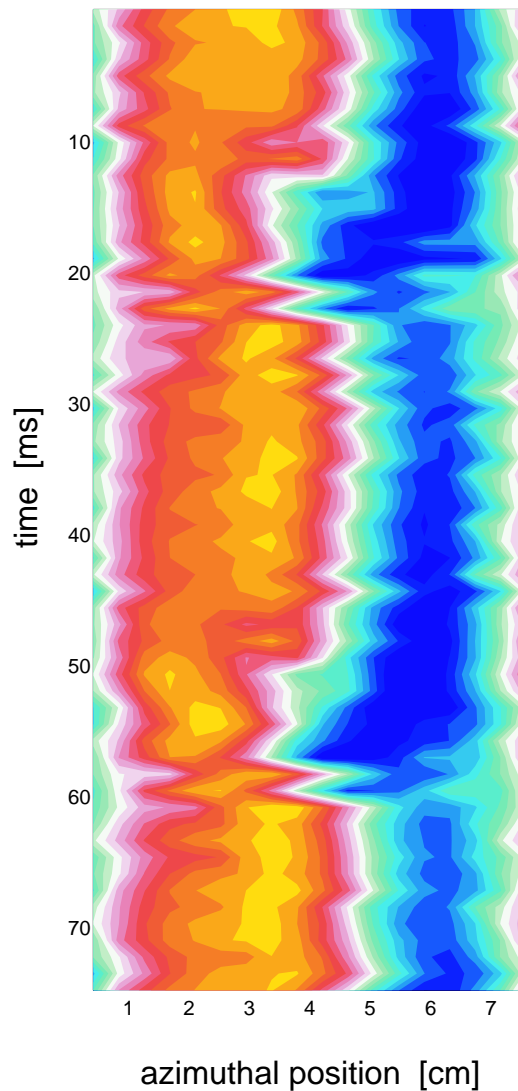


Figure 6.10: Visualization of spatial component of periodic pulling. The color plot shows the time evolution of the $m = 2$ drift mode phase in the co-rotating drift wave frame. The color code is the same as in Fig. 6.9. The azimuthal axis covers half the circumference of the plasma column.

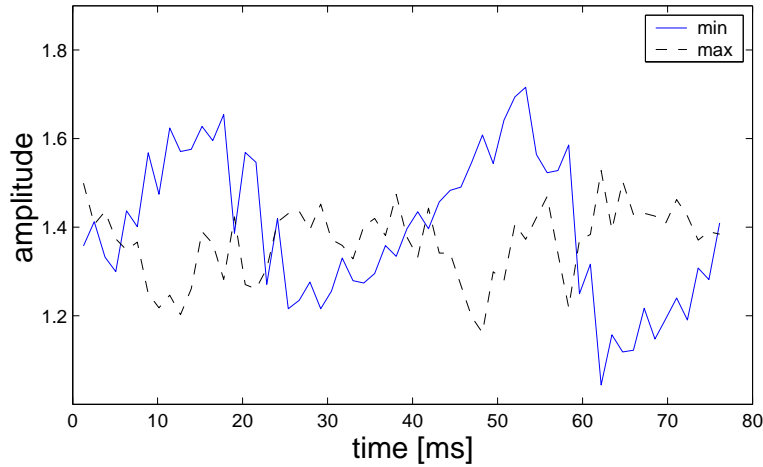


Figure 6.11: *Absolute amplitudes of minimum and maximum density fluctuations obtained from Fig. 6.10.*

The second remarkable finding from Fig. 6.10 is that the amplitude modulation for minimum and maximum density fluctuation are not similar. Fig. 6.11 shows this in more detail. For the minimum a clear amplitude modulation is observed. The amplitude is minimal at the beginning of the locking process and increases constantly during the process of locking until the drift wave unlocks. During the period of fast wave propagation the amplitude drops drastically. For the maximum such a clear modulation of amplitude is not observed. Interestingly the amplitude of the minimum is rather in opposite phase than in-phase with the temporal evolution of the maximum amplitude. This is in agreement with the observed local wave length modulation. The compression of the wave leads to an increase in amplitude. In order to fulfill the periodic azimuthal boundary conditions the other half wave is stretched, i.e. its amplitude reduces. The amplitude modulation of the minimum and maximum have opposite phase.

A different method to obtain information on the wave length modulation is a spectral approach with local frequency wave number spectra and local integrated wave number spectra. The spectra shown in Fig. 6.12 are calculated from the original time series recorded by two neighboring probes from the array. As reference the integrated wave number spectrum for the undriven state has been added. The driver frequency is slightly below 18 kHz. In the frequency domain of the local frequency wave number spectrum the typical asymmetry for the pulling process is observed. Only for frequencies higher than the driver frequency side bands of significant amplitude exist. In k such a clear asymmetry is not evident. The shift of the peaks to higher k with increasing frequency is not observed for all probe combinations. Hence, it seems to be not significant. On the other hand, the spectral broadening is always observed in the integrated wave number spectrum. This shows that the spectral method is less sensitive than the spatially higher resolved method described before and has to be interpreted with care. Nevertheless, both methods give clear indication that the observed periodic pulling of drift waves has a spatial component.

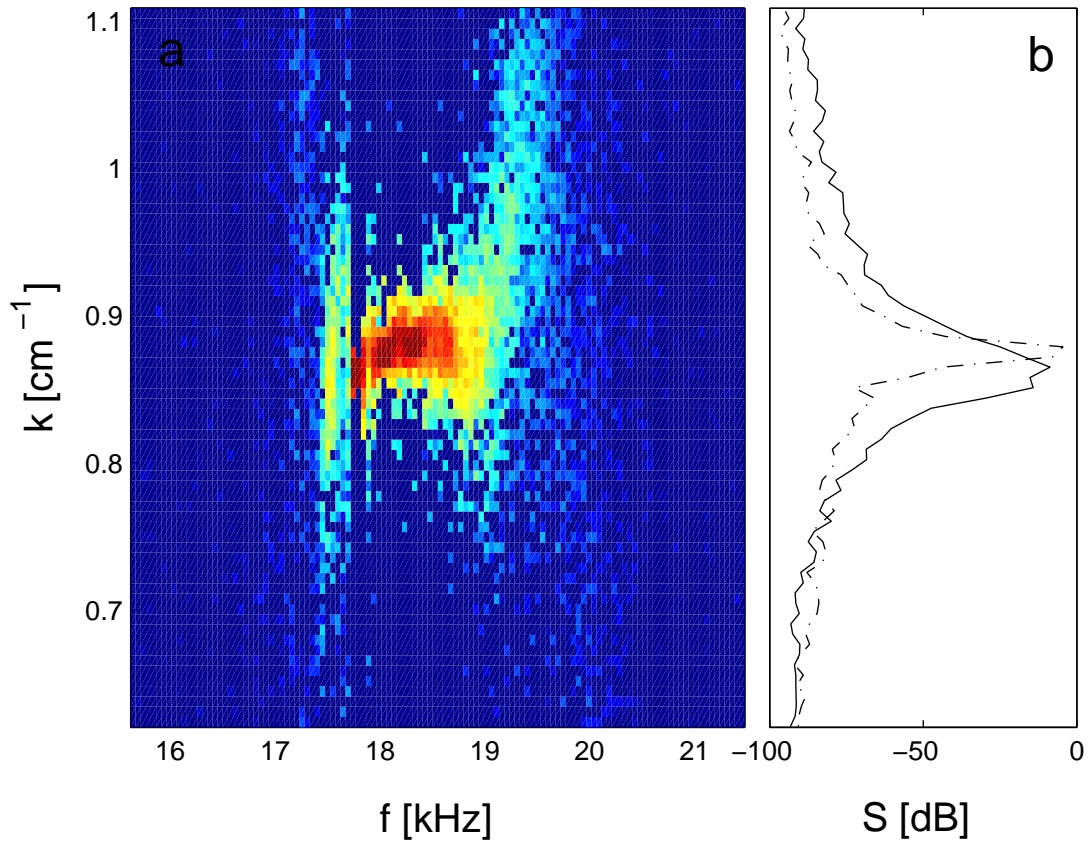


Figure 6.12: (a) The color plot shows the local frequency wave number spectrum for a driven $m = 2$ drift mode. The driver frequency is slightly lower than the drift wave frequency. It is calculated from density fluctuations recorded with the probe array. The radial probe position is $r = 23 \pm 2$ mm. Plot (b) shows the integrated wave number spectrum for the same data set (solid line) and the undriven system (dashed-dotted line).

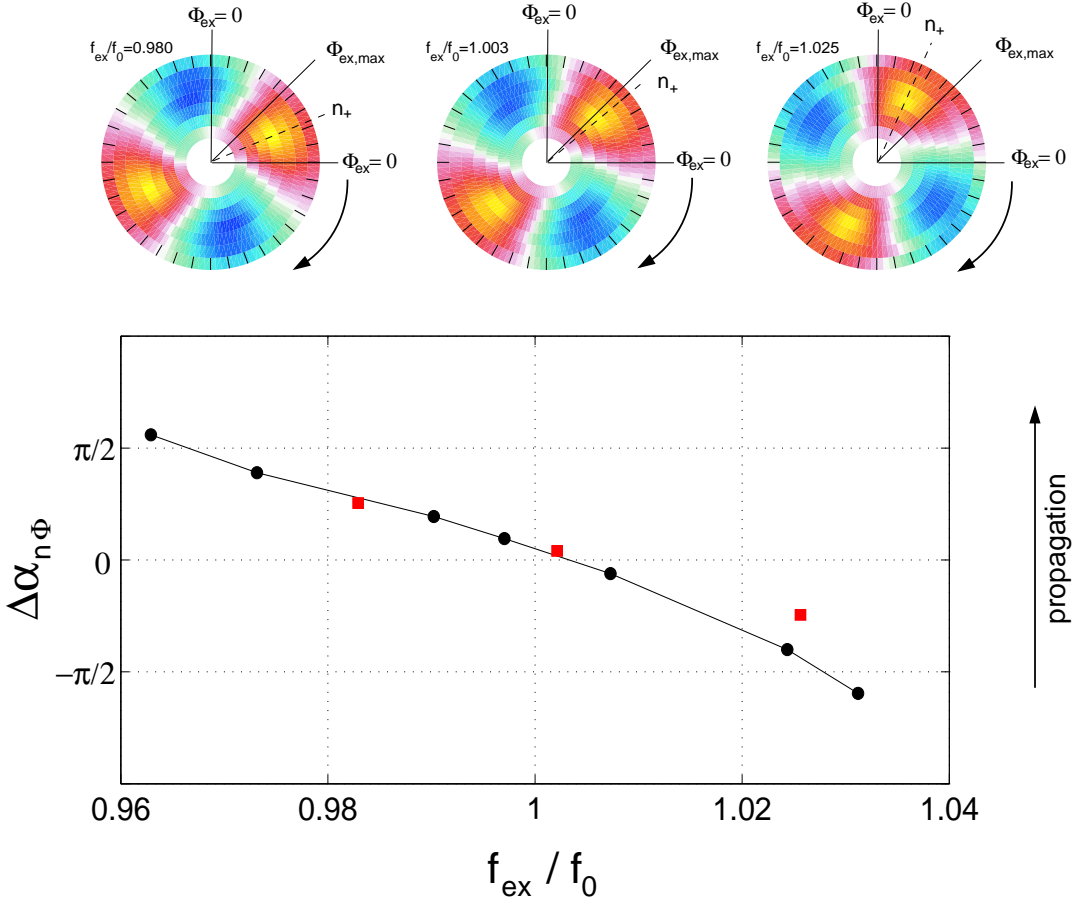


Figure 6.13: Relative phase measurements of density n and exciter signal Φ_{ex} . The color plots are obtained by phase sensitive data averaging method and show the spatial distribution of the coherent density fluctuations. The propagation direction of exciter signal and drift wave is indicated by arrows. The positions of density maximum n_+ and maximum exciter potential $\Phi_{ex,max}$ are marked. The phase shift between density and exciter potential maximum, obtained from these plots, are added to the plot below (squares). The other values are obtained from phase spectrum calculations. The phase shift is counted positive if the density maximum precedes the exciter potential maximum and negative if the density maximum lags behind the exciter potential maximum. The phase values are related to the exciter signal, i.e. a full azimuthal circumference is 4π .

Phase shift of drift wave and exciter signal

The spatio-temporal investigation of periodic pulling already revealed that the favored phase shift of the drift wave and the exciter signal is zero for matching frequencies. The question, whether the phase shift deviates from zero for $f_{ex} \neq f_0$, is answered with help of Fig. 6.13. It shows relative phase measurement of density n and exciter signal Φ_{ex} . The color plots are obtained by phase sensitive data averaging method and show the spatial distribution of the coherent density fluctuations. The propagation direction of exciter signal and drift wave is indicated by arrows. The positions of maximum density fluctuation n_+ and maximum exciter signal are marked. The exciter plates are located in the region covered by the ticks. The left color plot shows that n_+ is displaced in direction of propagation for $f_{ex} < f_0$. This corresponds to a positive phase shift of n and Φ_{ex} , i.e. n_+ precedes the exciter signal maximum. The approximate phase shift in degree can be obtained from the ticks at the border of the plot. Due to the tick separation of 10° the phase shift is approximately 20° . For $f_{ex} \approx f_0$, the phase shift is zero. For $f_{ex} > f_0$, the density lags behind $\Phi_{ex,max}$. A negative phase shift is found. These phase shifts are marked by squares in the lower plot. For comparison the results obtained from phase spectrum calculations are plotted as well. The results of both measurement techniques are in good agreement. The position of n_+ is shifted in direction of propagation for $f_{ex} < f_0$ and against direction of propagation for $f_{ex} > f_0$. The dependence of the phase shift on frequency mismatch is almost linear.

Taking into account that the observed drift wave frequency f_0 and applied exciter frequencies f_{ex} are directly related to the azimuthal propagation velocities of the un-driven drift wave \mathbf{v}_0 and exciter \mathbf{v}_{ex} (chapter 2 and 5) allows to extend the interpretation of the observed phase shifts. In the framework of propagation velocities, Fig. 6.13 shows that for $\mathbf{v}_0 > \mathbf{v}_{ex}$ the positive density perturbation n_+ advances the exciter signal maximum, but due to synchronization the propagation velocity of the driven drift wave is \mathbf{v}_{ex} , i.e. the drift wave is decelerated by the exciter signal. For $\mathbf{v}_0 < \mathbf{v}_{ex}$ the positive density perturbation n_+ lags behind the exciter signal maximum. Nevertheless, the synchronization assures that the propagation velocity of the driven drift wave propagated with \mathbf{v}_{ex} , i.e. it is accelerated. In other words, the phase shift of drift wave and exciter signal indicates whether the drift wave is accelerated or decelerated by the exciter signal. The fact that slower drift waves are accelerated but still lag behind the favored position of zero phase shift, while faster drift waves are decelerated but still precede the favored position, indicates that the position of zero phase shift has an apparently attractive character.

This attractive character is surprising at first, because the positively charged drift wave maximum seems to be attracted by a positive potential. A simple energy argument would lead to the conclusion that the position of zero phase shift is repulsive and not attractive. However, a closer look at the drift wave mechanism shows that this position can very well have an attractive character. For this purpose it is helpful to briefly review the propagation mechanism of drift waves (Fig. 6.14 a). The positive and negative charges of the drift wave maximum and minimum generate electric fields

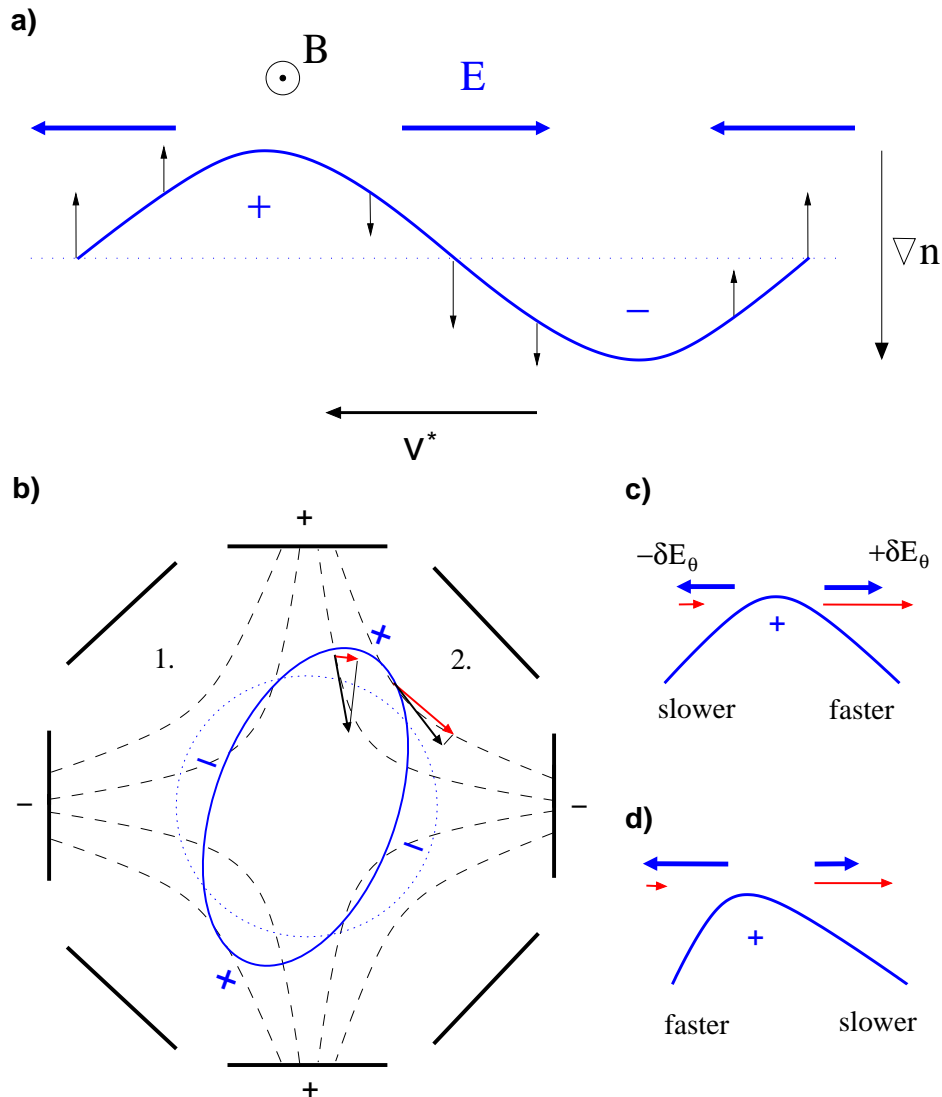


Figure 6.14: (a) Physical picture of the drift wave mechanism. The solid (dotted) line indicates a (un)perturbed density contour. Due to the Boltzmann relation the potential perturbation is in-phase with the density perturbations. The related electric fields (bold arrows) and the magnetic field B cause local $E \times B$ drifts (thin arrows). The resulting propagation of the perturbation is indicated by \mathbf{v}^* . (b) Sketch of the eight exciter plates (bold) and the topology of the vacuum electric field (dashed) for a $m_{ex} = 2$ mode. The plate potentials are indicated by '+' and '-'. Additionally, the electric field (black) and its azimuthal component (red) are plotted at two positions. The solid (dotted) line shows the equi-density color of a $m = 2$ drift mode (the unperturbed density profile). (c) and (d) are zooms of the region of maximum density perturbation for subsequent time steps. The bold (thin) arrows indicate the azimuthal electric field component of the drift wave (exciter field). The change of electric field strength due to superposition of these fields is marked by $\pm\delta E_\theta$. The related change in propagation velocity is labeled below.

(bold arrows). These fields in conjunction with the magnetic field cause $E \times B$ drifts (thin arrows). The result is a propagation of the drift wave. The propagation speed in this simple picture is given by the electron diamagnetic drift velocity \mathbf{v}^* , i.e. the propagation velocity depends on the background density gradient (Eq. 2.7). The local electric fields do not appear in Eq. 2.7 although they finally cause the drifts that lead to propagation. The reason is that they are generated by the density perturbations which again depend on the background density gradient. For the following discussion the important point is that local electric fields have an influence on the propagation of the drift wave, although they do not appear in the equations due to the self-consistent description.

Fig. 6.14 b shows the eight exciter plates (bold) and the topology of the vacuum electric field generated by a $m_{ex} = 2$ exciter signal (dashed). The potential of the exciter plates is indicated by '+' and '-'. The important feature of this exciter field is that its azimuthal field strength depends on the azimuthal position. At the positively and negatively charged plates the azimuthal component is almost zero. Between these positions the orientation of the electric field is almost azimuthally, but with opposite direction for position 1 and 2. Additionally, the equi-density contour of a $m = 2$ drift mode (solid) and of a unperturbed density profile (dotted) are depicted. The propagation direction of drift wave and exciter signal is counter-clockwise. To demonstrate the influence of the exciter field on the drift wave, the drift wave is slightly displaced from the position of zero phase shift, i.e. the position where the drift wave maximum would directly face the positive exciter plate. Due to this displacement, the azimuthal field component of the exciter signal (red arrows) has different values on both sides of the density maximum, although the absolute value of the electric field (black arrows) is the same. To discuss the influence of this difference on the propagation of the drift wave, Fig. 6.14 c shows a zoom of the region of maximum density perturbation. The bold arrows indicate the azimuthal field related to the drift wave itself. The azimuthal field component of the exciter field is plotted below. Obviously, the additional azimuthal field component of the exciter field enhances the azimuthal electric field component on the one side ($+\delta E_\theta$) and decreases the azimuthal electric field at the other side of the density maximum ($-\delta E_\theta$). This results in a change of propagation velocity. The part marked by $+\delta E_\theta$ propagated faster and the part marked by $-\delta E_\theta$ slower. The resulting steepening of the wave on the slower side of the maximum increases the local electric field of the drift wave, i.e. the local propagation velocity increases (Fig. 6.14 d). The combination of both processes shifts the density maximum towards the position of zero phase shift. For displacements to the other side the mechanism reverses. This shows that in the framework of this simplified electrostatic picture the position of zero phase shift has an attractive character.

Nevertheless, to reduce the complexity of the problem this picture does not include the influence of sheaths on the exciter signal. However, these sheath will mainly attenuate the exciter signal, but they will not change the topology of the problem. Therefore, the qualitative findings will not change. To check the validity of this picture for drift wave models including instability mechanisms, i.e. phase shifts of density and poten-

tial, numerical simulations are needed. These simulations will have to solve the full set of equations including modulated boundary conditions due to the exciter signal, but this is beyond the scope of this work.

6.2 Multi-mode state

A more complex dynamic situation is found for the *multi-mode state*. In contrast to the single-mode state, the multi-mode state invokes several modes with different frequencies and wave numbers. Therefore, this state is suitable to attack the following questions:

- How will the system react if more than one mode is present?
- Is the driving process still mode selective?
- Is it possible to enhance or suppress other modes?

First, the initial state without driver signal will be described. Guided by the results obtained for the single-mode state, the following investigations with driver signal are restricted to co- and counter-rotating signals, because non-rotating signals are unlikely to comprise new dynamics.

6.2.1 Dynamics without exciter

To gain information on the initial state without driver signal, spectral techniques are used. Fig. 6.15 shows a plot of the spectral power density $S(f)$ and a color plot of the local frequency wave number power spectrum $S(f, k)$. Both spectra are recorded at $r = 25$ mm. A radially resolved measurement of the spectral power density is shown in Fig. 5.17. The power spectrum $S(f)$ shows basically three peaks at approximately $f_1 = 13.5$ kHz, $f_2 = 21.9$ kHz, and $f_3 = 30$ kHz. The spectral width of these peaks is about 2 kHz. The position of the peaks is shifting radially outwards with increasing frequency. The peaks are significantly broader than those observed in the single-mode state. The highest peak is clearly related to a wave number $k \approx 0.6 \text{ cm}^{-1}$. The peak at f_1 belongs to a wave number $k \approx 0.3 \text{ cm}^{-1}$. The third peak has only a very weak signature in the local frequency wave number spectrum. An analysis of several data sets reveals that its wave number is around $k \approx 0.8 \text{ cm}^{-1}$. These wave numbers indicate that the observed peaks are related to $m = 1$, $m = 2$ and $m = 3$ drift modes. The almost linear dispersion is in agreement with theoretical predictions from linear drift wave models. Nevertheless, an important fact is that the $m = 2$ mode is much stronger than the other modes. Especially the $m = 3$ mode is only slightly unstable. The peak height distribution reflects the results of growth rate calculations [115]. These calculations predict the $m = 2$ mode to be the most unstable, followed by the $m = 1$ and $m = 3$. The $m = 3$ mode is predicted to have a very small growth rate.

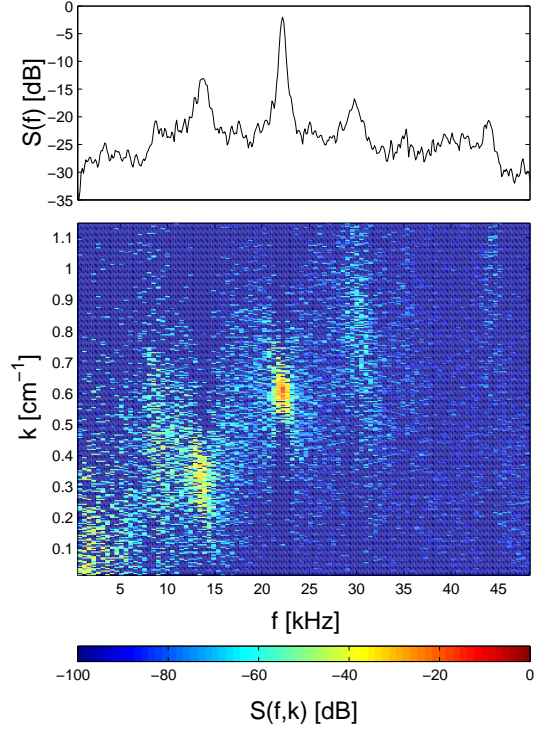


Figure 6.15: Spectral power density $S(f)$ and a color plot of the local frequency wave number power spectrum $S(f,k)$ for the undriven multi-mode state. Both spectra are recorded at $r = 25$ mm.

6.2.2 Dynamics with co-rotating exciter signal

To investigate the multi-mode state with driver signal, three different co-rotating driver signals are applied to the system. Their characteristics are summarized in Tab. 6.1. The frequencies are chosen as close as possible to the frequencies f_1 , f_2 and f_3 . The exciter mode number m_{ex} corresponds to the related drift mode number observed for that frequency. This is guided by the previous finding that matching temporal and spatial structure of driver and drift wave provide maximum coupling. The results observed for these driver signals are presented in Fig. 6.16 and 6.17. They will be discussed in the following paragraphs for each mode number separately.

drift mode	m_{ex}	f_{ex}	amplitude
$m = 1$	1	13333 Hz	8 V
$m = 2$	2	22221 Hz	8 V
$m = 3$	3	29761 Hz	8 V

Table 6.1: Characteristics of the applied, co-rotating driver signals. m_{ex} denotes the azimuthal mode number of the driver signal. f_{ex} is the applied driver frequency.

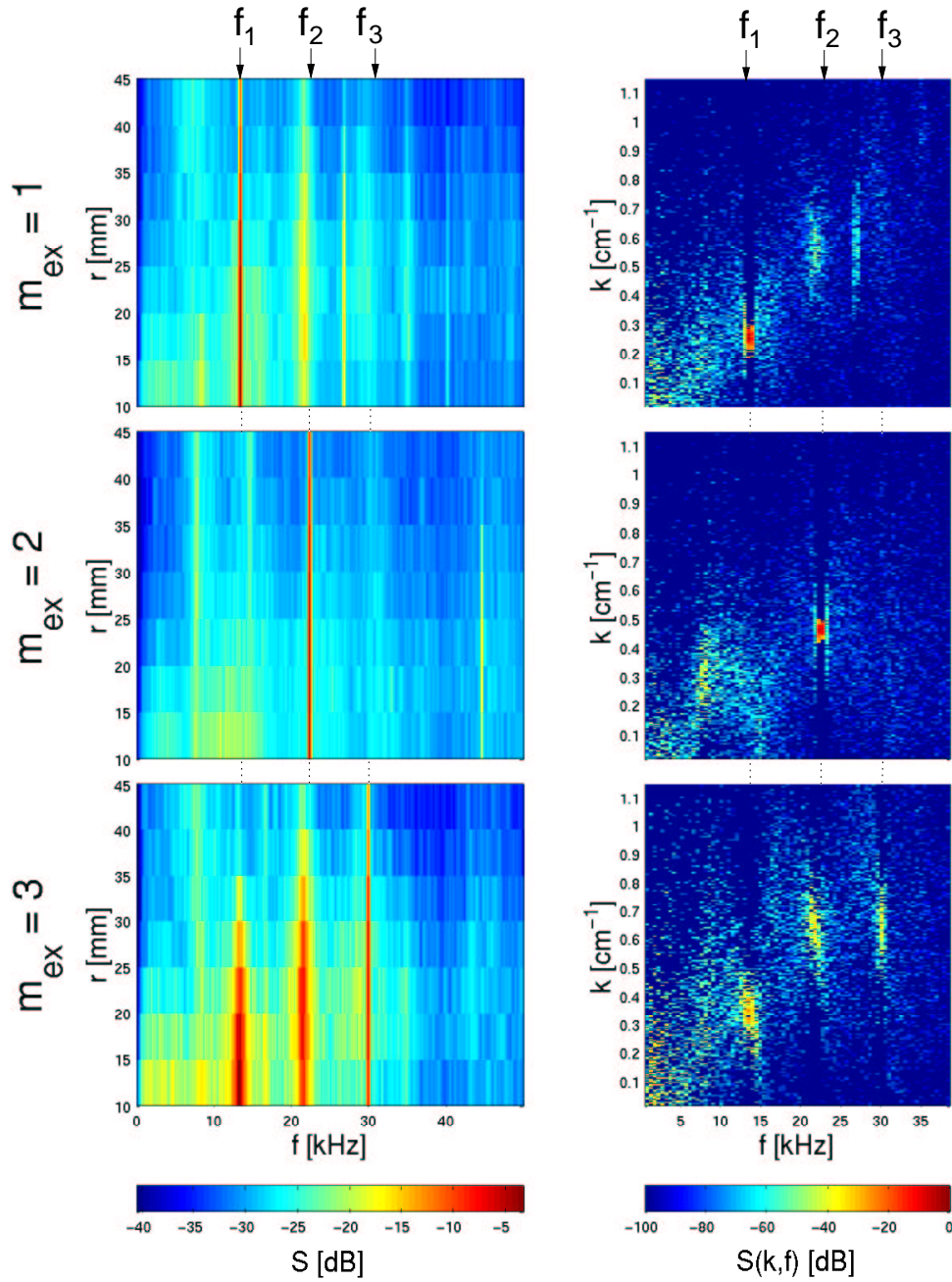


Figure 6.16: Spectral analysis of the driven multi-mode state for co-rotating driver signals specified in Tab. 6.1. The color plots on the left show the radial resolved power spectrum $S(f)$ for the three driver signals. The common color encoding is depicted below. The color plots to the right are local frequency wave number spectra $S(f,k)$ recorded at $r = 25$ mm. The color encoding is depicted below and is identical to those used in Fig. 6.15

m = 1: A comparison of Fig. 5.17 and Fig. 6.16 reveals that for a $m_{ex} = 1$ driver signal the peak amplitude at the driver frequency increases while it decreases around f_2 and f_3 . Additionally, the peak width is reduced for f_{ex} and a higher harmonic appears in the spectrum at $2f_{ex}$. The peak height decreases with radial position. The same spectral characteristics are obtained from $S(f, k)$ as well. Here, basically only one peak is observed. Compared to the initial state the wave number for f_1 stays nearly unchanged, but the peak is much more localized in k for the driven system. The conclusion from this data is, that the driver suppresses the $m = 2$ and $m = 3$ mode and enhances the $m = 1$. Although the driven system is not in a single-mode state, the power distribution among the modes has changed significantly. The dominant mode is now the $m = 1$ mode. Its amplitude is more than 3 times higher for the driven system than for the initial state. The $m = 3$ mode has disappeared completely and the $m = 2$ mode is suppressed by almost a factor of 6 in amplitude. These findings are supported by the phase sensitive measurements (Fig. 6.17). The coherent structures $\langle n \rangle_{coh}$ and $\langle \Phi_{f1} \rangle_{coh}$ have large amplitudes. The $m = 1$ mode structure is pronounced for both quantities. The radial and azimuthal extent of the positive (negative) fluctuations is large. The coherent fluctuation fraction goes up to 90 percent of all fluctuations in the system. Its coherence fraction slightly decreases with radius. The phase shift of density and potential is about $\pi/3$. The phase shift of maximum density and maximum exciter potential (denoted by 'max') indicates that the driver frequency for optimal synchronization should be little higher than the chosen $f_{ex} = 13333$ Hz. Indeed the frequency f_1 obtained from the undriven system, as best guess for the frequency of a $m = 1$ mode, is about 200 Hz higher.

m = 2: For $m_{ex} = 2$ the comparison of Fig. 5.17 and Fig. 6.16 reveals even more drastic changes than observed for $m_{ex} = 1$. The peak amplitude at the driver frequency increases while it nearly disappears around f_1 and f_3 . Additionally, the peak width for the $m = 2$ mode is reduced and a higher harmonic appears in the spectrum at $2f_{ex}$. The peak height at f_2 shows no radial dependence. In $S(f, k)$ basically one peak is observed. Compared to the initial state the wave number for f_2 stays nearly unchanged, but the peak is much more localized in k for the driven system. The conclusion from this data is, that for $m_{ex} = 2$ qualitatively the same behavior is observed as for $m_{ex} = 1$. The driver suppresses the non-resonant modes and enhances the mode with matching spatial structure. A difference is that for the $m_{ex} = 2$ driver signal the spectra of the driven system are comparable with those observed in a single-mode state. The phase sensitive measurements (Fig. 6.17) reproduce the spectral findings. The coherent structures observed in $\langle n \rangle_{coh}$ and $\langle \Phi_{f1} \rangle_{coh}$ have large amplitudes. The $m = 2$ symmetry is pronounced for both quantities. Compared with the $m_{ex} = 1$ driver the radial and azimuthal extent of the positive (negative) fluctuations is smaller. Again, the high coherent fluctuation fraction shows that nearly all fluctuations in the system are coherent. However, the radial dependence reveals some differences with respect to $m_{ex} = 1$. The maximum of the coherence fraction for $m_{ex} = 2$ is slightly shifted radially outwards compared to $m_{ex} = 1$. This indicates that the different modes are driven at different radial positions. A finding that would be in agreement with the linear theory of drift

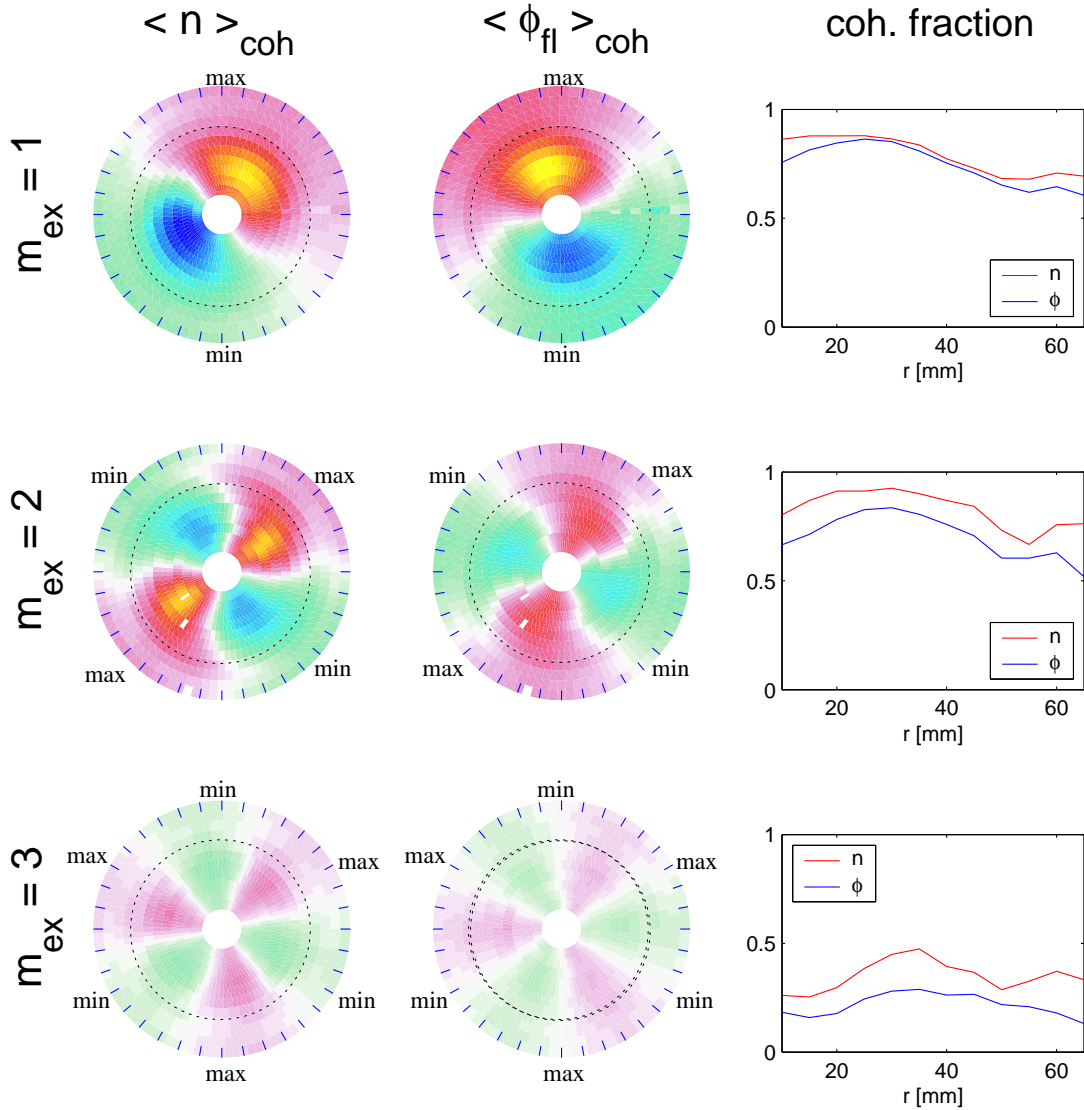


Figure 6.17: Phase sensitive measurements of density and potential fluctuations at the applied driver frequency. The color encoding and scaling of the color plots is common for all density (potential) plots. The exciter position is marked by the dotted circle. The positions of maximum and minimum exciter signal are marked with 'max' and 'min'. As reference the coherent fraction is plotted as function of radius. '1' denotes that all fluctuations in the system are coherent. '0' indicates no coherent fluctuations.

waves, which predicts a shift of maximum fluctuation amplitude radially outwards for increasing mode numbers. Although, this radial shift in maximum coherence fraction is not very pronounced, it is worth to keep this behavior in mind for the transport analysis presented in chapter 7. The phase shift of density and potential is found to be same as for $m_{ex} = 1$. In contrast to $m_{ex} = 1$ the phase shift of maximum density and maximum exciter potential indicates that the driver frequency for optimal synchronization should be little higher than the chosen $f_{ex} = 22221$ Hz.

m = 3: A completely different situation is found when the driver has a $m_{ex} = 3$ structure. Although a peak is observed for the driver frequency in $S(f)$ and the $m = 2$ mode is slightly suppressed, the $m = 1$ peak is enhanced. The same is apparent from $S(f, k)$. The spectral components related to $m = 1$ are enhanced while those belonging to $m = 2$ are damped. Interestingly, the peak related to f_{ex} is not observed at wave numbers corresponding to a $m = 3$ mode. These observations show clearly that the $m = 3$ mode is not enhanced by the $m_{ex} = 3$ driver. The enhancement of the $m = 1$ mode indicates a super harmonic synchronization, as $f_{ex} \approx 2f_1$. Additional to the temporal super-harmonicity a spatial super-harmonicity is included due to the mismatch of spatial structure of $m = 1$ drift mode and $m_{ex} = 3$ driver. That despite of this spatial and temporal mismatch synchronization could be achieved can be shown with help of the phase sensitive measurements. A superposition of spatial structure for $m = 1$ and $m = 3$ shows that for matching positions of a maximum of $m = 3$ and the maximum of $m = 1$ result in a configuration, where opposite to this matching maximum positions matching positions of minima are found as well. Only the regions in between do not match. This partly spatial matching combined with harmonic frequencies could explain why the $m = 1$ mode is weakly driven. This mechanism would lead to a suppression of the $m = 2$ mode as well, because neither the spatial structure nor the temporal structure are harmonic. Although a $m = 3$ mode is not observed in $S(f, k)$, the phase sensitive measurement shows a $m = 3$ structure. This is related to the harmonic frequencies of $m = 1$ and $m_{ex} = 3$ and the insensitivity of the phase sensitive averaging technique to suppress harmonic frequencies.

6.2.3 Dynamics with counter-rotating exciter signal

For counter-rotating signals the situation changes significantly. The applied signals have the same characteristics as described in Tab. 6.1, just the propagation direction has been reversed. The results observed for these driver signals are presented in Figs. 6.18 and 6.19. For all exciter mode numbers m_{ex} , the spectral analysis reveals no significant changes compared to the undriven system. The power spectrum only shows an additional peak at the driver frequency f_{ex} . The peaks related to the drift modes $m = 1 \dots 3$ are enhanced or damped notably. The frequency wave number spectra show no peaks corresponding to a counter rotating wave established in the system. The spectral power distribution is less localized in k for the mode number corresponding to m_{ex} . Another change in $S(f, k)$ is observed for $m_{ex} = 1$. In this case, a shift of the peak related to $m = 1$ is shifted towards $k = 0$. This means the corresponding wave length is tend-

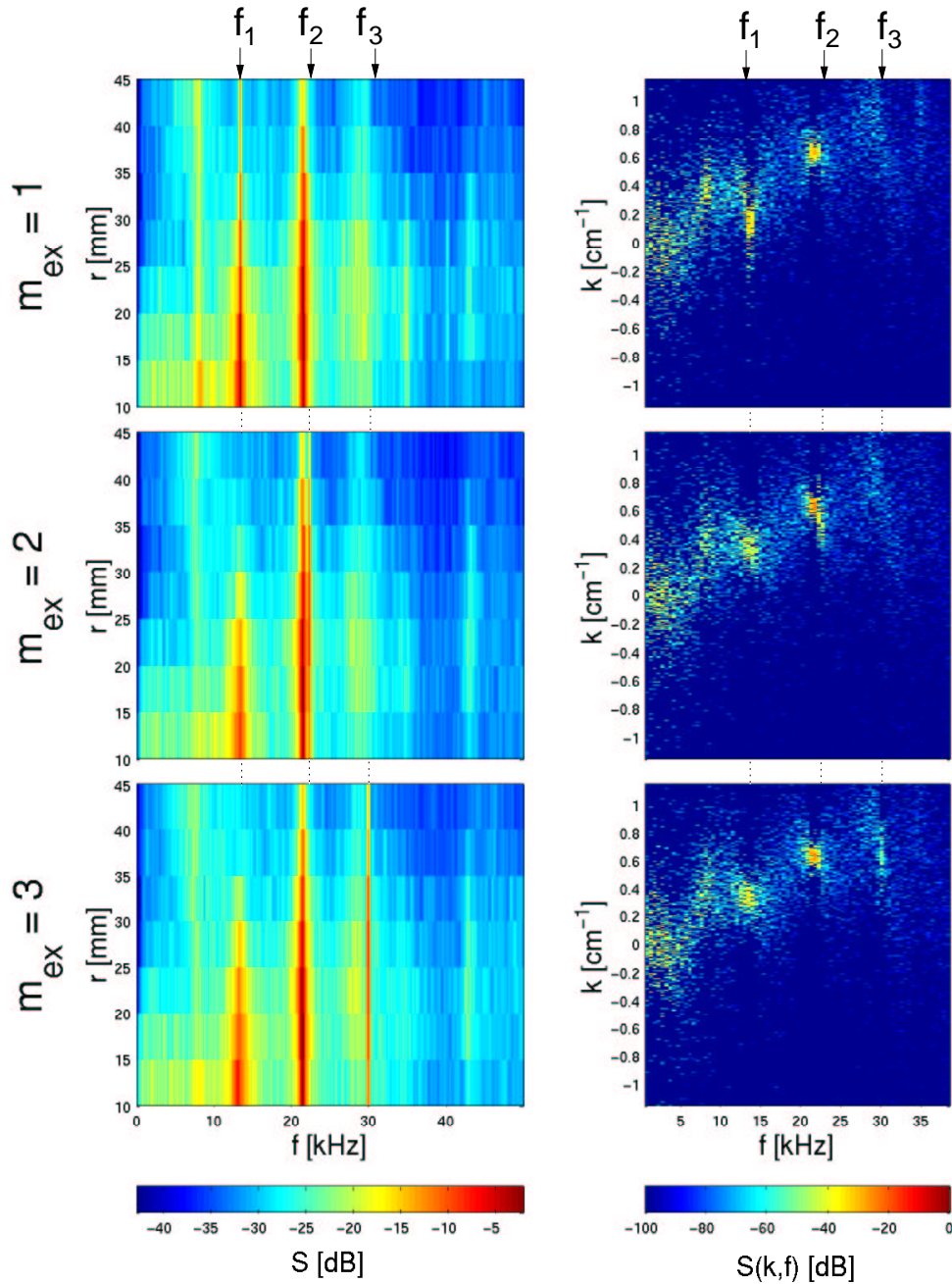


Figure 6.18: Spectral analysis of the driven multi-mode state for counter-rotating driver signals specified in Tab. 6.1. The color plots on the left show the radial resolved power spectrum $S(f)$ for the three driver signals. The common color encoding is depicted below. The color plots to the right are local frequency wave number spectra $S(f,k)$ recorded at $r = 25$ mm. The color encoding is depicted below and is identical to those used in Fig. 6.15

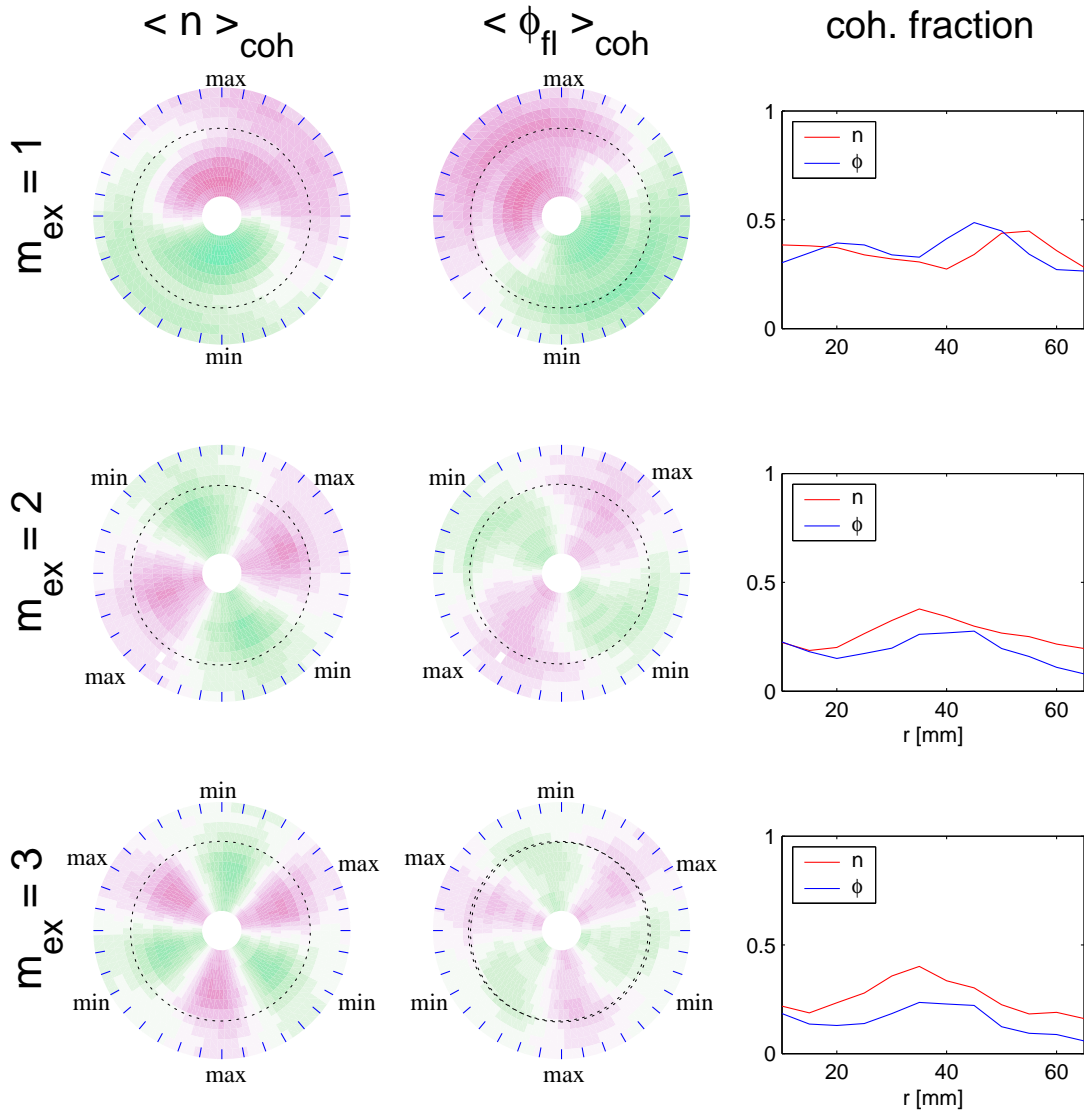


Figure 6.19: Phase sensitive measurements of density and potential fluctuations at the applied driver frequency. The color encoding and scaling of the color encoding is the same as in Fig. 6.17. The exciter position is marked by the dotted circle. The positions of maximum and minimum exciter signal are marked with 'max' and 'min'. As reference the coherent fraction is plotted as function of radius.

ing towards infinity. Whether this effect is artificial or not can not be judged from the data, but structures with an azimuthal wave number $k = 0$ are well known as zonal flows and are discussed in combination with confinement in fusion experiments [44]. The phase sensitive measurements show weakly established coherent structures for all driver modes. They originate from the insensitivity of the method to propagation direction, i.e. waves with $\pm k$ can not be separated. Consequently the coherent structures are related to the peaks observed in $S(f, k)$ and not with counter-rotating waves. Additionally, the low coherence fraction shows that the observed structures are not dominant.

6.3 Synopsis

In this chapter, synchronization experiments of drift waves with spatio-temporal driver signals have been presented. The the main results will be summarized in the following paragraphs.

The basic measurements of the drift wave dynamics for different exciter modes clearly revealed, that the spatial component of the exciter signal plays a significant role. Only for matching spatial and temporal structures of driver and drift wave a strong interaction between drift wave and driver signal is observed. The observed temporal nonlinear dynamics, e.g. quasi-periodicity, periodic pulling and synchronization, are in good agreement with those observed for a driven van der Pol oscillator. This is rather surprising because the van der Pol model is a description for a purely temporal *oscillatory* system and not for a spatio-temporal wave system.

Spatio-temporal investigations have shown that the observed temporal dynamics are related to spatio-temporal processes. It was found that the driver signal directly influences the propagation velocity of the drift wave. The propagation velocity of the synchronized drift wave is identical with the propagation velocity of the spatial driver signal, i.e. the drift wave is accelerated or decelerated, depending on the ratio of propagation velocity of driver and undriven drift wave. The preferred phase shift between driver signal and drift wave is found to be zero for the synchronized state. Deviations from this position depend on the initial propagation velocity mismatch of the driver signal and the undriven drift wave. The analysis of this dependency revealed that this position has an attractive character, although the drift wave extrema directly face exciter plates of same charge. It is proposed that the attractive character of this position is related to the influence of the azimuthal component of the electric exciter field on the processes of drift wave propagation.

The spatio-temporal dynamics of periodic pulling have been investigated as well. The measurements have shown that the pulling process has to be described by a modulation of propagation velocity of the drift wave. Additionally, a compression and stretching of the drift wave is observed. The simultaneous compression of e.g. the wave crest and the stretching of the wave trough assures a constant 'wave length', which is determined by the periodic azimuthal boundary conditions.

For a multi-mode state the synchronization process is found to be mode selective.

The modes, which do not match the spatio-temporal structure of the exciter signal, are generally suppressed with the exception of super-harmonic synchronization. The strength of mode suppression is found to depend on the stability of the modes within the system. The most unstable mode ($m = 2$) can be driven most effectively to suppress the other modes. Modes with small growth rate ($m = 3$) cannot be driven efficiently.

Generally speaking, the measurements clearly show that the spatio-temporal driver signal influences the drift wave dynamics for single and multi-mode states. The temporal dynamics are known from other driven systems, but the spatio-temporal analysis of the driven drift wave system exhibits new dynamical phenomena.

Chapter 7

Effects of synchronization on transport

The investigations on drift waves have been linked with investigations on anomalous transport from the very beginning [4]. Hence, the various attempts to influence the drift wave dynamics were mostly made in order to reduce transport [40, 42, 43]. In chapter 6 it has been shown that the driver signal influences the drift wave dynamics for single and multi mode states. Due to this change in dynamics it is likely that the fluctuation-induced transport, generated by drift waves, is affected as well. Therefore, the effects of synchronization on transport are studied for a single-mode and multi-mode state in this chapter. The basic questions to be answered are:

- Is fluctuation-induced transport affected by the driver?
- Is this influence universal or does it depend on the mode structure of the driver signal?
- Can the reason for a change of fluctuation-induced transport be identified?

7.1 Single-mode state

Again, it is helpful to start with the simpler dynamics of the single-mode state to investigate the influence of the driver signal on transport¹. First, a characterization of the observed transport without driver signal is given. Second, the effects of a driver signal on average and spatio-temporally resolved transport are discussed for complete and incomplete synchronization. All transport informations are obtained from triple probes (see chapter 5). To achieve reasonable statistics, a record length of 256 KWords is chosen. An accurate phase information is provided by a simultaneously recording of the driver signal for every data set.

¹The more precise terminology 'fluctuation-induced' is omitted in the following.

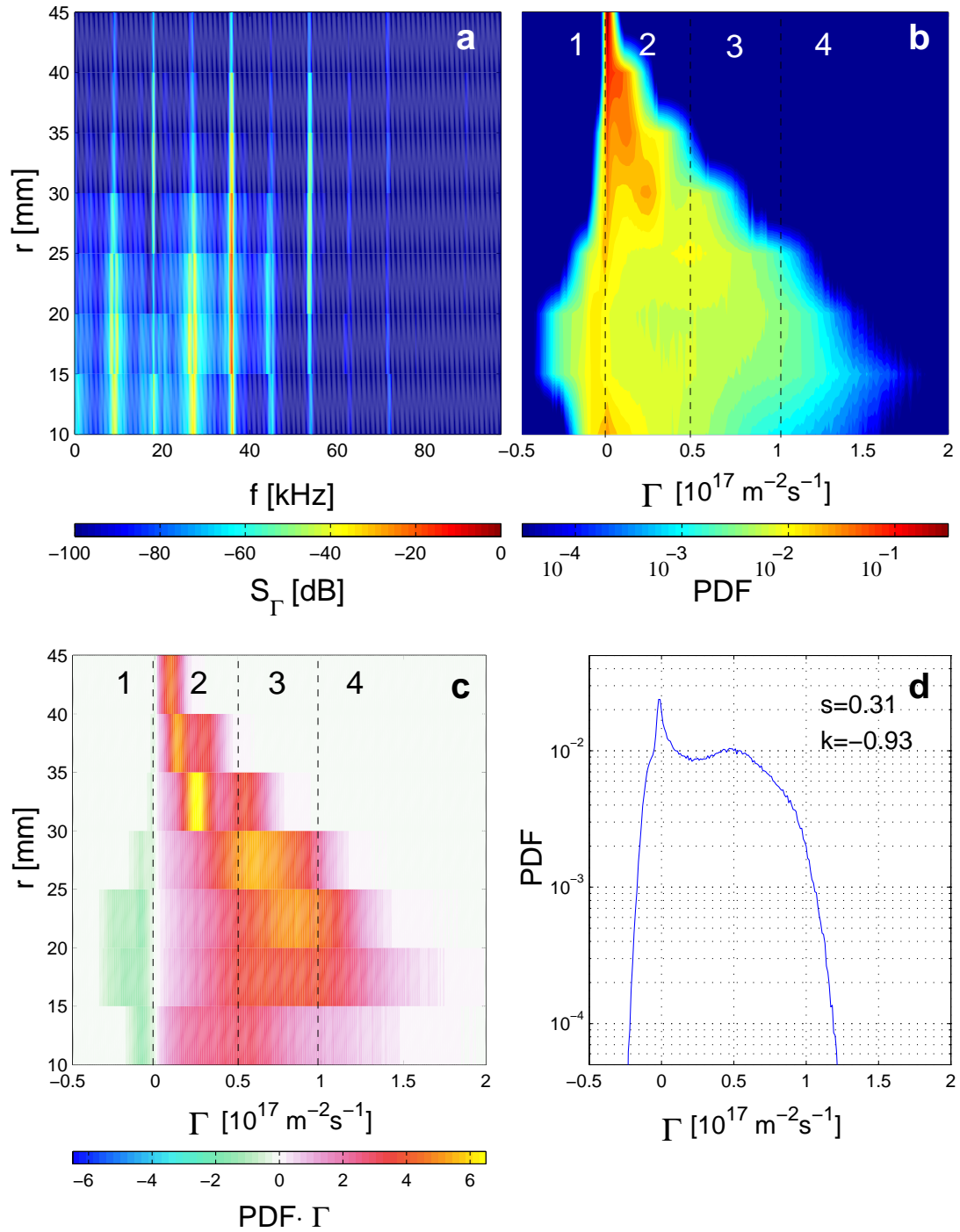


Figure 7.1: Analysis of the undriven system. (a) Color plot of power spectrum S_Γ as function of radius. (b) Radially resolved PDF of Γ . The numbers are related to the transport classification. (c) Color plot of transport flux fraction. (d) PDF at $r = 25$ mm. 's' and 'k' denote skewness and kurtosis according to chapter 4.

7.1.1 Transport without driver signal

The single-mode state and its fluctuation characteristics have already been described in detail in chapter 5 and 6. It was found that the density and potential fluctuations are monochromatic. Therefore, the transport Γ is expected to be monochromatic as well. Fig. 7.1 a shows the power spectrum of Γ as a function of radius. The dominant peak is found at $f_2 \approx 36$ kHz. This is twice the frequency of the density and potential fluctuations. This finding is in agreement with theory (see Eq. 2.31), which states that the main contribution to transport is found at the first harmonic of the driver. The peak at $f_1 \approx 10$ kHz is related to a weak $m = 1$ mode. The other peaks are sidebands, i.e. they are found at frequencies $f = mf_1 \pm nf_2$, with integer numbers n and m . These peaks have at least 40 dB lower amplitude compared to the peak at f_2 . They are not relevant for the following studies, because their contribution to transport is negligible. The spectrum confirms that radial changes in peak amplitude are related to the radial fluctuation profile of density and potential. This radial change in fluctuation amplitude is directly observable in Fig. 7.1 b. The color plot shows the PDF of Γ as a function of radius. For all radial positions the PDF is peaked at $\Gamma = 0$ and shows a strong asymmetry with respect to $\Gamma = 0$. To give a better visualization of its shape the PDF for $r = 25$ mm is plotted in Fig. 7.1 d. The flat top profile with two peaks is typical for a harmonic signal. The fact that mostly outward transport is observed, reflects the phase shift between density and potential fluctuations. In chapter 6 this phase shift was found to be about $\pi/3$. If this phase shift is applied to Eq. 2.31, Γ is found to be directed outwards for almost all times. Generally, this asymmetry in the PDF shows that there are many medium and large transport events radially outwards and only few small transport events inwards.

How much these different sizes of transport events contribute to transport is specified by the transport flux fraction. The transport flux fraction is defined as the product of PDF and Γ . Its radial dependence is plotted in Fig. 7.1 c. With the help of Fig. 7.1 d an empiric classification for transport events can be introduced:

- 1) **inwards:** $-0.5 < \Gamma \leq 0$
- 2) **small:** $0 < \Gamma \leq 0.5$
- 3) **medium:** $0.5 < \Gamma \leq 1$
- 4) **large:** $1 < \Gamma$

where Γ is given in $10^{17} \text{ m}^{-2}\text{s}^{-1}$. The intervals are chosen to have the same size and to cover the whole PDF. Additionally, the boundary between small and medium has been set to the position of the local maximum of the PDF. The definition of 'large' implies for a nearly harmonic signal that large events should be rather rare. Although the classification is mainly guided by eye, the obtained results are similar for other definitions. With this definition it is found that less than 1 % of the transport is inwards. The dominating part is outwards. About 33 % of the transport are due to small events

and only 4% are caused by large events. The remaining 64% have their origin in medium-sized transport events.

To summarize, the transport without driver Γ_{ref} is found to be harmonic and the main contribution to the transport is by medium transport events. The radial shape can be understood from the radial mode structure of the drift waves.

7.1.2 Influence of synchronization on transport

To investigate the influence of the driver signal on transport, the transport is recorded at different radial positions for $m_{ex} = 2$ driver signals with frequencies from 16 to 20 kHz. The frequency step width is $\Delta f = 200$ Hz. For each radial position a data set without applied driver signals is recorded as well, to take small plasma parameter drifts into account. The results are plotted in Fig. 7.2. The color plot shows the average transport of the driven system, which has been normalized to the average transport of the undriven system. The frequency scale has been normalized to the drift wave frequency f_0 without driver signal. The second plot in Fig. 7.2 shows the normalized average transport at radial position $r = 25$ mm. The frequency domain of complete synchronization is marked. It is seen that the average transport is reduced significantly for almost matching frequencies at all radial positions. The transport reduction is about 30%. The errors are estimated to be $\pm 5\%$. An enhancement of transport is not observed.

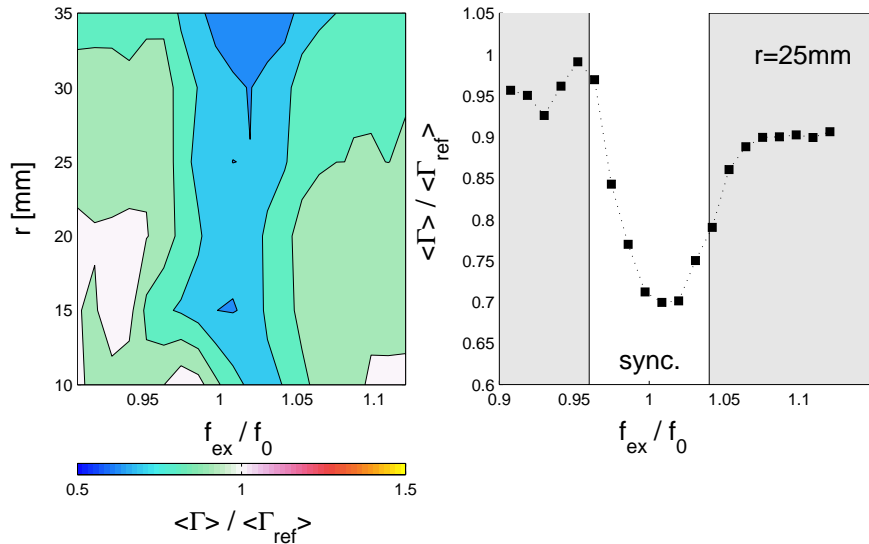


Figure 7.2: The color plot shows the average transport for a co-rotating $m_{ex} = 2$ driver signal applied to a $m = 2$ mode as a function of radius and driver frequency. The transport is normalized to the average transport without driver signal. f_0 denotes the drift wave frequency without applied driver signal. The right plot shows the normalized average transport as function of driver frequency at $r = 25$ mm. The region, where complete synchronization is observed, is marked.

Temporal transport properties

To achieve information on the origin of the transport reduction a close investigation of the temporal transport properties is needed. Due to the length of the time series, it is difficult to obtain information by visual inspection of the transport time series. Instead, spectral and statistical tools have to be used. The results are shown in Fig. 7.3 a-d. The spectral information on transport for the driven system is plotted in Fig. 7.3 a. It shows the spectral power density for the different driver signals at $r = 25$ mm. The power spectrum of the undriven system is plotted above. The region of synchronization is clearly distinguished from those regimes, where periodic pulling and quasi periodicity are observed. Compared to the reference spectrum a significant change for the regime of synchronization is not observed. For the regimes of periodic pulling and quasi periodicity, pronounced side band structures and their harmonics are apparent. Therefore, the spectral analysis provides information on the dynamic state of the system, but it does not explain the observed transport reduction. Fig. 7.3 b compares the PDFs for different driver frequencies. The PDF for the undriven system is plotted above. A comparison of the reference PDF with those plotted below reveals, that for complete synchronization the large transports events are reduced, while for periodic pulling and quasi periodicity the large transport events are enhanced. This qualitative finding is quantified by Fig. 7.3 c. The plot shows the change of the PDF compared to the PDF of the undriven state. The reduction of medium size events is as clearly observed as the enhancement of small size events. For periodic pulling and quasi periodicity an additional enhancement for large transport events is visible. To answer the question of responsibility for the observed transport reduction, Fig. 7.3 d shows the change of transport flux fraction with respect to the undriven system. Obviously, the observed transport reduction is related to the reduction of medium size transport events. This visual impression of transport reduction and enhancement is quantified by integration over the flux fraction for the different event sizes. With a normalization to $\langle \Gamma_{ref} \rangle$, the result of this calculation is the relative change in transport. For synchronization the enhancement of small transport events gives an increase in transport of 4 %. This increase is exactly canceled by the transport reduction found for large transport events. For the driven system large transport events are not observed. For medium transport events the reduction in transport is found to be about 30 %. This agrees exactly with the reduction observed for average transport. The net change for inward transport events is zero. A comparison of the change in flux fraction for $f_{ex}/f_0 = 0.9$ and $f_{ex}/f_0 = 1.1$ might lead to the interpretation that the difference in average transport observed for these states is caused by the large transport events. This interpretation is not justified, because the statistics for large transport events is not sufficient. This is seen by splitting of the transport time series into ten sub-series. The resulting deviation in average transport for these subseries is about $\pm 5\%$ and is caused by the bad statistics for large events. This shows that the observed asymmetry for $f_{ex}/f_0 < 1$ and $f_{ex}/f_0 > 1$ is within error bars. However, the transport reduction of up to 30 % for synchronization is still significant.

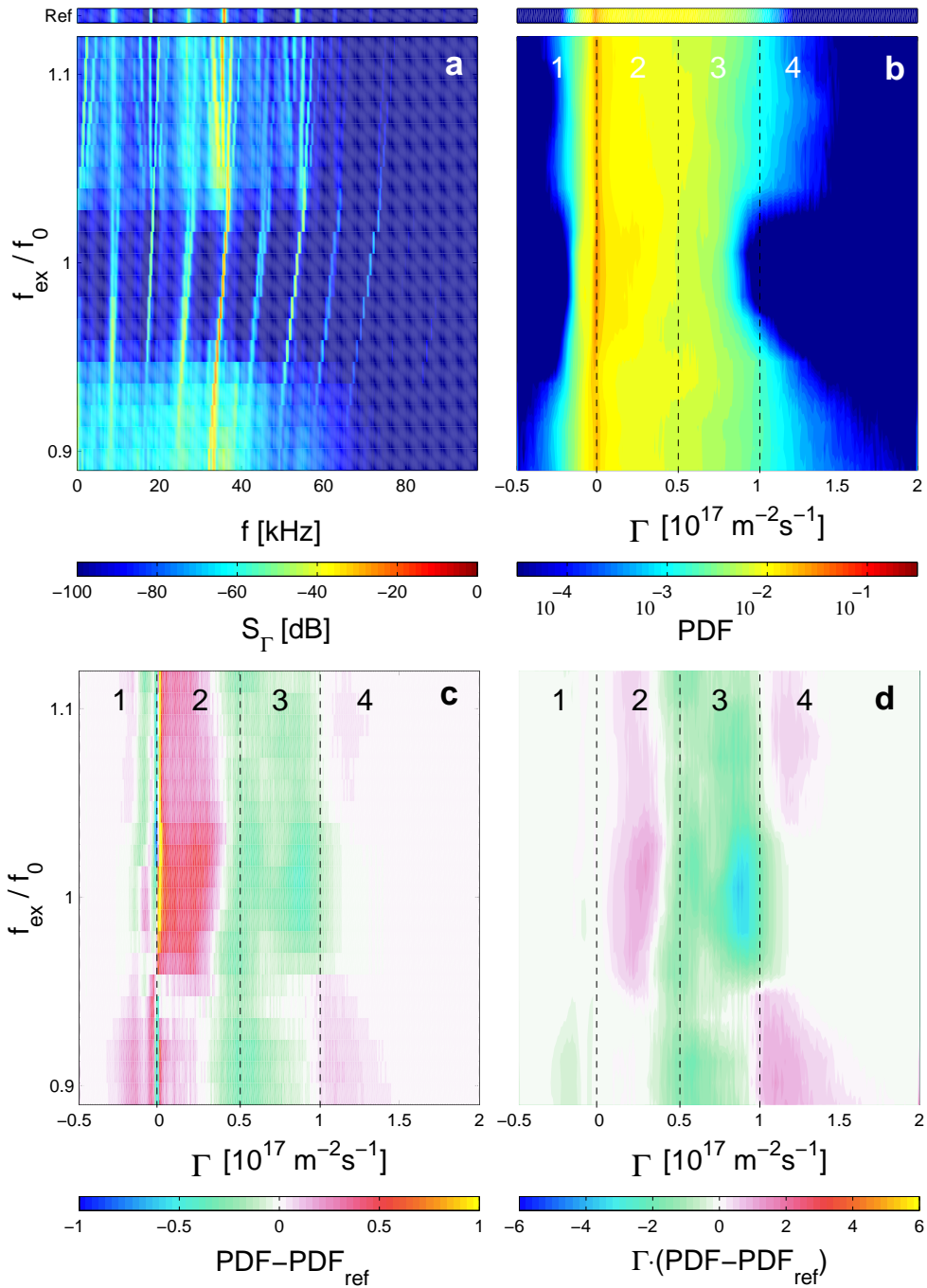


Figure 7.3: Analysis for co-rotating $m_{ex} = 2$ driver signal. (a) Color plot of power spectrum S_Γ as function of f_{ex}/f_0 . (b) PDF of Γ as function of f_{ex}/f_0 . The numbers are related to the transport classification. (c) Color plot to visualize changes of PDF. (d) Color plot of change of transport flux fraction. The color scale is identical with those in Fig. 7.1 c.

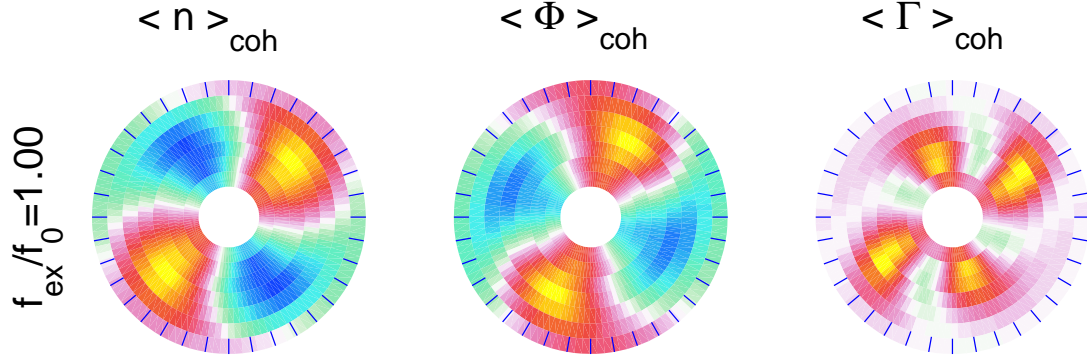


Figure 7.4: *Coherent fluctuations of density, potential and transport for a synchronized system. The green areas mark inwards transport while the yellow-red indicate outward transport.*

Spatial transport properties

The harmonicity of the transport signal gives the opportunity to investigate the spatial transport properties. For synchronization density and potential fluctuations are recorded simultaneously for various radial positions. With help of the phase sensitive averaging method, the coherent fraction of both signals can be extracted (Fig. 7.4). The product of coherent density and potential fluctuations yields the coherent transport. The spatial structure of the coherent transport has a clear $m = 4$ mode structure. The structure propagates azimuthally with the same speed as the coherent density fluctuations. This leads to frequency doubling, e.g. $f_{\Gamma} = 2f_0$. Therefore, the spatial structure of the transport explains the observed spectrum $S_{\Gamma}(f)$. Further, it is found that the regions of outward transport are much more pronounced than those of inward transport. This asymmetry is the result of the phase shift of density and potential of about $\pi/3$ (see Fig. 2.4). Additionally, this asymmetry explains the shape of the observed PDFs. The weak inward transport results in only few negative transport events observed in the PDF. The dominant, coherent, outward transport is observed as local maximum. Hence, the fluctuations are harmonic, but their average is not zero.

To conclude, the spatial structure of the coherent transport is in agreement with the theoretical picture given in chapter 2. The asymmetry of inward and outward transport is caused by phase shift of density and potential and explains the shape of observed PDFs. This shows that the temporal and spatial transport signals are directly linked. The dominant coherent transport structures determine the temporal transport properties.

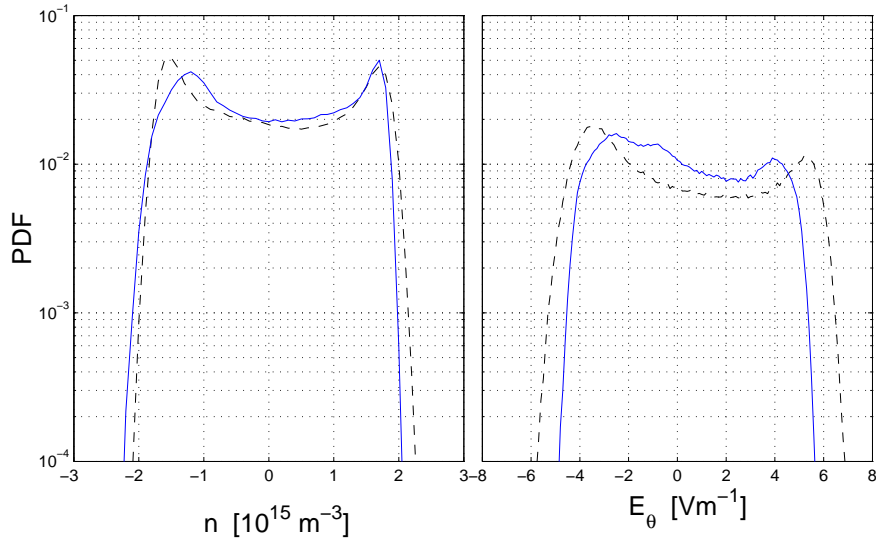


Figure 7.5: PDFs of density and azimuthal electric field for co-rotating $m_{ex} = 2$ driver signal applied to a $m = 2$ drift mode (solid) and undriven system (dashed). The time series are recorded at $r = 25$ mm.

What causes transport reduction?

In the foregoing sections it has been shown that a change of transport properties is observed. Due to its definition, a change of transport is related to changes of density and potential fluctuations. The theoretical treatment and the measurements of spatial and temporal transport properties show that basically three effects can cause a change of average transport:

1. A change of density and/or potential fluctuations amplitude.
2. A change of phase shift between density and potential fluctuations.
3. A change of shape of density and/or potential fluctuations, i.e. localized phase shifts.

To check to what extent amplitude changes are responsible for the observed transport reduction, Fig. 7.5 depicts the PDFs for density and azimuthal electric field fluctuations recorded at $r = 25$ mm. The slight changes of the density fluctuation amplitude do not change the average amplitude significantly, but the changes of the azimuthal electric field fluctuation are significant. The average amplitude of the electric field fluctuations is reduced by about 25 %. This reduction is due to an overall reduction in electric field fluctuation amplitude. With the assumption of unchanged phase between density and potential the observed amplitude reduction would lead to a transport reduction of 25 %. This is of the order of the observed overall transport reduction. Interestingly, these changes support the findings of chapter 6, where the azimuthal electric field was proposed to play a significant role for the synchronization process.

However, transport is very sensitive to phase changes for certain phase values (see Eq. 2.31). This means that an absolute accuracy of about $\pm 10^\circ$ in phase measurement results in an absolute accuracy for the average transport of $\pm 15\%$ for the observed phase shift of 60° . Therefore, an influence on transport by phase changes can not be excluded.

A change in shape of the fluctuations might be deduced from the change in maximum position of the PDFs for negative values, but its influence on transport cannot be estimated because of the missing phase relation.

To summarize, the observed changes in transport cannot be clearly related to phase, amplitude or shape changes, but the change in electric field amplitude would lead to a change in transport that is comparable to the overall change in transport. This indicates that the other mechanisms are not dominant or cancel.

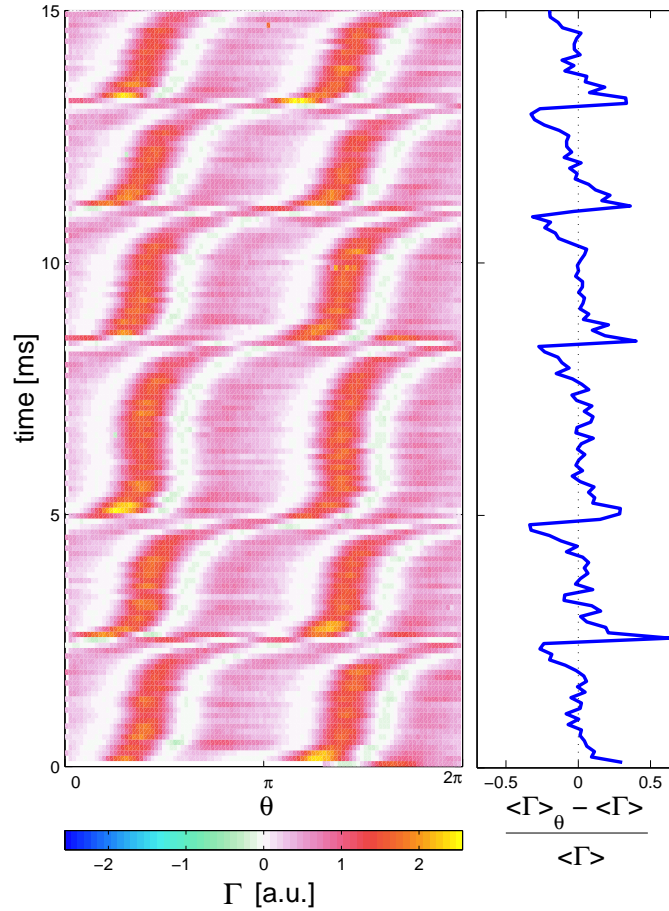


Figure 7.6: *Spatio-temporal transport measurement for periodic pulling. The color plot shows the transport as function of azimuthal position and time. The right plot shows the relative deviation of the azimuthally averaged transport from the spatio-temporal average. The plot is normalized to spatio-temporally averaged transport.*

7.1.3 Transport and Periodic Pulling

It has been shown in chapter 3 that periodic pulling is a combination of amplitude and phase modulation. As transport depends on both amplitude and phase, it is interesting to study how periodic pulling influences transport. For this purpose a statistical approach is not promising. In chapter 6 it has been shown that periodic pulling of drift waves is a spatio-temporal process. Hence, information on average values or their PDFs is not likely to give insight into the effect of periodic pulling on transport. Instead, spatio-temporally resolved measurements of transport are needed. For this purpose the phase sensitive measurement technique is used at a single radial position ($r = 25$ mm). The result is depicted in Fig. 7.6. The color plot shows the transport as function of azimuthal position and time. The reference frame is the co-rotating frame of the driver signal. As in Fig. 7.4 the spatial component shows a $m = 4$ mode structure. In combination with the temporal evolution, the periodic pulling process is clearly observed. The transport signal shows the same characteristic signature of propagation velocity modulation as observed for the density fluctuations (Fig. 6.9). Additionally, an amplitude modulation is observed. When the systems starts to unlock the transport is first reduced and afterwards enhanced. This systematic amplitude modulation is more evident in the azimuthally averaged transport data. The plot to the right shows the relative deviation of the azimuthally averaged transport from spatio-temporally averaged transport. The plot is normalized to spatio-temporally averaged transport, e.g. '0.5' denotes an increase in transport of 50 % compared to spatio-temporal average. For each unlocking process a transport reduction followed by an transport enhancement is observed. The peak-to-peak transport modulation amplitude is of the order of 60-80 %.

The origin of this transport modulation can either be an amplitude modulation of density and/or potential or a phase modulation. The latter can not be investigated, because the definition of 'phase' is critical for the periodic pulling process (see chapter 6). The very limited number of minima and maxima in azimuthal direction and the local deformation make it difficult to distinguish amplitude and phase modulation, but nevertheless the modulation of the peak amplitude can be studied. To determine the influence of amplitude modulation on transport, the relative transport deviation is plotted together with the relative peak-to-peak amplitude modulation of density and electric field in Fig. 7.7. The positions of zero crossing in relative transport deviation are marked by ticks. A comparison of relative density deviation and relative transport deviation reveals that they are obviously linked. The relative density and transport deviation are nearly identical. The link between transport and azimuthal electric field is less pronounced. First, the electric field modulation is weaker, its maximum values are around 20 %. Second, the electric field does not show the same amplitude modulation as the transport, but maximum electric field seems to be linked with the unlocking process, while for the locked period the electric field is usually lower than its spatio-temporal averaged value. That the amplitude modulation of electric field and density is at least in parts responsible for the observed transport modulation is demonstrated with the time series of the product of n and E . This time series shows that the transport

time series is reproduced qualitatively.

Therefore, it can be stated that periodic pulling has an influence on transport. The observed modulation is at least partly the result of an amplitude modulation of density and potential and not necessarily related to phase modulation.

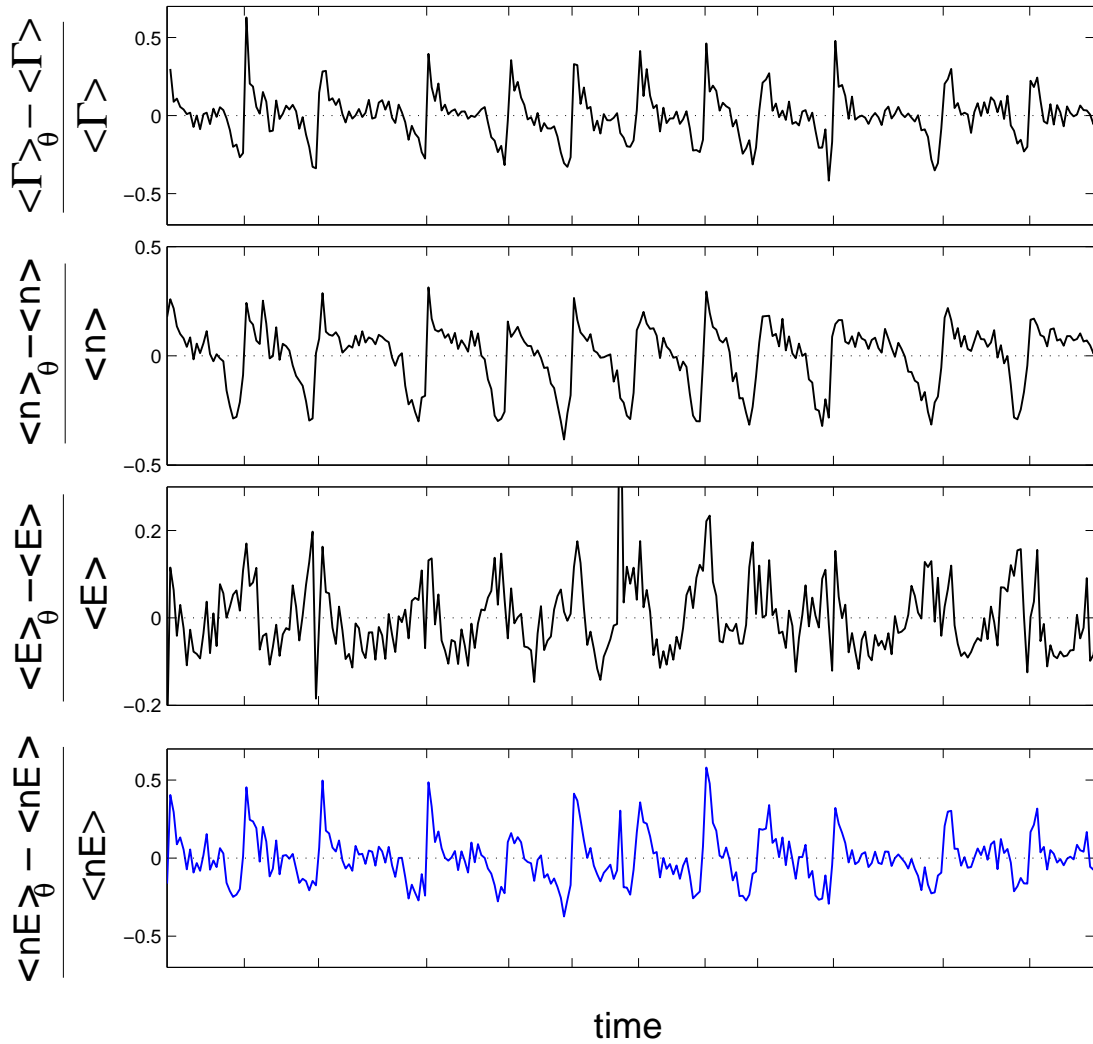


Figure 7.7: Time series of (a) relative modulation of spatially averaged transport, (b) relative peak to peak density modulation and (c) relative modulation of peak to peak azimuthal electric field. (d) shows the product of relative density and azimuthal electric field modulation. All time series are normalized to their spatio-temporal average.

7.2 Multi-mode state

In most systems, where transport studies are of interest, the plasma dynamics are turbulent, i.e. the fluctuation-induced transport originates from several, interacting drift modes. To start with transport investigations in a driven turbulent system is not promising. The complicated dynamics would inhibit a clear interpretation of the observed phenomena. The multi-mode state is more suitable for a detailed study. Its dynamics are related to just three, interacting drift modes. It will allow to study the influence of the exciter signals on transport for different mode structures in a simpler system and still answer general questions like:

- Does the driver increase or reduce transport?
- Does this influence depend on the mode structure of the driver?

7.2.1 Transport without driver signal

First, it is essential to discuss the transport properties of the undriven system, because they are used for reference later on. The scaling of the plots in Fig. 7.8 is identical to those used for the single-mode state to allow for a better comparison.

Fig. 7.8 a shows the transport power spectrum of the multi-mode state. In contrast to the single-mode state, a number of spectral components is observed, which form an almost continuous spectrum below 40 kHz. Only the density fluctuation related to the $m = 2$ drift mode can be related to the pronounced peak at $f = 41$ kHz. For the $m = 1$ and $m = 3$ drift modes pronounced peaks at twice the frequency of the density fluctuations are not observed.

That the transport fluctuations are not harmonic is shown by the PDFs as well (Fig. 7.8 b and d). The PDF is peaked at $\Gamma = 0$ and is still asymmetric and most of the transport events are directed outwards, but the typical second peak for harmonic signals has disappeared. The shape of the PDF is rather similar to those found for weakly turbulent states. The absolute transport reduction compared to the single-mode state is caused by a lower equilibrium plasma density due to the modified discharge parameters, i.e. lower density fluctuations amplitude [80]. Nevertheless, the relative fluctuation amplitudes are comparable for single and multi-mode state. Due to this reduction, the empirical classification for the transport events has to be adapted. The new definitions are:

- 1) **inwards:** $-0.3 < \Gamma \leq 0$
- 2) **small:** $0 < \Gamma \leq 0.3$
- 3) **medium:** $0.3 < \Gamma \leq 0.6$
- 4) **large:** $0.6 < \Gamma$

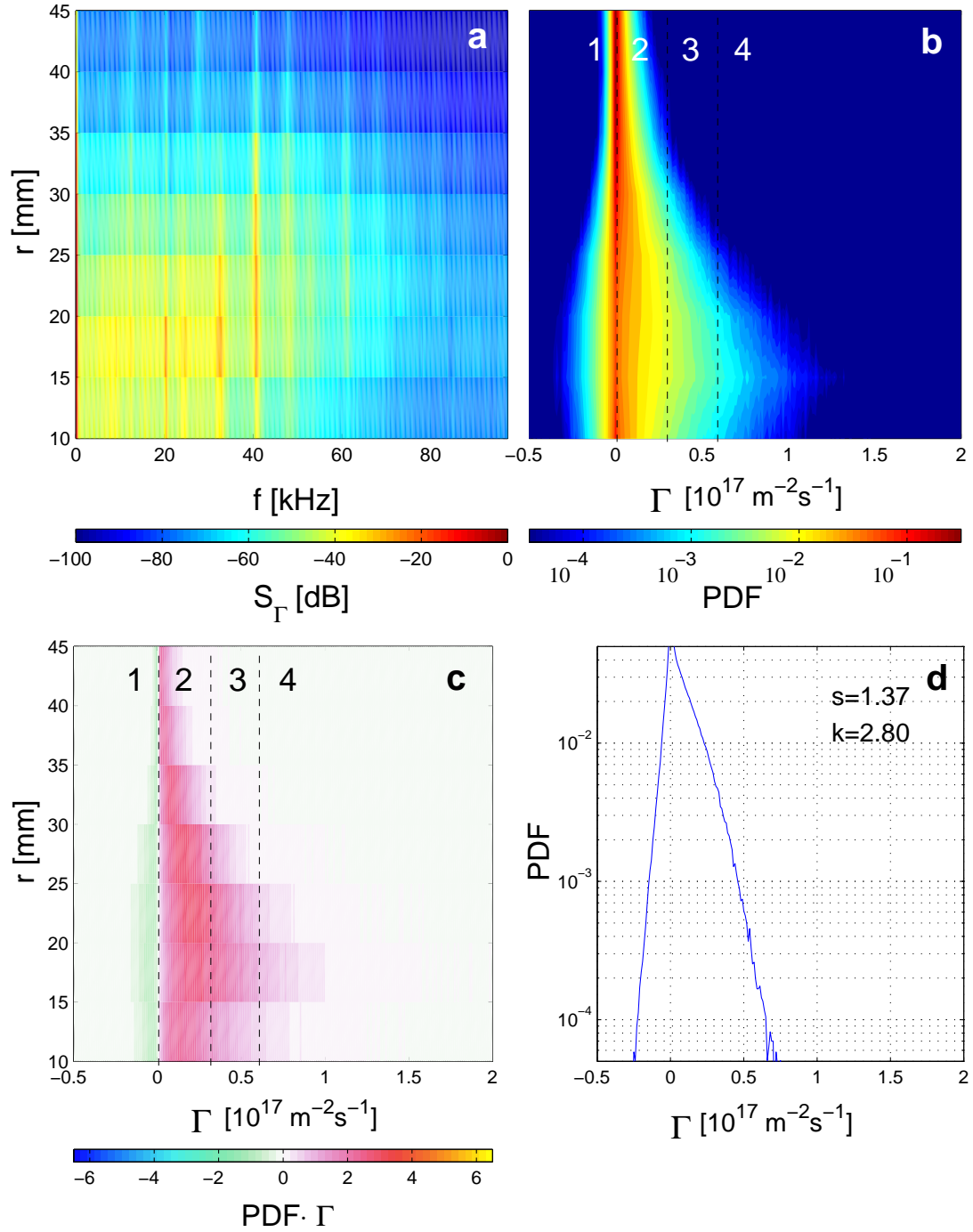


Figure 7.8: Analysis of the undriven system. (a) Color plot of power spectrum S_Γ as function of radius. (b) Radially resolved PDF of Γ . The numbers are related to the transport classification. (c) Color plot of transport flux fraction. (d) PDF at $r = 25$ mm. 's' and 'k' denote skewness and kurtosis.

With these definitions the transport flux fraction, which is shown in Fig. 7.8, can be analyzed. It is found that the large transport events cause only 1 % of the observed transport, while 24 % are related to medium size transport events. The majority of transport is produced by small transport events. They contribute 84 % to transport. The remaining 9 % are directed inwards.

To summarize, the observed transport T_{ref} is dominated by small transport events. The spectrum and the PDFs indicate that the transport is not dominated by a single-mode.

7.2.2 Transport with driver signal

To study the influence of the exciter signal on transport, co-rotating driver signals of $m_{ex} = 1 \dots 3$ are applied to the system. For each mode number the transport is recorded with triple probes as function of radius and driver frequency. The frequency step width is 200 Hz. For $m_{ex} = 1$ the frequency is varied from 10 to 14 kHz, for $m_{ex} = 2$ from 18 to 22 kHz and for $m_{ex} = 3$ from 24 to 28 kHz. Additionally, the transport of the undriven system is recorded at each radial position to correct slight plasma parameter drifts.

The results are shown in Fig. 7.9. The color plot Fig. 7.9 b depicts deviation of the average transport with driver signal from the average transport without driver signal as function of radius and driver frequency. The plot is normalized to the average transport of the undriven system. In other words, the yellow regions mark a transport enhancement of 100 %, while blue indicates transport reduction. The power spectrum of the density fluctuations of the undriven system at $r = 25$ mm is plotted for orientation (Fig. 7.9 a). The plots Fig. 7.9 c-e show the average transport as function of radius for the driven and undriven system for the different driver signals ((c) $m_{ex} = 1$, (d) $m_{ex} = 2$ and (e) $m_{ex} = 3$). The corresponding driver frequencies are marked by dashed lines in Fig. 7.9 a.

As for the driven single-mode state, average transport is affected by the driver signal. However, depending on the exciter mode m_{ex} completely different behavior is observed. For $m_{ex} = 1$ the transport is nearly doubled for positions close to the center. This relative enhancement decreases with radius and finally turns into a transport reduction of 30 % at $r = 40$ mm. The maximum enhancement is observed for $f_{ex} = f_1$. This corresponds to the local maximum observed in the power spectrum of the undriven system. According to chapter 6, a phase measurement reveals zero phase shift of $m = 1$ drift mode and exciter signal for this exciter frequency. The more f_{ex} and f_1 differ, the lower is the observed transport enhancement close to the center. At the same time transport increases at $r > 40$ mm, i.e. close to the position of the exciter plates.

For $m_{ex} = 2$ the radial distribution of transport reduction and enhancement is different. For $f_{ex} \approx f_2$ a slight transport enhancement is found for $r \approx 30$ mm. Closer to the center of the plasma column and to the exciter plates the transport is reduced at the same time. Compared to the transport enhancement observed for $m_{ex} = 1$, the region of transport enhancement is much smaller and the enhancement is only of the order of

20-30 %. The average transport is reduced at most radial positions, if the frequencies f_{ex} and f_2 are different. Only close to the position of the exciter plates transport enhancement is observed. Although the local maximum of the density power spectrum is not observed at f_2 , a phase measurement reveals zero phase shift of $m = 2$ drift mode and exciter signal. This confirms the observation presented in chapter 6, that for a multi-mode state the best synchronization for a $m = 2$ drift mode is not always observed at those frequencies, where the density power spectrum of the undriven system has a local maximum.

For $m_{ex} = 3$ a transport enhancement is not observed. At all radial positions and for all exciter frequencies the transport is reduced by about 30 %.

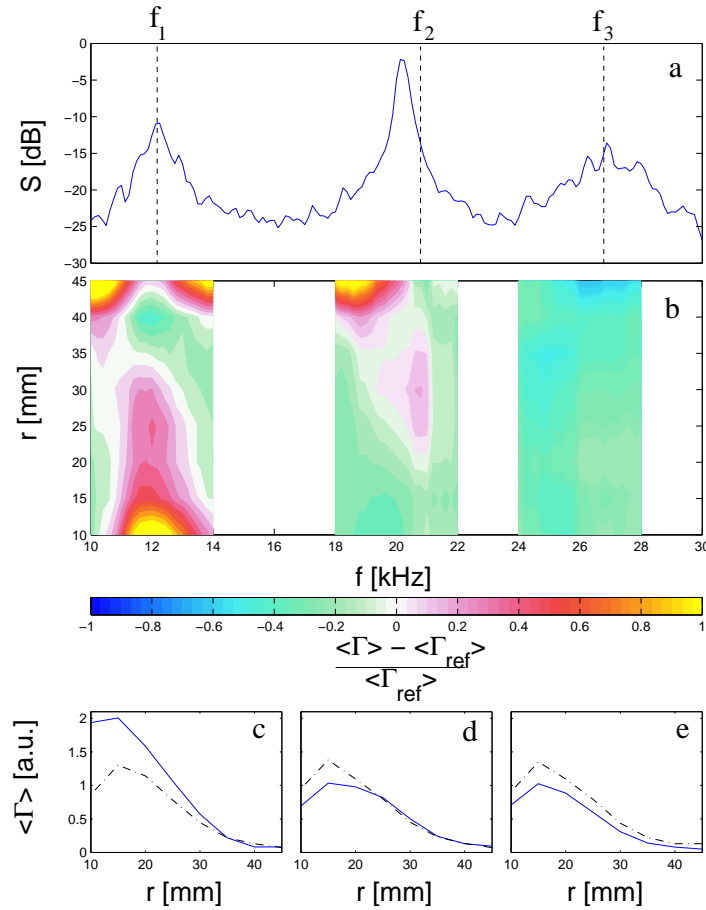


Figure 7.9: (a) Power spectrum of the density fluctuations of the undriven system at $r = 25$ mm. (b) Deviation of the average transport with exciter signal from the average transport without exciter signal as function of radius and exciter frequency. The three colored regions are related to $m_{ex} = 1 \dots 3$ exciter signals (mode number increases with frequency). Average transport as function of radius for $m_{ex} = 1$ (c), $m_{ex} = 2$ (d) and $m_{ex} = 3$ (e). The corresponding frequencies are marked by dashed lines in (a). The dashed dotted line shows the average transport without exciter signal.

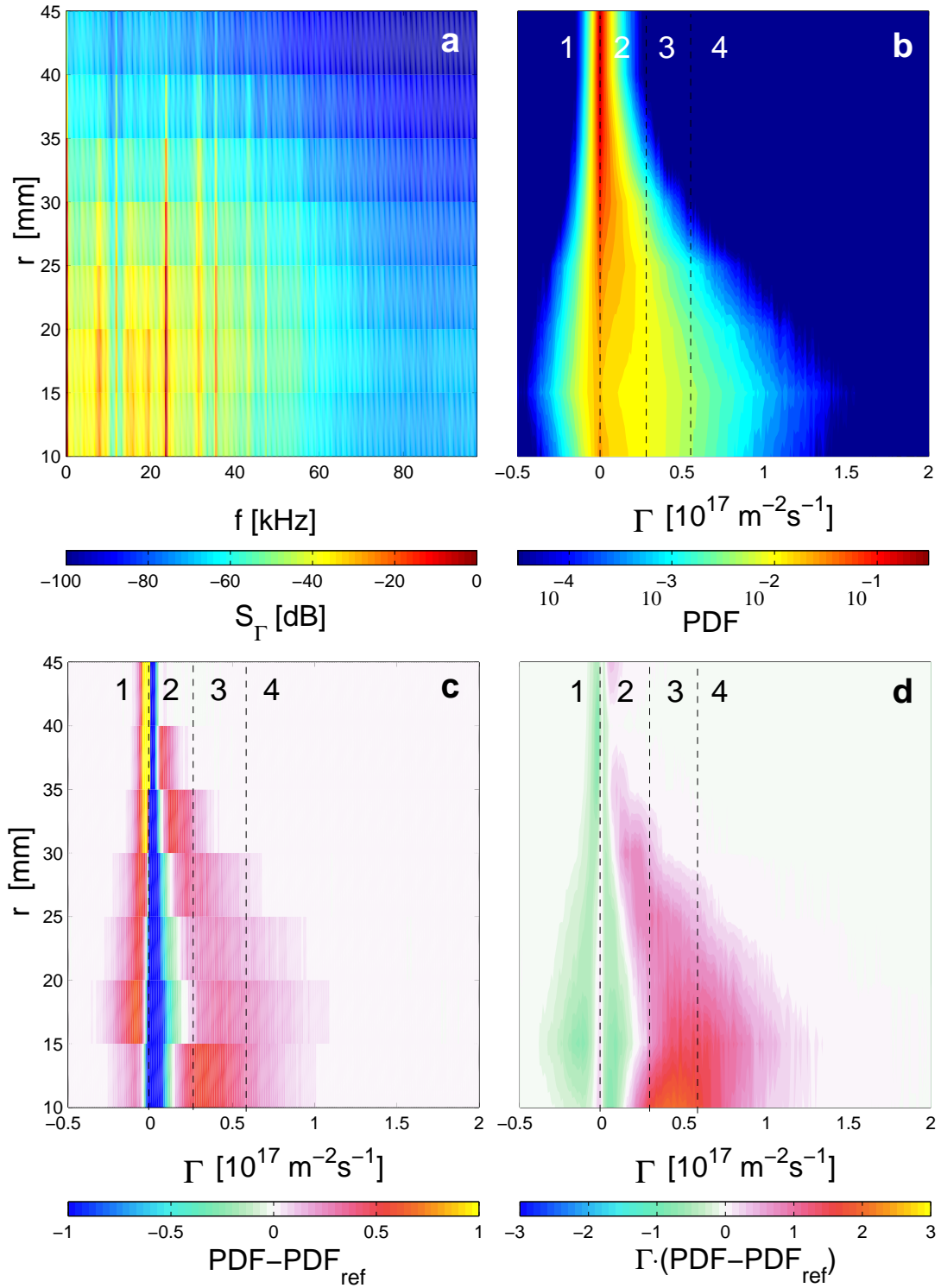


Figure 7.10: Analysis for co-rotating $m_{ex} = 1$ exciter signal with frequency $f_{ex} = f_1$. (a) Color plot of power spectrum S_Γ as function of radius. (b) PDF of Γ as function of radius. The numbers are related to the transport classification. (c) Color plot to visualize change of PDF. (d) Color plot of change of transport flux fraction.

To relate these reductions and enhancements in average transport to the temporal transport evolution, the Figs. 7.10-7.12 show the spectral and statistical properties of Γ for $f_{ex} = f_1 \dots f_3$ at $r = 25$ mm. Each figure uses the same scalings to assure comparability.

Fig. 7.10 a shows the power spectrum of Γ for $\mathbf{m}_{ex} = \mathbf{1}$ and $\mathbf{f}_{ex} = \mathbf{f}_1$. Compared to the undriven system (Fig. 7.8 a) a new, pronounced spectral component is observed at $2f_{ex}$. The peak of the $m = 2$ mode is almost completely suppressed. Nevertheless, the radial extent of the broadband background level has increased, while its amplitude has not changed. These spectral properties of Γ are in agreement with the observations made in chapter 6. There, the co-rotating $m_{ex} = 1$ exciter signal was found to synchronize the $m = 1$ drift mode and to suppress the other drift modes. While the $m = 3$ mode disappeared from the spectrum, the peak of the $m = 2$ mode was still observed. Therefore, the power spectrum of Γ qualitatively reflects the previous findings. Related to the enhancement of the $m = 1$ mode is a significant change of the PDF of Γ (Figs. 7.10 b and c). The number of medium and large transport events has increased, while the number of small events has decreased. The resulting change in flux fraction is depicted in Fig. 7.10 d. At a radius of e.g. $r = 25$ mm the transport is enhanced by 35 % (see Fig. 7.9 b). This enhancement is related to the increased number of medium and large size transport events. The decrease of small size events and inward transport events nearly cancel. For positions close to the plasma column center this increase in transport flux fraction of medium and large transport events becomes more and more dramatic. Note, that this radial dependency shows some similarity with the radial mode structure of the $m = 1$ drift mode. In chapter 6 the density fluctuation amplitude and the coherent fluctuation fraction were found to decrease slightly with radius.

These findings differ significantly for $\mathbf{m}_{ex} = \mathbf{2}$ and $\mathbf{f}_{ex} = \mathbf{f}_2$. The power spectrum of Γ is shown in Fig. 7.11 a. Pronounced peaks are only observed for f_2 and its higher harmonics. The peaks for the other drift modes are completely suppressed. Compared to the undriven state the broadband background level is suppressed as well. The spectrum is almost comparable with the spectrum of the single-mode state (see Fig. 7.1). The peak at $2f_{ex}$ is clearly dominating due to its almost 40 dB higher amplitude. Compared to the $m_{ex} = 1$ exciter signal, the maximum amplitude is located at intermediate radii and not close to the center of the plasma column. This finding is supported by the PDF of Γ . The PDF is broadest for intermediate radial positions. Compared to the PDF of Γ_{ref} an increase of small and inward transport events is observed. The medium and large events are suppressed. The change in transport flux fraction (Fig. 7.11 d) shows that the suppression of medium and large transport events gives a significant transport reduction, while the increased number of small transport events enhances transport. For small radii the transport reduction is dominating, but with increasing radius the transport enhancement increases rapidly and dominates for $r \approx 30$ mm. In chapter 2 and 6 it was shown that the mode structure of an $m = 2$ drift mode has its maximum fluctuation amplitude at larger radii than the $m = 1$. Combining these findings and the observed transport properties, it seems that reduction/enhancement of average transport and radial mode structure are related.

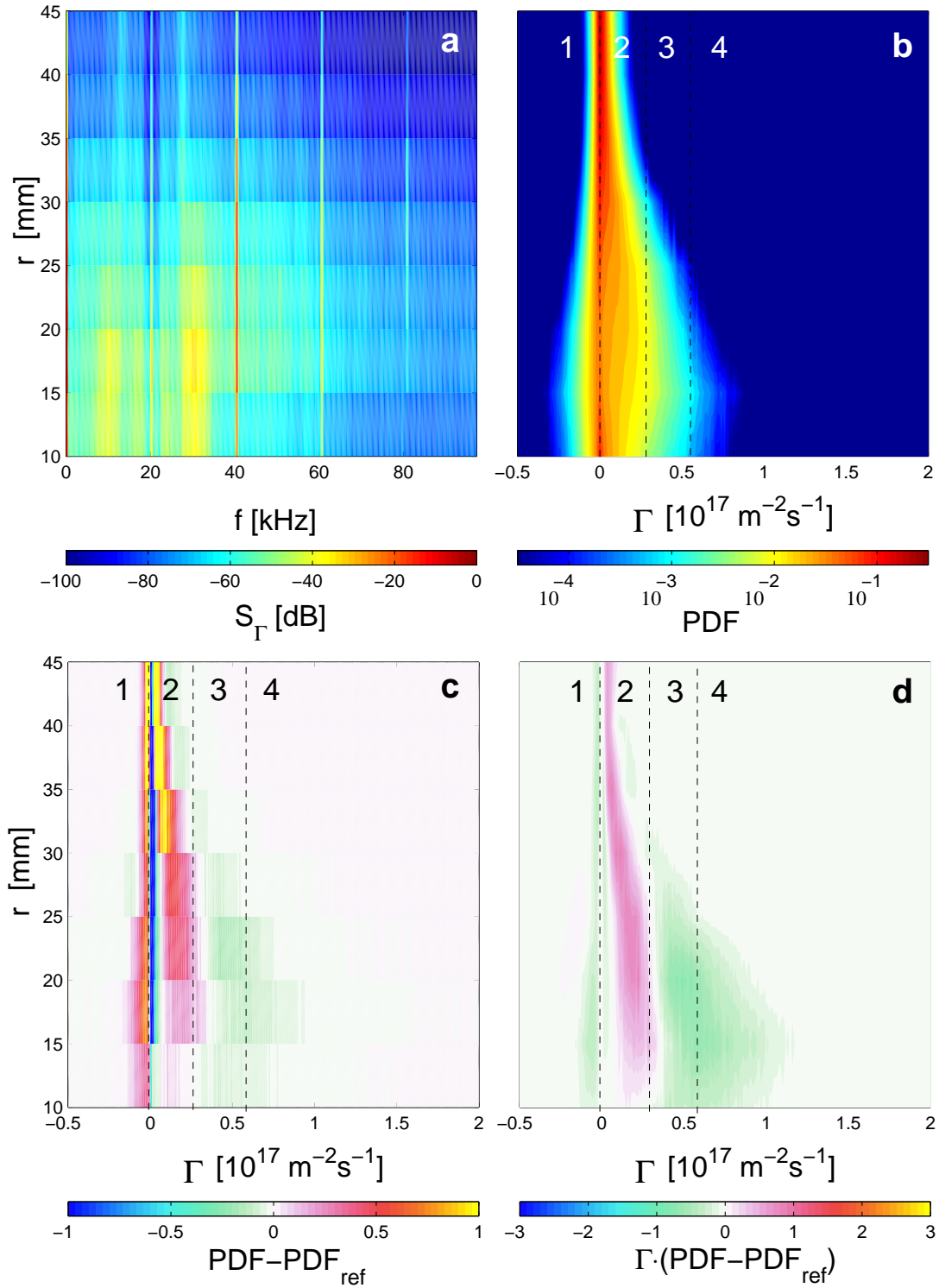


Figure 7.11: Analysis for co-rotating $m_{ex} = 2$ exciter signal with frequency $f_{ex} = f_2$. (a) Color plot of power spectrum S_Γ as function of radius. (b) PDF of Γ as function of radius. The numbers are related to the transport classification. (c) Color plot to visualize change of PDF. (d) Color plot of change of transport flux fraction.

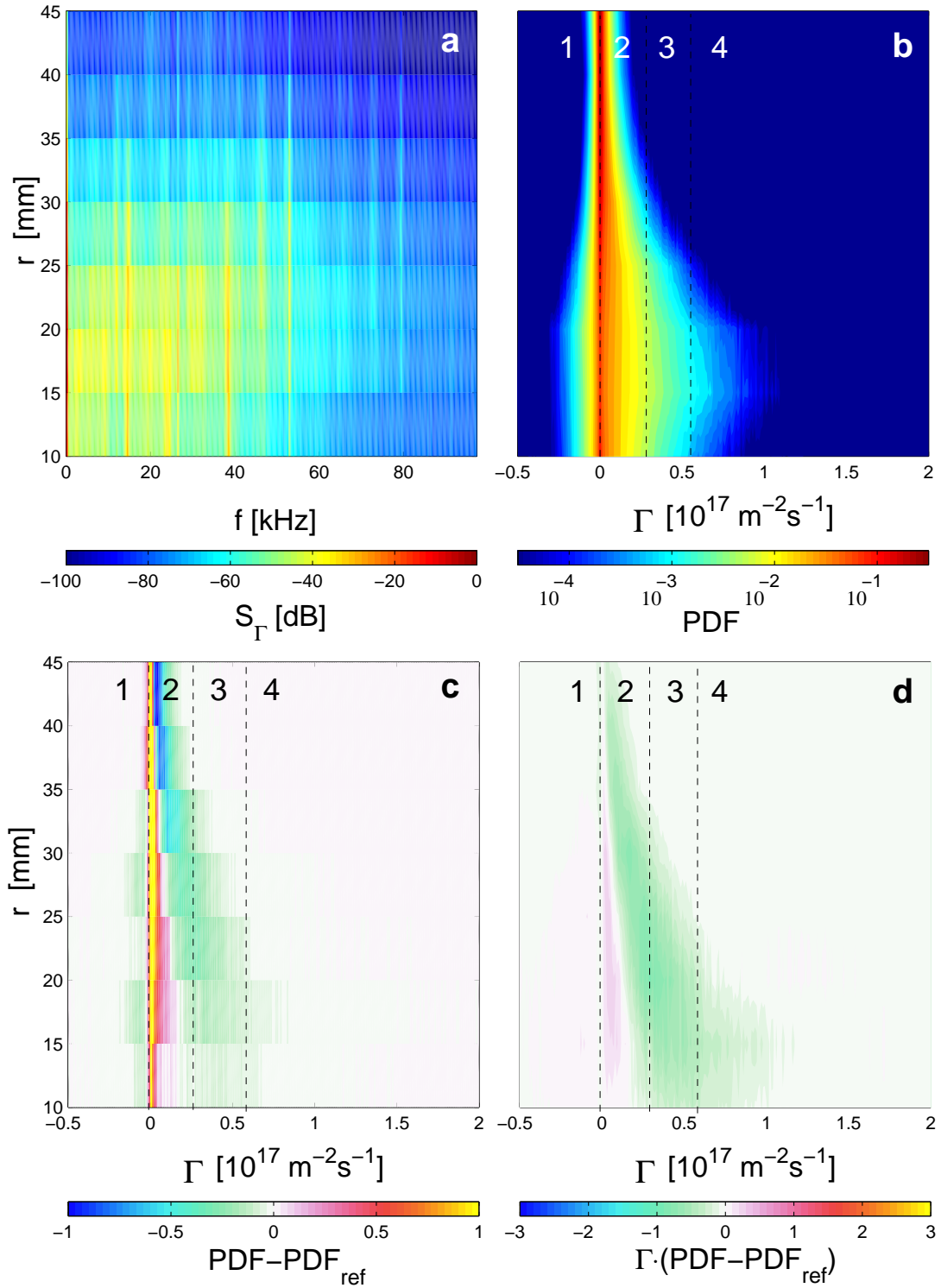


Figure 7.12: Analysis for co-rotating $m_{ex} = 3$ exciter signal with frequency $f_{ex} = f_3$. (a) Color plot of power spectrum S_Γ as function of radius. (b) PDF of Γ as function of radius. The numbers are related to the transport classification. (c) Color plot to visualize change of PDF. (d) Color plot of change of transport flux fraction.

No dominant peaks are observed in the transport power spectrum for $\mathbf{m}_{ex} = \mathbf{3}$ and $\mathbf{f}_{ex} = \mathbf{f}_3$ (Fig. 7.12 a). Compared to the undriven system, this means that the peak related to the $m = 2$ drift mode is suppressed. The PDF of Γ is reduced for medium and large transport events, while the number of small transport events is increased (Fig. 7.12 b and c). The result is a significant reduction of transport, due to the reduction of medium and large transport events. This reduction is only slightly attenuated by the increase of small transport events. That for the $m_{ex} = 3$ exciter mode a harmonic transport signal is not observed, is in agreement with the observations made in chapter 6. There, it was found that the $m = 3$ drift mode was not enhanced by the matching exciter signal. Rather the $m = 1$ mode was synchronized super-harmonically, while the $m = 2$ drift mode was suppressed. The enhancement of the $m = 1$ drift mode was much weaker than for a $m_{ex} = 1$ exciter mode. These findings agree with the observation from the power spectrum of Γ (Fig. 7.12 a).

To summarize, the changes in average transport are related to changes in spectral and statistical properties of Γ . Their radial structure and the observations made for synchronization in chapter 6 raises the suspect, that the radial mode structure of the different mode numbers is responsible for the observed qualitative change in transport for different exciter modes.

7.2.3 Spectrally resolved transport measurements

To investigate the influence of suppression and enhancement of the different drift modes on transport, it is essential to measure the spectrally resolved transport. For this purpose the obtained data are analyzed with the technique described in chapter 4. The transport related to a specific mode number is estimated from

$$\langle \Gamma(f_i) \rangle = \int_{f_i - \Delta}^{f_i + \Delta} \Gamma(f) df. \quad (7.1)$$

with $\Delta = 2$ kHz and $i = 1 \dots 3$ denoting the drift mode number. f_i are the frequencies obtained in the previous section. For each exciter mode the spectrally resolved transport is calculated for the $m = 1 \dots 3$ drift modes. The results are depicted in Figs. 7.13 - 7.15. For each drift mode its relative contribution to transport is shown in the plot (a-c). The plots (d-f) show the relative change in transport with respect to the undriven system.

For a $m_{ex} = 1$ exciter signal, the transport is clearly dominated by the $m = 1$ drift mode, if $f_{ex} \approx f_1$. Close to the center of the plasma column about 80-90% of the observed transport are related to the $m = 1$ mode (Fig. 7.13 a). The contribution to transport of the $m = 2$ mode decreases with f_{ex} approaching f_1 (Fig. 7.13 b). The contribution of the $m = 3$ mode is negligible for all frequencies f_{ex} . The enhancement and suppression of the different modes can be seen in Figs 7.13 d-f. The $m = 1$ mode is significantly enhanced by the $m_{ex} = 1$ exciter signal. The enhancement decreases with radius. At the same time the $m = 2$ drift mode is suppressed. The suppression is strongest for $r \approx 25$ mm. For the $m = 3$ mode the slight suppression is strongest

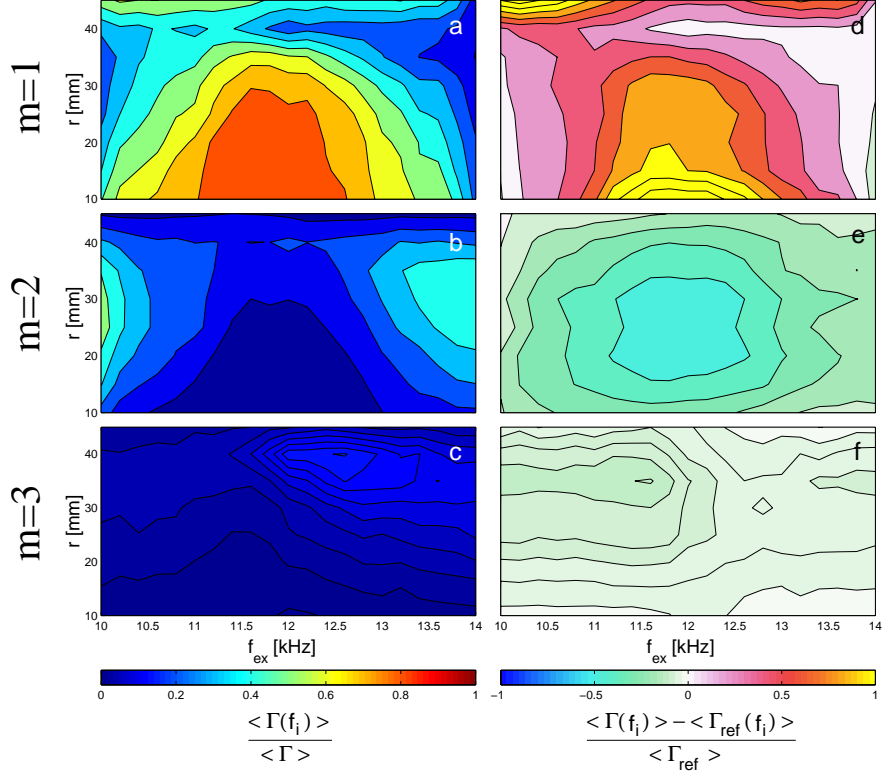


Figure 7.13: Spectrally resolved transport measurements for a $m_{ex} = 1$ driver signal. Plots (a-c) show the transport calculated by Eq. 7.1. The related drift mode number is attached to the left. The plots are normalized to the average transport. Plots (d-f) show the relative change in transport with respect to the undriven system for the different mode numbers.

for $r \approx 35$ mm. A comparison with the observed changes in average transport (see Fig. 7.9) yields that these changes are almost entirely caused by the enhancement and suppression of the drift modes. This implies that the change of the transport related to stochastic fluctuations is not significant.

For a $m_{ex} = 2$ exciter signal, the transport is dominated by the $m = 2$ drift mode for $f_{ex} \approx f_2$ (Fig. 7.14 b). The radial position of the transport maximum is observed at $r \approx 30$ mm. Here, the $m = 2$ drift mode causes about 90 % of the observed transport. The non-matching mode numbers are suppressed (Fig. 7.14 d and f). Their contribution to transport can be neglected (Fig. 7.14 a and c). Therefore the observations for $m_{ex} = 1$ and $m_{ex} = 2$ are qualitatively the same. Both exciter modes enhance the matching drift mode and suppress the other. The remaining drift mode causes almost the entire observed transport. The radial position of transport enhancement and reduction is shifted outwards with increasing mode number.

A slightly different observation is made for a $m_{ex} = 3$ exciter signal. Although a transport enhancement is found for the $m = 3$ drift mode (Fig. 7.15 c), the transport is

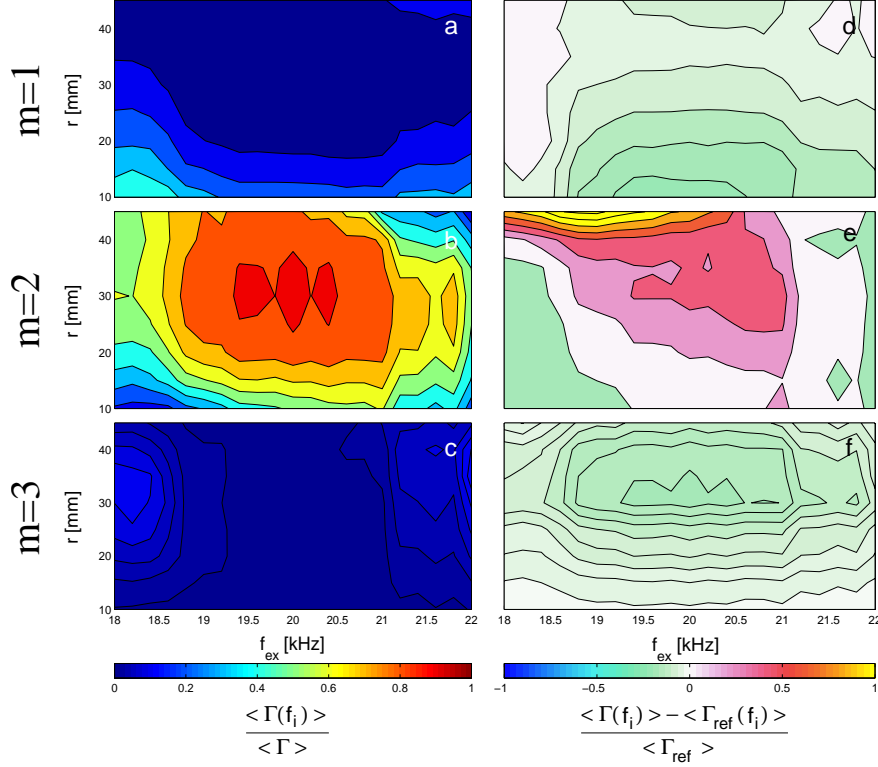


Figure 7.14: Spectrally resolved transport measurements for a $m_{ex} = 2$ driver signal. The arrangement and notations of the plots are identical with those in Fig. 7.13

enhanced for the $m = 1$ drift mode as well (Fig. 7.15 a), but compared to Fig. 7.13a the radial structure is different. The enhancement is very localized ($r \leq 20$ mm) (Fig. 7.15 d). For $r > 25$ mm, transport reduction is found, but for these positions the transport of the $m = 3$ drift mode is enhanced. The $m = 2$ drift mode is suppressed and their contribution to transport can be neglected (Fig. 7.15 b and e). The transport reduction due to the suppression of the $m = 2$ mode is of the order of 50 %, while the enhancement due to $m = 1$ and $m = 3$ are only about 20 %. Therefore, the observed transport reduction (Fig. 7.9 b) is related to the efficient suppression of the $m = 2$ drift mode.

These results show that the transport suppression and enhancement is clearly related to the suppression and enhancement of the different drift modes. Further, the radial position of maximum transport variation is moving radially outwards with increasing drift mode number. This is in agreement with the previous findings that the position of maximum fluctuation amplitude is shifting outwards with increasing mode number, i.e. a suppression and enhancement of a drift mode will enhance or reduce the radial fluctuation profile according to the mode number. Therefore, a $m_{ex} = 1$ driver signal will increase the fluctuations closer to the center of the plasma column, while a $m_{ex} = 3$ driver signal will increase the fluctuations further outside. The overall change in transport is related to the balance of the individual transport changes.

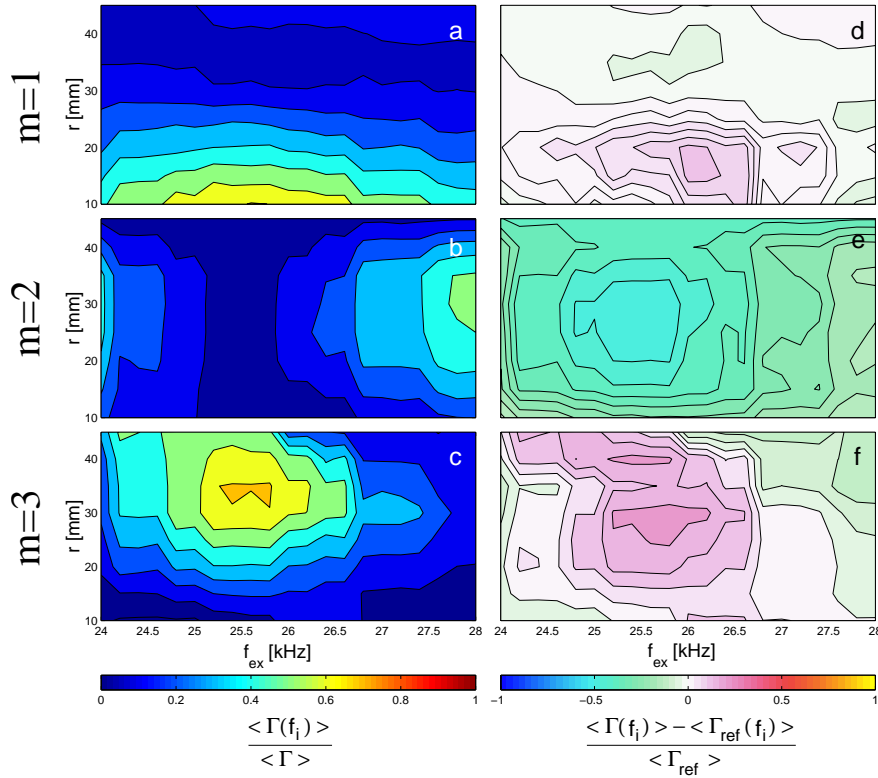


Figure 7.15: Spectrally resolved transport measurements for a $m_{ex} = 3$ driver signal. The arrangement and notations of the plots are identical with those in Fig. 7.13

7.3 Synopsis

To analyze the transport properties of the driven drift wave system statistical and spatio-temporally resolved measurement techniques have been used. The obtained results of the different techniques are basically identical. An additional important result is that the spatial resolution is essential for a detailed interpretation of the measurements.

The presented investigations on transport concentrated on two initial states, the single-mode and multi-mode state, with different drift wave dynamics. For both states transport is found to be dominated by coherent structures, i.e. drift modes. This is in agreement with the results presented in chapter 6, where the fluctuations of density and potential were found to be dominated by the coherent fraction.

For the driven single-mode state a significant transport reduction is found for matching spatio-temporal structures of driver signal and drift wave. Although an influence of the driver signal on the phase shift between density and potential fluctuations can not be excluded, the reduced fluctuations amplitude of the azimuthal electric field can explain the observed transport reduction. This additionally supports the picture, that the azimuthal electric field plays a substantial role for the synchronization process (see chapter 6).

Furthermore, the observed transport modulation for periodic pulling is shown to be related to an amplitude modulation of density and azimuthal electric field. Generally a phase modulation cannot be excluded, but the analysis reveals that the amplitude modulation seems to dominate.

If a system with more than a single drift mode is driven, a more complicated situation is found. The radially resolved and mode selective measurements of transport show that the observed changes of average transport depend on the mode number of the driver signal. The transport measurements support the findings from chapter 6, where the fluctuation amplitude of the resonantly driven mode was found to be enhanced, while the other modes are suppressed. Hence, the resonantly driven mode dominates the observed transport, while the other modes contribute less to transport than for the undriven state. Whether the average transport is enhanced or suppressed overall, is determined by the sum of the transport enhancements and suppressions of the individual drift modes. Due to the Gaussian density profile and the size of the different mode structures a $m = 1$ mode with its larger size and a more centrally peaked position can transport dense plasma from the center very efficiently far outwards. For a $m = 3$ mode the smaller size limits the transport distance. Its remote position from the plasma center additionally leads to less transport compared to a $m = 1$ mode. Therefore, a suppression of the more central, large scale modes yields an overall transport reduction while the transport is enhanced if such a mode is driven.

Chapter 8

Summary and outlook

In this thesis, extensive experimental investigations have been presented which were aimed to study the influence of spatio-temporal driver signals on drift waves. Besides a thorough characterization of the discharge, its equilibrium profiles and its fluctuations, the investigations were focused on the interaction of spatio-temporal driver signals and drift waves. For this purpose two different plasma states have been used, first a single-mode state to study the spatio-temporal dynamics of a driven drift wave and to gain insight into the underlying mechanism, and second the multi-mode state to extend the validity of the observed phenomena to more complex dynamical situations and to link them with observations made for weak turbulence [81]. The following paragraphs summarize the main results and point out future prospects.

Undriven system: Spatially three dimensional measurements of the plasma equilibrium profiles have been performed which allow for a clear identification of the observed fluctuations as drift waves. The measured propagation velocity of the drift waves was found to be determined by the equilibrium profiles of plasma potential and density, i.e. $\mathbf{v}_{dw} \approx \mathbf{v}_{E \times B} + (1 + Q\rho^2)^{-1} \mathbf{v}^*$. The theoretically predicted radial mode structure and its dependence on mode number were clearly observed by independent measurements and analysis techniques. Furthermore, all observations are in concord with previous findings [115, 116]. Therefore, the well described plasma conditions in KIWI provide an excellent basis for a detailed comparison of the dynamics of driven and undriven drift waves.

Driven single-mode state: The application of spatio-temporal driver signals with various spatial periodicities and propagation directions revealed that only for resonant spatio-temporal driver signals a significant influence on drift wave dynamics is observed. In this case the drift waves are found to be entrained by the driver signal. The synchronization width was found to be a reliable indicator to quantify the influence of the driver signal on the drift wave dynamics. Besides complete synchronization the driven system shows other nonlinear processes like periodic pulling and quasi-periodicity. Amplitude and phase measurements showed that the temporal dynamics

of driven drift waves are van der Pol-like. This finding is in accordance with many observations made for other driven systems. A novel finding is that the observed spatial dynamics consist of a modulation of propagation velocity which cause spatial stretching and compression. The preferred phase shift of driver signal and drift wave is found just opposite to what one would expect from energy arguments. Indeed, the azimuthal electric field is proposed to influence the drift wave propagation in such a way that the observed zero phase shift of drift wave and driver signal is the favored position for synchronization. Further, the measurements show impressively that a detailed understanding of the observed nonlinear dynamics is only achieved by spatio-temporal measurement techniques which reflect the spatio-temporal character of the drift wave. Especially processes like periodic pulling, which are not strictly periodic, demand for spatio-temporally resolved measurements.

Driven multi-mode state: If more than a single drift mode is present, the external driver signal suppresses the non-resonant modes in the system, while the resonant drift mode is enhanced. The efficiency of the driving process increases with the growth rate of the driven mode, i.e. the most unstable mode in the system is driven most efficiently. The enhancement of fluctuation amplitude by the driver signal is found to depend on the mode number of the driver signal. The radial outward shift of the position of maximum fluctuation amplitude with increasing mode number shows that the different drift modes are driven resonantly according to their specific radial mode structure.

Influence on transport: The spatio-temporal changes in drift wave dynamics were found to significantly alter the related fluctuation-induced transport. For the single-mode state, a significant transport reduction at all radial positions has been observed for a resonant spatio-temporal driver signal. Although an influence of the driver signal on the phase shift between density and potential fluctuations cannot be excluded experimentally, the observed reduction of the average azimuthal electric field fluctuation amplitude explains the observed transport reduction. For a multi-mode state, the influence of driver signals is found to be determined by the radial mode structure of the driven mode. Generally, the transport related to the driven mode is enhanced. The other modes are suppressed, if the driver signal is not superharmonic. The relative enhancement and suppression of transport related to single modes is found to depend on radius and to reflect directly their radial mode structure. The total fluctuation-induced transport is determined by the sum of the individual modes, i.e. the change of transport depends on the increase and decrease of transport of each mode. With increasing mode number it is observed that the transport related to the driven mode decreases. This reduction is related to the decreasing radial extent and the radial outward shift of the position of maximum fluctuation amplitude of the drift modes with increasing mode number. Therefore, the observed transport changes can be explained by the mode-selective influence of the driver signal on the undisturbed dynamic state and by the inherent properties of individual drift modes.

To conclude, a detailed spatio-temporal description of a driven drift wave system has been given for the first time. It shows that the spatial dimension is essential for a deeper understanding of the involved dynamical processes. It is suggested that the azimuthal electric field plays an essential role for the understanding of the synchronization process. In combination with prior findings for meta-stable guided ionization waves [78, 79], these measurements give strong indication that altered spatial dynamics are typical of driven wave-like phenomena. The combination of known techniques to investigate fluctuation-induced transport with concepts of nonlinear dynamics has shown that the observed transport is caused by the drift modes and that its spatio-temporal structure is directly linked with the spatio-temporal structure of the drift modes. Further it was shown that the nexus of nonlinear dynamics of driven drift waves and anomalous transport offers new possibilities to identify single transport processes and their importance and helps to disentangle the complexity of transport dynamics.

Therefore, one major benefit of synchronization experiments is the possibility to learn details about fundamental dynamical processes and their influence on transport. Its use as diagnostic tool has been successfully demonstrated by this work. Further refinements of this method with probe arrays will even allow to determine the temporal evolution of full poloidal cross-sections. This will offer almost perfect conditions for detailed comparisons of 3D simulations and experimental observations. Hence, the application of spatio-temporal driver signals to confined plasmas, e.g. with magnetic geometry with higher relevance for fusion, is a promising task. It will give further insight into the dynamics of drift wave turbulence and the related fluctuation-induced transport, which can be used to improve confinement.

Bibliography

- [1] A. J. Wootton, B. A. Carreras, H. Matsumoto, K. McGuire, W. A. Peebles, Ch. P. Ritz, P. W. Terry, and S. J. Zweben. Fluctuations and anomalous transport in tokamaks. *Phys. Fluids B*, 2(12):2879–2903, 1990.
- [2] A. Rudyi. Untersuchung transportrelevanter fluktuationen in der randschicht von asdex. Technical Report III/160, Max-Planck-Institut für Plasmaphysik, Garching, 1990.
- [3] F. Wagner and U. Stroth. Transport in toroidal devices - the experimentalist's view. *Plasma Phys. Controlled Fusion*, 35:1321–1371, 1993.
- [4] H. W. Hendel, T. K. Chu, and P. A. Politzer. Collisional drift waves—identification, stabilization, and enhanced plasma transport. *Phys. Fluids*, 11:2426–2439, 1968.
- [5] N. D'Angelo and N. Rynn. Diffusion of a cold cesium plasma across a magnetic field. *Phys. Fluids*, 4:275–276, 1961.
- [6] N. D'Angelo. Low-frequency oscillations in cesium thermionic converters. *Phys. Fluids*, 4:1054–1055, 1961.
- [7] N. D'Angelo and N. Rynn. Diffusion and recombination of a highly ionized cold plasma in a magnetic field. *Phys. Fluids*, 4:1303–1306, 1961.
- [8] S. S. Moiseev and R. Z. Sagdeev. On the bohm diffusion coefficient. *Sov. Phys. - JETP*, 17:515–517, 1963.
- [9] J. D. Jukes. Micro-instabilities in magnetically confined, inhomogeneous plasma. *Phys. Fluids*, 7:1468–1474, 1964.
- [10] H. Lashinsky. Universal instability in a fully ionized inhomogeneous plasma. *Phys. Rev. Lett.*, 12:121–123, 1964.
- [11] F. F. Chen. Normal modes for electrostatic ion waves in an inhomogeneous plasma. *Phys. Fluids*, 7:949–955, 1964.

- [12] F. F. Chen. Effect of sheaths on drift instabilities in thermionic plasmas. *Phys. Fluids*, 8:752–754, 1965.
- [13] F. F. Chen. Resistive overstabilities and anomalous “diffusion”. *Phys. Fluids*, 8:912–919, 1965.
- [14] F. F. Chen. “Universal” overstability of a resistive, inhomogeneous plasma. *Phys. Fluids*, 8:1323–1333, 1965.
- [15] F. F. Chen. Nonlocal drift modes in cylindrical geometry. *Phys. Fluids*, 10:1647–1651, 1967.
- [16] T. K. Chu, B. Coppi, H. W. Hendel, and F. W. Perkins. Drift instabilities in a uniformly rotating plasma cylinder. *Phys. Fluids*, 12(1):203–208, 1969.
- [17] R. F. Ellis and E. Marden-Marshall. Comparison of local and nonlocal theories of the collisional drift instability. *Phys. Fluids*, 22:2137–2139, 1979.
- [18] R. F. Ellis, E. Marden-Marshall, and R. Majeski. Collisional drift instability of a weakly ionized argon plasma. *Plasma Physics*, 22:113–132, 1980.
- [19] E. Marden-Marshall, R. F. Ellis, and J. E. Walsh. Collisional drift instability in a variable radial electric field. *Plasma Phys. Controlled Fusion*, 28(9B):1461–1482, 1986.
- [20] A. Hasegawa and K. Mima. Pseudo-three-dimensional turbulence in magnetized nonuniform plasma. *Phys. Fluids*, 21(1):87–92, 1978.
- [21] A. Hasegawa and M. Wakatani. Plasma edge turbulence. *Phys. Rev. Lett.*, 50:682–686, 1983.
- [22] W. Horton. Nonlinear drift waves and transport in magnetized plasmas. *Phys. Rep.*, 192(1-3):1–177, 1990.
- [23] W. Horton. Drift waves and transport. *Rev. Mod. Phys.*, 71(3):735–778, 1999.
- [24] B. Scott. Low frequency fluid drift turbulence in magnetised plasmas. Habilitationsschrift, Heinrich-Heine-Universität, Düsseldorf, 2000.
- [25] P. N. Guzdar. Shear-flow generation by drift/rossby waves. *Phys. Plasmas*, 2(11):4174–4176, 1995.
- [26] G. Manfredi, C. M. Roach, and R. O. Dendy. Zonal flow and streamer generation in drift turbulence. *Plasma Phys. Controlled Fusion*, 43:825–837, 2001.
- [27] A. E. Koniges, J. A. Crotinger, and P. H. Diamond. Structure formation and transport in dissipative drift-wave turbulence. *Plasma Phys. Controlled Fusion*, 4(9):2785–2793, Phys. Fluids B.

- [28] J. A. Krommes, G. Hu and J. C. Bowman. Statistical theory of resistive drift-wave turbulence and transport. *Phys. Plasmas*, 4(6):2116–2133, 1997.
- [29] K. W. Gentle. Diagnostics for magnetically confined high-temperature plasmas. *Rev. Mod. Phys.*, 65(4):809–835, 1995.
- [30] T. Huld, A. H. Nielsen, H. L. Pécseli, and J. J. Rasmussen. Coherent structures in two-dimensional plasma turbulence. *Phys. Fluids B*, 3(7):1609–1625, 1991.
- [31] K. Rypdal, H. Fredriksen, J. V. Paulsen, and O. M. Olsen. Coherent structures in the turbulent equilibrium of the simple magnetized torus. *Physica Scripta*, T63:167–173, 1995.
- [32] O. Grulke, T. Klinger, and A. Piel. Experimental study of the dynamics of conditionally averaged structures in weakly developed electrostatic turbulence. *Phys. Plasmas*, 6(3):788–796, 1999.
- [33] O. Grulke, T. Klinger, M. Endler, A. Piel, and the W7-AS team. Analysis of large-scale fluctuation structures in the scrape-off layer of the Wendelstein 7-AS stellarator. submitted to *Phys. Plasmas*, 2001.
- [34] T. Klinger, A. Latten, A. Piel, G. Bonhomme, T. Pierre, and T. Dudok de Wit. The route to drift wave chaos and turbulence in a bounded low- β plasma experiment. *Phys. Rev. Lett.*, 79:3913–3916, 1997.
- [35] A. Latten, T. Klinger, A. Piel, and Th. Pierre. A probe array for the investigation of spatio-temporal structures in drift wave turbulence. *Rev. Sci. Instrum.*, 66(5):3254–3262, 1995.
- [36] A. Latten, T. Klinger, A. Piel, T. Pierre, and G. Bonhomme. Experimental investigation of fluctuation-induced radial transport due to drift wave turbulence. In S. Benkadda, F. Doveil, and Y. Elskens, editors, *Transport, Chaos and Plasma Physics 2*, pages 341–344. World Scientific, Singapore, 1996.
- [37] E. J. Powers. Spectral techniques for experimental investigation of plasma diffusion due to polychromatic fluctuations. *Nucl. Fusion*, 14:749, 1974.
- [38] A. Latten. *Multisondendiagnostik von Driftwellenturbulenz und anomalem Radialtransport in Laborplasmen*. PhD thesis, Christian-Albrechts-Universität Kiel, 1997.
- [39] K. I. Thomassen. Feedback stabilization in plasmas. *Nucl. Fusion*, 11:175–186, 1971.
- [40] V. V. Arsenin and V. A. Chuyanov. Suppression of plasma instabilities by feedback method. *Sov. Phys.-Usp.*, 20(9):736–762, 1977.

- [41] T. Uckan B. Richards, A. J. Wootton, B. A. Carreras, R. D. Bengtson, P Hurwitz, G. X. Li, A. K. Sen, , and J. Uglum. Modification of tokamak edge turbulence using feedback. *Phys. Plasmas*, 1(5):1606–1611, 1994.
- [42] A. K. Sen. Control and diagnostic uses of feedback. *Phys. Plasmas*, 7(5):1759–1766, 2000.
- [43] R. R. Weynants and G. Van Oost. Edge biasing in tokamaks. *Plasma Phys. Controlled Fusion*, 35:B177–B189, 1993.
- [44] P. W. Terry. Suppression of turbulence and transport by sheared flow. *Rev. Mod. Phys.*, 72(1):109–165, 2000.
- [45] F. Wagner, G. Becker, K. Behringer, D. Campbell, A. Eberhagen, W. Engelhardt, G. Fussmann, O. Gehre, J. Gernhardt, G. v. Gierke, G. Haas, M. Huang, F. Karger, M. Keilhacker, O. Klüber, M. Kornherr, K. Lackner, G. Lisitano, G. G. Lister, H. M. Mayer, D. Meisel, E. R. Müller, H. Murmann, H. Niedermeyer, W. Poschenrieder, H. Rapp, H. Röhr, F. Schneider, G. Siller, E. Speth, A. Stäbler, K. H. Steuer, G. Venus, O. Vollmer, and Z. Yü. Regime of improved confinement and high beta in neutral-beam-heated divertor discharges of the ASDEX tokamak. *Phys. Rev. Lett.*, 49(19):1408–1412, 1982.
- [46] F. Wagner, G. Fussmann, T. Grave, M. Keilhacker, M. Kornherr, K. Lackner, K. McCormick, E. R. Müller, A. Stäbler, G. Becker, K. Bernhardt, U. Ditte, A. Eberhagen, O. Gehre, J. Gernhardt, G. v. Gierke, E. Clock, O. Gruber, G. Haas, M. Heese, G. Janeschitz, F. Karger, S. Kissel, O. Klüber, G. Lisitano, H. M. Mayer, D. Meisel, V. Mertens, H. Murmann, W. Poschenrieder, H. Rapp, H. Röhr, F. Ryter, F. Schneider, G. Siller, P. Smeulders, F. Söldner, E. Speth, K.-H. Steuer, Z. Szymanski, and O. Vollmer. Development of an edge transport barrier at the H-mode transition of ASDEX. *Phys. Rev. Lett.*, 53(15):1453–1456, 1984.
- [47] R. J. Taylor, M. L. Brown, B. D. Fried, H. Grote, J. R. Liberati, G. J. Morales, P. Pribyl, D. Darrow, and M. Ono. H-Mode behavior induced by cross-field currents in a tokamak. *Phys. Rev. Lett.*, 63(21):2365–2368, 1989.
- [48] H. G. Schuster. *Handbook of Chaos Control*. VCH Verlagsgesellschaft, Weinheim, 1 edition, 1998.
- [49] T. Klinger. Control of plasma instabilities. Habilitationsschrift, Christian-Albrechts-Universität Kiel, 1998.
- [50] E. Gravier, X. Caron, G. Bonhomme, and Th. Pierre. Control of the chaotic regimes of nonlinear drift waves in a magnetized laboratory plasma. *Phys. Plasmas*, 6(5):1670–1673, 1999.

- [51] H. Lashinsky. Periodic pulling and the transition to turbulence in a system with discrete modes. In J. Fox, editor, *Symposium on Turbulence of Fluids and Plasmas*, pages 29–46. Polytechnic Institute of Brooklyn, Polytechnic Press, Brooklyn, New York, April 16-18 1968.
- [52] B. E. Keen. Interpretation of experiments on feedback control of a 'drift-type' instability. *Phys. Rev. Lett.*, 24(6):259–262, 1970.
- [53] C. Hayashi. *Nonlinear Oscillations in Physical Systems*. Princeton University Press, Princeton, New Jersey, 1964.
- [54] U. Parlitz and W. Lauterborn. Period-doubling cascades and devil's staircases of the driven van der Pol oscillator. *Phys. Rev. A*, 36(3):1428–1434, 1987.
- [55] R. Mettin, U. Parlitz, and W. Lauterborn. Bifurcation structure of the driven van der pol oscillator. *Int. J. Bifurcation and Chaos*, 3(6):1529–1555, 1993.
- [56] H. Klostermann. *Experimentelle Untersuchung von Oszillationen der Ionenschicht im Gitterbereich einer Doppelplasmaanlage*. PhD thesis, Christian-Albrechts-Universität zu Kiel, 1997.
- [57] T. Klinger, F. Greiner, A. Rohde, and A. Piel. Nonlinear dynamical behavior of thermionic filamentary low pressure discharges. Part II: experiment. *Phys. Plasmas*, 2:1822–1836, 1995.
- [58] H. Amemiya. Characteristics of the nonlinear suppression of ionization waves. *Plasma Phys.*, 25(7):735–754, 1983.
- [59] R. H. Abrams, E. J. Yadlowsky, and H. Lashinsky. Periodic pulling and turbulence in a bounded plasma. *Phys. Rev. Lett.*, 22(7):275–278, 1969.
- [60] M. E. Koepke, M. J. Alport, T. E. Sheridan, W. E. Amatucci, and J. J. Carroll III. Asymmetric spectral broadening of modulated electrostatic ion-cyclotron waves. *Geophys. Res. Lett.*, 21:1011–1014, 1994.
- [61] F. Greiner, T. Klinger, and A. Piel. Nonlinear dynamical behavior of thermionic filamentary low pressure discharges. Part I: simulation. *Phys. Plasmas*, 2:1810–1821, 1995.
- [62] A. Rohde. *Particle-in-cell Simulation von Oszillationen der Ionenschicht im Gitterbereich einer Doppelplasmaanlage*. PhD thesis, Christian-Albrechts-Universität Kiel, 1997.
- [63] K. Kurokawa. Injection locking of microwave solid-state oscillators. *Proc. IEEE*, 61(10):1386–1410, 1973.
- [64] N. N. Bogoljubow and J. A. Mitropolski. *Asymptotische Methoden in der Theorie der nichtlinearen Schwingungen*. Akademie-Verlag, Berlin, 1965.

- [65] M. E. Koepke and D. M. Hartley. Experimental verification of periodic pulling in a nonlinear electronic oscillator. *Phys. Rev. A*, 44(10):6877–6887, 1991.
- [66] T. E. Sheridan, M. E. Koepke, C. A. Selcher, and T. N. Good. Periodic pulling in a driven relaxation oscillator. *Proc. SPIE*, 2039:158–167, 1993.
- [67] H. Lashinsky, T. J. Rosenberg, and D. L. Detrick. Power line radiation: Possible evidence of van der Pol oscillations in the magnetosphere. *Geophys. Res. Lett.*, 7(10):837–840, 1980.
- [68] Y. Nakamura. Suppression of two-stream instability by beam-modulation. *J. Phys. Soc. Jpn*, 28(5):1315–1321, 1970.
- [69] Y. Nakamura. Suppression and excitation of electron oscillation in a beam-plasma system. *J. Phys. Soc. Jpn*, 31(1):273–279, 1971.
- [70] T. Tsuru. Nonlinear resonance phenomena of electron plasma oscillations by beam modulation. *J. Phys. Soc. Jpn*, 40(2):548–554, 1976.
- [71] B. E. Keen and W. H. W. Fletcher. Suppression and enhancement of an ion-sound instability by nonlinear resonance effects in a plasma. *Phys. Rev. Lett.*, 23(14):760–763, 1969.
- [72] B. E. Keen and W. H. W. Fletcher. Measurement of growth rate, non-linear saturation coefficients, and mode-mode coupling coefficients of a 'van der Pol' plasma instability. *J. Phys. D: Appl. Phys.*, 3:1868–1885, 1970.
- [73] K. Ohe and S. Takeda. Frequency spectrum and dispersion relation of moving striations in narrow discharge tubes. *Jpn. J. Appl. Phys.*, 11(6):1173–1180, 1972.
- [74] P. Michelsen, H. L. Pécseli, J. J. Rasmussen, and R. Schrittwieser. The current-driven, ion-acoustic instability in a collisionless plasma. *Plasma Phys.*, 21:61–73, 1979.
- [75] T. Gyergyek, M. Čerček, N. Jelić, and M. Stanojević. Mode suppression of a two-dimensional potential relaxation instability in a weakly magnetized discharge plasma. *Phys. Lett. A*, 177:54–60, 1993.
- [76] T. Klinger, F. Greiner, A. Rohde, A. Piel, and M. E. Koepke. Van der pol behavior of relaxation oscillations in a periodically driven thermionic discharge. *Phys. Rev. E*, 1995.
- [77] M. E. Koepke, T. Klinger, F. Seddighi, and A. Piel. Periodic nonlinear wave-wave interaction in a plasma discharge with no external oscillatory driving force. *Plasma Phys.*, 3(12):4421–4426, 1996.

- [78] M. E. Koepke, A. Dinklage, T. Klinger, and C. Wilke. Spatio-temporal signatures of periodic pulling during ionization-wave mode transitions. *Phys. Plasmas*, 8(4):1432–1436, 2001.
- [79] K.-D. Weltmann, M. E. Koepke, and C. A. Selcher. Spatiotemporal laser perturbation of competing ionization waves in a neon glow discharge. *Phys. Rev. E*, 62(2):2773–2781, 2000.
- [80] A. Latten. *Multisondendiagnostik von Driftwellenturbulenz und anomalem Radialtransport in Laborplasmen*. PhD thesis, Christian-Albrechts-Universität Kiel, 1997.
- [81] Ch. Schröder, T. Klinger, D. Block, G. Bonhomme A. Piel, and V. Naulin. Mode selective control of drift wave turbulence. *Phys. Rev. Lett.*, 86(25):5711–5714, 2001.
- [82] F. F. Cap. *Handbook on Plasma Instabilities*, volume 1. Academic, New York, 1976.
- [83] A. B. Mikhailovskii. *Theory of Plasma Instabilities*. Consultants Bureau, 1974.
- [84] B. Scott. Three-dimensional computation of collisional drift wave turbulence and transport in tokamak geometry. *Plasma Phys. Controlled Fusion*, 39(3):471–504, 1997.
- [85] D. R. Nicholson. *Introduction to Plasma Theory*. Wiley, New York, 1983.
- [86] B. Scott. Three-dimensional computation of drift alfvén turbulence. *Plasma Phys. Controlled Fusion*, 39(10):1635–1668, 1997.
- [87] U. Kauschke, G. Oelerich-Hill, and A. Piel. Experimental investigation of coherent drift waves at low magnetic fields. *Phys. Fluids B*, 2:38, 1989.
- [88] E. Marden-Marshall. *Drift Waves in a Nonuniformly Rotating Plasma Column*. PhD thesis, Dartmouth College Hanover (USA), 1980.
- [89] H. L. Pécseli. Electrostatic drift waves. Vorlesungsskript, University of Oslo.
- [90] A. Kendl, B. D. Scott, and H. Wobig. Transition from tokamak to stellarator turbulence. *Plasma Phys. Controlled Fusion*, 42(11):L23–L29, 2000.
- [91] P. H. Diamond and T. S. Hahm. On the dynamics of turbulent transport near marginal stability. *Phys. Plasmas*, 2(10):3640–3649, 1995.
- [92] B. A. Carreras, D. Newman, V. E. Lynch, and P. H. Diamond. A model realization of self-organized criticality for plasma confinement.

- [93] P. Beyer, Y. Sarazin, X. Garbet, P. Ghendrih, and S. Benkadda. 2d and 3d boundary turbulence studies. *Plasma Phys. Controlled Fusion*, 41:A757–A769, 1999.
- [94] M. Wakatani and A. Hasegawa. A collisional drift wave description of plasma edge turbulence. *Phys. Fluids*, (27):611–618, 1984.
- [95] B. van der Pol. *Phil. Mag.*, 43:700, 1922.
- [96] R. Adler. A study of locking phenomena in oscillators. *Proc. IRE*, 34:351–357, 1946.
- [97] T. Klinger. *Experimentelle Untersuchung der nichtlinearen Dynamik einer thermionischen Diode*. PhD thesis, Christian-Albrechts-Universität Kiel, 1994.
- [98] M. Armand. On the output spectrum of unlocked driven oscillators. *Proc. IEEE*, 57:798–799, 1969.
- [99] L. Pekárek and J. Krása. Ionization waves in plasmas.
- [100] M. B. Priestley. *Spectral Analysis and Time Series*. Academic, San Diego, 6 edition, 1989.
- [101] Bronstein Semendjajew. *Taschenbuch der Mathematik*. Verlag Harri Deutsch, Thun und Frankfurt/Main, 1991.
- [102] A. Khintchine. Korrelationstheorie der stationären Prozesse. *Math. Ann.*, 109:604–615, 1934.
- [103] R. J. Adrian. Conditional eddies in isotropic turbulence. *Phys. Fluids*, 22(11):2065–2070, 1979.
- [104] A. H. Nielsen, H. L. Pèseli, and J. Juul Rasmussen. Electrostatic fluctuations and turbulent plasma transport in low- β plasmas. *Physica Scripta*, 51:632–637, 1994.
- [105] B. K. Joseph, R. Jha, P. K. Kaw, S. K. Mattoo, C. V. S. Rao, Y. C. Saxena, and the ADITYA team. Observation of vortex-like coherent structures in the edge plasma of the aditya tokamak. *Phys. Plasmas*, 4(12):4292–4300, 1997.
- [106] T. Pierre, G. Leclert, and F. Braun. Magnetized double-plasma device for wave studies. *Rev. Sci. Instrum.*, 58:6–11, 1987.
- [107] K. N. Leung, G. R. Taylor, J. M. Barrick, S. L. Paul, and R. E. Kribel. Plasma confinement by permanent magnet boundaries. *Phys. Lett. A*, 57:145, 1976.
- [108] T. Klinger. private communications.

- [109] V. Rohde. *Anwendung der Resonanzkegelmethode in der Ionosphäre und in Laborplasmen*. PhD thesis, Christian-Albrechts-Universität Kiel, 1993.
- [110] H. M. Mott-Smith and I. Langmuir. The theory of collectors in gaseous discharges. *Phys. Rev.*, 28:727–763, 1926.
- [111] F. F. Chen. Electric probes. In H. Huddelstone, editor, *Plasma Diagnostic Techniques*. Academic, New York, 1965.
- [112] N. Hershkowitz. How langmuir probes work. In O. Auciello and D. L. Flamm, editors, *Plasma Diagnostics*, volume 1. Academic, New York, 1993.
- [113] K. Hansen, T. Klinger, and A. Piel. Computer controlled probe diagnostic system and application in a magnetized laboratory plasma. *Rev. Sci. Instrum.*, 65(8):2615 – 2622, 1994.
- [114] A. Latten. Entwicklung eines 64-Kanal-Transientenrekorders zur Untersuchung turbulenter Driftwellen. Master's thesis, Christian-Albrechts-Universität Kiel, 1994.
- [115] U. Boelter. Untersuchungen zur Wechselwirkung stromtriebener Driftwellen mit Potentialrelaxationsoszillationen. Master's thesis, Christian-Albrechts-Universität Kiel, Januar 1996.
- [116] J. Noetzel. Destabilisierung und Sättigung von Driftwellen im Experiment Kiwi. Master's thesis, Christian-Albrechts-Universität Kiel, Dezember 1996.
- [117] C. Schröder. Experimentelle Untersuchungen des globalen dynamischen Plasmagleichgewichts im Plasmaexperiment KIWI. Master's thesis, Christian-Albrechts-Universität Kiel, 1999.
- [118] S.-T. Tsai, F. W. Perkins, and T. H. Stix. Thermal conductivity and low frequency waves in collisional plasmas. *Phys. Fluids*, 13(8):2108–2114, 1970.

Curriculum vitae

personal data

name Dietmar Block
date of birth January 5, 1972
place of birth Hamburg
nationality German
marital status Married

school education

1978 till 1982 Primary school in Nahe
1982 till 1991 Grammar school in Norderstedt,
June 1991 Final examen (Abitur), mark 1.6
1991 till 1992 Civil service with the Arbeiter–Samariter–Bund in Tangstedt
 as first-aid attendant and first-aid instructor

scientific education

1992 till 1998 Study of physics at the Christian–Albrechts–University
 zu Kiel
1.10.95 till 31.12.97 Research assistant in the group of Prof. Piel in the space
 science project DEOS (Dynamic of the Equatorial iono-
 sphere Over Shar), DLR 50-OE-9503.
 Subject: Development of sensor electronics for an impe-
 dance probe.
1.12.96 till 31.12.97 Preparation of the master thesis in the group of Prof. Piel.
 Subject: Microcontroller controlled impedance probe
6.1.98 Diploma in physics (sehr gut)
1.1.98 till 30.4.98 Scientific member of the DEOS project.
 Subject: Preparation and supervision of the sounding
 rocket launch in SHAR (India).
since 1.5.98 Ph.D. graduation in the group of Prof. Piel.
 Subject: Synchronization of drift waves and its effects
 on fluctuation-induced transport
Sept. 2001 Research stay at the Physics Institute of the University
 of Tromso (Norway)
 Subject: Conditional averaging measurements of coher-
 ent structures in a simple magnetized torus for filament
 and RF-discharges.

Acknowledgments

Prof. Dr. A. Piel is gratefully acknowledged for the opportunity to prepare the present work in his group. He offered me generous freedom to find my own way to solve technical and scientific problems. His steady support and enthusiasm in scientific questions substantially contributed to the progress of this work.

The author most warmly thanks Prof. Dr. T. Klinger, Dr. V. Naulin, and Dipl. Phys. Ch. Schröder for many scientific debates and the fruitful collaboration. Prof. Dr. C. Rypdal and his co-workers are acknowledged for the kind hospitality during the stay in Tromsø.

Many of the presented experiments would not have been possible without the excellent technical support of V. Rohwer and B. Hipp. Special thanks belong to M. Brix and this team for the sophisticated and very reliable mechanical construction of the exciter and the 3D-positioning system.

For the help to find the right forms and solve other administrative problems, the author thanks M. Seeger and K. Hinz. Due to their refreshing way even these sometimes annoying tasks became a pleasure.

Special thanks belong to all members of the plasma physics group. The enjoyable debates at lunch time always gave new motivation for the second half of the day and sometimes even solutions to actual problems. Especially Dr. A. Melzer is gratefully acknowledged for the careful reading of the copy and Dr. F. Greiner for numerous support and discussions.

Last but not least, the author wishes to thank his family and especially his wife for encouragement and all the things beyond physics.

Hiermit versichere ich an Eides Statt, dass ich diese Arbeit ausschliesslich unter Anleitung meiner wissenschaftlichen Lehrer und unter Verwendung der angegebenen Hilfsmittel angefertigt habe.

Kiel,